UC Santa Barbara
UC Santa Barbara Electronic Theses and Dissertations

Title
The Thermoelectric Properties of Rare Earths as Dopants in InGaAs Films

Permalink
https://escholarship.org/uc/item/9np166mx

Author
Koltun, Rachel

Publication Date
2014

Peer reviewed|Thesis/dissertation

eScholarship.org Powered by the California Digital Library
University of California

UNIVERSITY OF CALIFORNIA

Santa Barbara

The Thermoelectric Properties of Rare Earths as Dopants in InGaAs Films

A dissertation submitted in partial satisfaction of the

requirements for the degree Doctor of Philosophy

in Materials

by

Rachel Ann Koltun

Committee in charge:

Professor Christopher J. Palmstrøm, Chair

Professor John E. Bowers

Professor Arthur C. Gossard

Professor James Allen

December 2014

The dissertation of Rachel Koltun is approved.

John E. Bowers

Arthur C. Gossard

S. James Allen

Christopher J. Palmstrøm, Committee Chair

September 2014

The Thermoelectric Properties of Rare Earths as Dopants in InGaAs Films

Copyright © 2014

By

Rachel Koltun

ACKNOWLEDGEMENTS

There are many people who have helped develop the work presented in this dissertation and supported me in my graduate career. First, I must thank my advisors Chris Palmstrøm and John Bowers, for their discussions and guidance throughout this process. I would also like to thank the rest of my committee, Art Gossard and Jim Allen for their input and new perspectives in examining my work.

I would like to thank my mentors from the beginning of graduate school, Jac Hall and Ashok Ramu, who introduced me to MBE growth and thermoelectric measurements. The thermoelectrics meetings have been a great sounding board for problems encountered in thermoelectrics research and I would like to thank everyone who participated in those meetings, including Ben, Matt, Yichi, Tyler, Anne and Christina. A special thanks to Hong Lu and Peter Burke,who have helped me understand the nuances of MBE growth and the embedded nanoparticle material system. Alex Sztein was instrumental in developing the thermoelectrics measurements and taught me how to use high temperature thermoelectrics setup. Not to mention the hours helping me fix the many problems I came across.

I must also thank Brian Schultz, for restoring order to the Palmstrøm MBE lab. Along with Brian, Sahil Patel, Bo Shojaei, Alex Young and Jason Kawasaki were all instrumental in maintaining the MBE equipment my first two years here and were great people to work with during my time here.

I would also like to thank the newer members of the Palmstrøm lab: Anthony, Nate, Javad, Tony, Mihir, Sean, Jay, Dan, and Tobias. Special thanks to Ryan Need for working on TEM and low temperature Hall and the many helpful discussions. John English deserves a special mention for always letting us use spare parts and pumps and never forgetting to give us a hard time.

This work made use of the world class facilities at UCSB. I would like to thank Tom Mates and Stephan Kraemer at CNSI who were instrumental in successfully characterizing ScAs and GdAs particles. Processing samples for high temperature measurements made use of the NNIN Nanofabrication facility, and the entire nanofab staff deserves a thank you for keeping the facilities running so well. Particularly, thanks to Brian Thibeault for help in process development. Collaborations with Joe Feser and David Cahill were instrumental in understanding thermal transport in this material system.

I also need to acknowledge funding for this work from the Center for Energy Efficient Materials, an Energy Frontier Research Center funded by the US Department of Energy, Office of Science, Basic Energy Sciences under award number DE-SC0001009.

Completing this Ph.D. would not have been possible without support from my family: my parents Eila and Doug, my brother, Ben, and my grandparents for their support over the years. Last, but certainly not least, I would like to thank my fiancé, Idse. Your love and support has been a crucial part of getting me to this point.

VITA OF RACHEL ANN KOLTUN

September 2014

EDUCATION

Bachelor of Arts in Physics, Northwestern University, June 2010

Doctor of Philosophy in Materials, University of California, Santa Barbara, September 2014
Advisors: Chris Palmstrøm and John Bowers

RESEARCH EXPERIENCE

September 2010-present
Graduate Research Assistant, Materials Department, UCSB: Explored different rare earth metals as new dopants in III-V semiconductors by molecular beam epitaxy and characterized thermoelectric properties of these materials at high temperature.

March 2008 – June 2010
Undergraduate Research Assistant, Venkat Chandrasekhar's Lab, Northwestern University: Used e-beam lithography to pattern substrates for thermopower measurements on graphene and carbon nanotube.

June 2007 – August 2007
Howard Hughes Medical Institute Bionanotechnology Intern, Michael Deem's Lab, Rice University: Wrote program in C++ to gather data and analyze strains of H5N1 avian flu virus.

PUBLICATIONS

1. **R. Koltun**, R.F. Need, A. Meginnis, J.P. Feser, D.G. Cahill, B.D. Schultz, C.J. Palmstrøm, and J.E. Bowers, "Epitaxial Growth of GdAs and Gd-doped InGaAs for High Temperature Thermoelectric Applications." *In Preparation*.

2. **R. Koltun**, J. L. Hall, T. E. Mates, J. E. Bowers, B. D. Schultz, and C. J. Palmstrøm, "Thermoelectric Properties of Single Crystal ScErAs:InGaAs Nanocomposites" J. Vac. Sci. Technol. B Microelectron. Nanom. Struct. 31, 1 (2013). [DOI: 10.1116/1.4810961]

CONFERENCE PRESENTATIONS AND POSTERS

1. **R. Koltun**, R.F. Need, A. Meginnis, B.D. Schultz, J.P. Feser, D.G. Cahill, J.E. Bowers, and C.J. Palmstrøm, "*High Temperature Thermoelectric Properties of InGaAs Films Using Traditional and Non-Traditional Dopants,*" MRS Spring Meeting 2014, San Francisco, California, April 2014.

2. **R. Koltun**, R. F. Need, A. Meginnis, B. D. Schultz, J. P. Feser, D. G. Cahill, J. E. Bowers, and C. J. Palmstrøm, "Thermoelectric Properties of Coherent Metallic Nanoparticles in III-As Thin Films," Physics of Sustainable Energy III, Berkely, CA, March 8, 2014.

3. **R. Koltun**, R.F. Need, A. Meginnis, B. D. Schultz, J. P. Feser, D. G. Cahill, J. E. Bowers, and C. J. Palmstrøm, "High Temperature Thermoelectric Properties of Gd Doped InGaAs Films," APS March Meeting 2014, Denver, Colorado, March 7, 2014.

4. **R. Koltun**, J. L. Hall, B. D. Schultz, A. T. Ramu, J. E. Bowers, and C. J. Palmstrøm, "Thermoelectric Properties of ErScAs:InGaAs," ICMR summer school on Inorganic Materials for Energy Conversion and Storage, Santa Barbara, CA, August 19, 2012.

5. **R. Koltun**, J. L. Hall, B. D. Schultz, A. T. Ramu, J. E. Bowers, and C. J. Palmstrøm, "Thermoelectric Enhancement of Rare Earth Arsenide Nanoparticles Coherently Embedded in Thin Film InGaAs," International Conference on Thermoelectrics, Aalborg, Denmark, July 11, 2012.

FIELDS OF STUDY

Major Field: Materials Science and Engineering

Emphasis: Electronic Materials

Studies in III-As semiconductors with rare earth composites grown by molecular beam epitaxy for high temperature thermoelectric applications

ABSTRACT

The Thermoelectric Properties of Rare Earths as Dopants in InGaAs Films

by

Rachel Ann Koltun

Current energy technologies lose over half of the energy input to waste heat. Thermoelectric materials can recover some of this waste heat by converting it into electricity. Thermoelectric devices have no moving parts, so they are low noise and highly reliable, making them particularly suitable for extreme environments. A good thermoelectric has low thermal conductivity to maintain large temperature gradients and high electrical conductivity to effectively transport carriers across that temperature gradient. One of the major challenges in engineering such thermoelectrics is effectively decoupling these parameters. These relationships are quantified in the dimensionless thermoelectric figure of merit, ZT, where a ZT of 1 is considered commercially viable.

Doping MBE grown InGaAs films with rare earths forms embedded nanoparticles that have been shown to improve thermoelectric efficiency of InGaAs. Rare earth doping effectively overcomes the problematic relationship between

electrical and thermal conductivities. These embedded particles effectively decouple thermal and electrical properties by contributing carriers to increase electrical conductivity as well as forming scattering centers for mid to long wavelength phonons to decrease thermal conductivity. However, the mechanism for carrier generation from rare earths is poorly understood. Comparing different rare earths as dopants in InGaAs, we find a positive correlation with the electrical activation efficiency as the rare earth arsenide nanoparticles are more closely lattice matched to the host matrix. This is in contrast to traditional Si doped InGaAs, which is fully ionized at room temperature. The high doping efficiency of Si leads it to be as good or better of a dopant for thermoelectrics compared to the best rare earths studied. We observe that rare earth doped InGaAs has thermal activation of carriers at high temperature, giving it the potential to be a more efficient thermoelectric in this regime than traditionally doped InGaAs.

A method was developed to determine the thermoelectric efficiency of a material system over a range of conductivities using only a few experimental data points. This allows for more efficient mapping of a material system for thermoelectrics. Using this analysis, high temperature measurements show that carrier scattering from rare earth impurities compensates the enhancement from thermally generated carriers, giving Si the potential to be a better thermoelectric dopant in InGaAs at high temperature. Extrapolating temperature dependent measurements to higher temperatures shows that a ZT greater than 3 should be theoretically possible for Gd or Si doped InGaAs at 700˚C.

TABLE OF CONTENTS

ACKNOWLEDGEMENTS iv

VITA OF RACHEL ANN KOLTUN vi

ABSTRACT viii

TABLE OF CONTENTS x

LIST OF FIGURES xiv

1 Introduction 1

1.1 Introduction to Thermoelectrics 1

1.1.1 Thermoelectric Efficiency 5

1.1.2 Limiting Factors to ZT 11

1.1.3 The Ideal Thermoelectric 12

1.1.4 Low Dimensional Structures 16

1.2 Recent Developments in Thermoelectrics 18

1.2.1 Sharp Features in Density of States 19

1.2.2 Resonant Doping 21

1.2.3 Nanoinclusions 22

1.2.4 Summary of Recent Developments 25

1.3 Background on Thermoelectric Properties of RE-As Particles in III-As Semiconductors 26

1.3.1 Embedded Nanoparticle System 26

1.3.2 History of Er doped InGaAs 33

1.4 Overview of Thesis 36

2 Characterization Methods 39

2.1 Introduction to Molecular Beam Epitaxy 39

2.2 Electrical Conductivity Measurements 42

2.2.1 Low Temperature Hall 42

2.2.2 High Temperature Hall 43

2.3 Seebeck Measurements 44

2.3.1 Error in High Temperature Measurements 44

2.4 Thermal Conductivity Measurements 47

2.4.1 3ω Method 48

2.4.2 Time Domain Thermoreflectance (TDTR) 50

2.5 Summary of Measurements 51

3 Si Doped InGaAs: an Experimental Base 52

3.1 InGaAs Growth 52

3.2 InGaAs Thermoelectric Properties 62

3.2.1 Doping with Si 62

3.2.2 Room Thermoelectric Properties of Si doped InGaAs 64

3.2.3 Low Temperature Transport 67

3.3 Conclusions from InGaAs Growth and Transport Properties 70

4 ScAs Particles in InGaAs 72

4.1 ScAs nanoparticles 72

4.1.1 Growth of Mechanism of Embedded ScAs Nanoparticles 73

4.1.2 Codeposition of ScAs Particles 75

4.1.3 Atom Probe of ScAs Nanoparticles 77

4.2 Room Temperature Electrical Properties of ScAs Particles in InGaAs 82

4.3 Room Temperature Properties of ErScAs particles in InGaAs 85

4.3.1 Doping Mechanism From Rare Earths 89

4.3.2 Thermal Conductivity of Er and Sc Doped InGaAs 92

4.4 Conclusions from Sc and ErSc Doping 96

5 GdAs Nanoparticles in InGaAs: a Survey of Rare Earths 98

5.1 Growth of GdAs Thin Films 99

5.2 TEM of GdAs Nanoparticles in InGaAs 102

5.3 Room Temperature Thermoelectric Properties of Embedded GdAs Particles in InGaAs 104

5.4 Comparison of Doping with Si to Different Rare Earths at Room Temperature 110

5.4.1 Doping Mechanism of Rare Earths in InGaAs 110

5.4.2 Transport in Rare Earth Doped InGaAs 113

5.4.3 Scattering from Rare Earths 116

5.4.4 Reducing Thermal Conductivity in RE Doped InGaAs 118

5.4.5 Thermoelectric Properties of RE Doped InGaAs 124

5.5 Conclusions and Future Work for Gd doped InGaAs 127

6 Codoping as a Tool to Improve Thermoelectric Efficiency 129

6.1 The Concept of Codoping 129

6.2 Electrical Transport of Be and Si Codoping with Sc in InGaAs 130

6.3 Price Analysis for ZT Optimization 137

6.4 Conclusions 143

7 Literature Summary of Rare Earths in InGaAs 144

7.1 Electrical Comparison of Rare Earths 145

7.2 Conclusions 152

8 Temperature Dependent Comparison of Rare Earth and Traditional Dopants 154

8.1 High Temperature Hall Effect 155

8.2 Low Temperature Hall 159

8.3 High Temperature Thermoelectric Properties 167

8.3.1 InP Substrate Conduction and Bipolar Conductivity........................ 169
8.3.2 Summary of High Temperature Properties...................................... 171
8.3.3 Optimizing ZT at High Temperature.. 176
8.4 Conclusions 184

9 Conclusions and Future Work 186

9.1 Conclusions 186
9.2 Future Work... 190
9.2.1 High Temperature Measurements.. 190
9.2.2 Growth Rate Effect... 191
9.2.3 Si as a Dopant in InGaAs 191

10 Appendix..193

A.1 Substrate Removal for High Temperature Measurements 193
B.1 Defect Levels From Temperature Dependent Hall.. 196
C.1 Particle Detection From Low Temperature Photoluminesence.............................. 198

References 200

LIST OF FIGURES

Figure 1.1 Estimated US Energy Use in 2013[1] 1

Figure 1.2 Schematic of a Thermoelectric Device 2

Figure 1.3 Schematic of the Seebeck Effect 4

Figure 1.4 Thermoelectric Efficiency versus ZT for a Thermoelectric Element in an Automobile Environment 9

Figure 1.5 ZT Comparison to Other Energy Technologies[3] 10

Figure 1.6 Thermoelectric Properties of Bi_2Te_3 12

Figure 1.7 ZT Improvement over Time[9] 15

Figure 1.8 Density of States With Reducing Dimensionality[6] 17

Figure 1.9 Quantum Confinement Opens Bandgap in Bi Wire[17] 18

Figure 1.10 Increasing Seebeck From Quantum Confinement of Gated InAs Nanowire 20

Figure 1.11 Tl as a Resonant Dopant in PbTe 22

Figure 1.12 Band Alignment and Mesoscopic Disorder Improve ZT of PbTe 24

Figure 1.13 Electron Filtering in InGaAs 27

Figure 1.14 Lattice Parameters of Rare Earth-Arsenides 28

Figure 1.15 Rare Earth Arsenide Nanoparticles in InGaAs 29

Figure 1.16 Interfacial Properties of ErAs 31

Figure 1.17 Quantum Confinement of RE-As Particles 32

Figure 1.18 Band Alignment of RE-As Particles in InGaAs 33

Figure 1.19 High ZT for Er Doped InGaAlAs 35

Figure 2.1 MBE Schematic 41

Figure 2.2 Hall Sample Schematic 43

Figure 2.3 High Temperature Seebeck Schematic 46

Figure 2.4 3ω schematic 49

Figure 3.1 RHEED of InGaAs Growth 55

Figure 3.2 Schematic of Oxide Desorption on InP by MBE 56

Figure 3.3 X-ray Characterization 59

Figure 3.4 Bandgap Heaven 60

Figure 3.5 Photoluminescence of Isolated InGaAs 61

Figure 3.6 Si as an Amphoteric Dopant in GaAs 63

Figure 3.7 Si Doping Calibration 64

Figure 3.8 Thermoelectric Properties of Si Doped InGaAs 66

Figure 3.9 Low Temperature Transport of Si Doped InGaAs 69

Figure 4.1 Embedded Nanoparticle Growth Mechanism 75

Figure 4.2 Sc Doped InGaAs RHEED 76

Figure 4.3 Atom Probe Schematic 79

Figure 4.4 Atom Probe of ScAs Nanoparticles 82

Figure 4.5 Electrical Properties of Sc Doped InGaAs 84

Figure 4.6 Thermoelectric Properties of $Er_xSc_{1-x}As$:InGaAs 88

Figure 4.7 Schematic of Doping Mechanism for Rare Earths in InGaAs 91

Figure 4.8 Thermal Conductivity of $Er_xSc_{1-x}As$:InGaAs 93

Figure 4.9 ZT of $Er_xSc_{1-x}As$:InGaAs 95

Figure 5.1 GdAs Temperature Series 101

Figure 5.2 GdAs Single Crystal 102

Figure 5.3 GdAs Nanoparticles in TEM 104

Figure 5.4 Electrical Properties of Gd doped InGaAs 107

Figure 5.5 Thermoelectric Properties of Gd doped InGaAs 109

Figure 5.6 Doping Efficiency of Different Rare Earths 111

Figure 5.7 Doping Efficiency of Rare Earths and Si in InGaAs 112

Figure 5.8 Lattice Mismatch Correlates with Doping Efficiency 113

Figure 5.9 InGaAs Electrical Transport 116

Figure 5.10 Mobility of Doped InGaAs 118

Figure 5.11 Error in TDTR Measurements[55] 123

Figure 5.12 Comparison of thermal conductivity measurements 124

Figure 5.13 Thermoelectric Properties of RE and Si doped InGaAs 126

Figure 6.1 Electrical Properties of Codoping with Sc 132

Figure 6.2 Intrinsic Material Relationship of Seebeck vs Conductivity 135

Figure 6.3 Power Factor of Codoped InGaAs 136

Figure 6.4 Price Analysis 138

Figure 6.5 Sc Doping Deviates From Single Parabolic Band Transport 140

Figure 6.6 Optimization of Sc doped InGaAs 142

Figure 7.1 Doping Efficiency in InGaAs 147

Figure 7.2 Comparison of Seebeck for Different Rare Earths 149

Figure 7.3 Comparison of Power Factor for Different Rare Earth Dopants 152

Figure 8.1 High Temperature Hall 158

Figure 8.2 Low Temperature Hall of Sc and Gd Doped InGaAs 162

Figure 8.3 Low Temperature Electrical Conductivity.. 165

Figure 8.4 Activation Energy of Gd and Sc doped InGaAs 166

Figure 8.5 Power Factor of Si and Gd doped InGaAs... 168

Figure 8.6 Effect of InP Substrate Conduction on Electrical Conductivty[107]....... 170

Figure 8.7 Temperature Dependent Power Factor 175

Figure 8.8 Seebeck Trends at Varying Temperature 178

Figure 8.9 Power Factor Optimization Over Temperature....................................... 179

Figure 8.10 Optimized ZT at 200˚C 181

Figure 8.11 ZT Trends Extrapolated to High Temperature...................................... 183

Figure 10.1 Au Bonding of InGaAs Films to Insulating Substrate 194

Figure 10.2 Many Levels from Gd doped InGaAs... 197

Figure 10.3 Photoluminesence to Detect ErAs Nanoparticles 199

Chapter 1

1 Introduction

1.1 Introduction to Thermoelectrics

Current energy technologies lose over half of the energy input to waste heat. In 2013 alone, the US rejected about 59 Quads (~59x10^{18} Joules) of energy out of the total 97 Quads used. In the transportation sector in particular, 79% of the energy input was estimated to be rejected, mostly as waste heat. Thermoelectric materials can recover some of this waste heat by converting it into usable electricity.

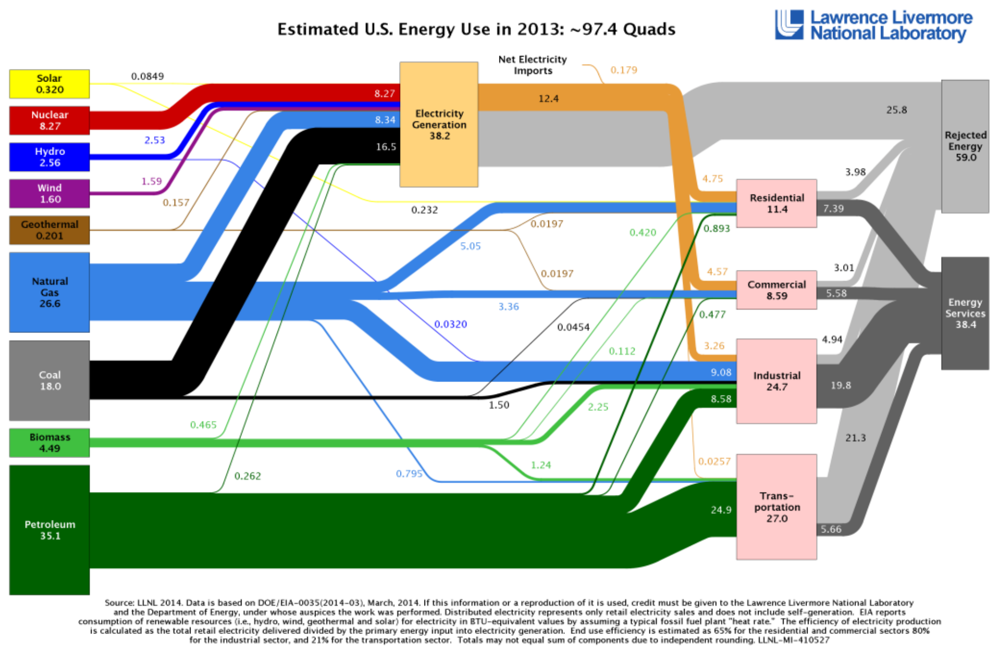

Figure 1.1 Estimated US Energy Use in 2013[1]
Over half of the energy input in the US is rejected, mostly as waste heat.

When a thermoelectric material is exposed to a temperature gradient, it causes charge carriers to thermally diffuse from the hot side to the cold side of the material. This causes a voltage to build up in open circuit conditions, or current to flow if the device is connected to a load as shown in Figure 1.2.

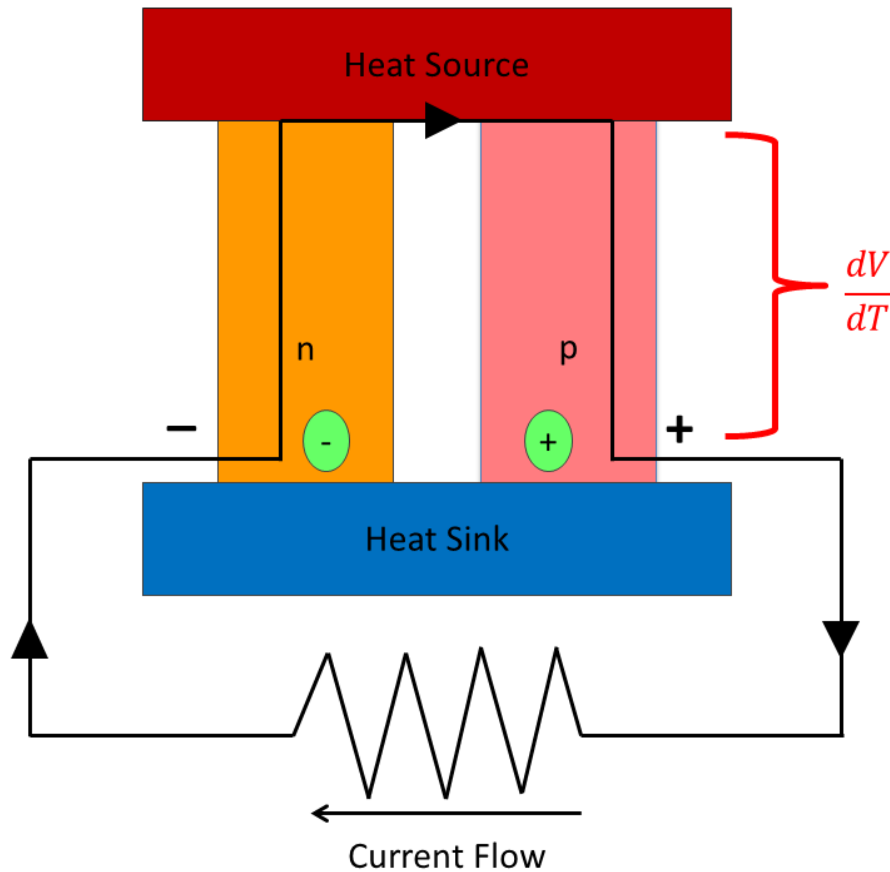

Figure 1.2 Schematic of a Thermoelectric Device
A thermoelectric device consists of an n and p leg connected electrically in series and thermally in parallel. An applied temperature gradient causes charge to thermally diffuse from the hot side to the cold side, driving a current when connected to a load. In a thermoelectric cooler, current is pushed in the direction of the arrows and the charge carriers carry heat away from the heat source, actively cooling the top of the device.

In order to make a thermoelectric power generator, a temperature gradient must be applied to both an n and/or a p-type material. Connecting the device thermally in parallel and electrically in series ensures that charge carriers flow in one continuous direction, allowing current to flow through a closed circuit.

A typical thermoelectric device has both an n and p-leg in order to maximize the voltage across the device. It is possible to use only one leg in a thermoelectric device as long as the electrical connection to the hot side of the thermoelectric does not act as thermal short. Thermoelectrics can also be used for solid state cooling. When a current is run through a thermoelectric device as shown in Figure 1.2, it drives charge carriers away from the heat source, carrying away heat with it. This actively cools the top of the device.

The defining factor of a thermoelectric is the ability to generate a thermal voltage across a material. In a 3D material, the density of states is filled by the Fermi-Dirac distribution function. At low temperature, this distribution function is very sharp as seen in Figure 1.3. Only the low energy carriers are filled. As the temperature increases, the distribution broadens so that higher energy carriers are also occupied. This leads to an energy differential of occupied carriers when there is a temperature gradient across a material, causing charge carriers to move from the hot side to the cold side.

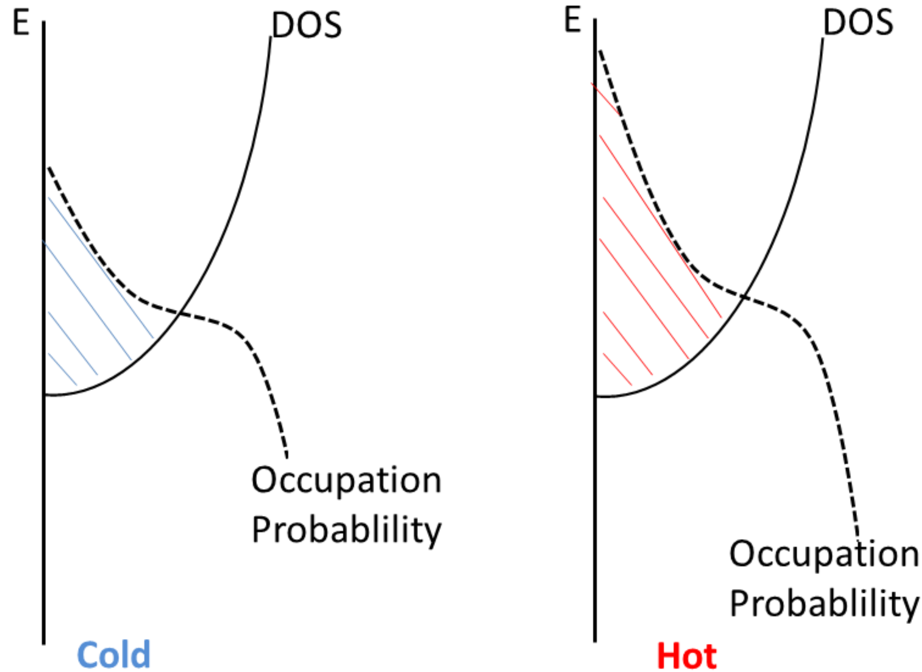

Figure 1.3 Schematic of the Seebeck Effect
At cold temperatures, the distribution function (shown by the dashed line) is more sharply defined and has a smaller tail while at hot temperatures the occupation function smears out and a much longer tail of higher energy carriers are occupied. This difference in occupation of high energy electrons drives carriers to move from the hot side to the cold side.

Thermoelectric devices have no moving parts, so they are low noise and highly reliable, making them particularly suitable for extreme environments. They are used in radioisotope thermoelectric generators (RTG) to power deep space probes for tens of years. Radioactive Plutonium is typically used as a heat source for thermoelectrics. Plutonium has a half-life of tens of years, making it an ideal heat source for long lasting thermoelectric devices. Voyager 1, which is an interstellar satellite launched in 1977, uses an RTG as its power source to take pictures and send data back to earth from the farthest points in space that can be reached. Today, more than 30 years later,

the RTG still provides enough power to operate the satellite as it explores deep space[2].

Terrestrially, thermoelectrics are used for car seat localized heating and cooling. Thermoelectrics are particularly advantageous at small scales due to the ability of these materials to scale down without compromising efficiency, contrary to typical mechanical heat engines[3].

1.1.1 Thermoelectric Efficiency

Thermoelectrics are characterized by the dimensionless thermoelectric figure of merit, ZT.

$$ZT = \frac{S^2\sigma}{\kappa}T \quad (1.1)$$

Where S is the Seebeck coefficient characterized by dV/dT, σ is the electrical conductivity, $\kappa = \kappa_{el} + \kappa_{lat}$ is the thermal conductivity and T is the temperature. The Seebeck coefficient is positive for p-type material and negative in n-type material. There are two contributions to thermal conductivity. κ_{lat} is caused by lattice vibrations, which transmit heat in the form of quasiparticles called phonons.

Mobile charge carriers in a material also carry heat[4]. According to Fourier's Law of heat conduction, heat currents are transported through a material by:

$$\boldsymbol{j}_Q = -\kappa\boldsymbol{\nabla}T \quad (1.2)$$

Where j_Q is the heat current through a temperature gradient and κ is the thermal conductivity. Since heat can also be carried by an electron gas, using the kinetic theory of gases, the electronic thermal conductivity (κ_{el}) can be expressed in terms of average thermal velocity (v), average scattering time (τ), mean free path length (l=vτ), and electronic heat capacity (c_{el}).

$$\kappa_{el} = \frac{1}{3} l v c_{el} \qquad (1.3)$$

Where v is a function of the Boltzmann constant (k_B), temperature and effective mass (m*) given by

$$v = \left(\frac{3k_B T}{m^*}\right)^{\frac{1}{2}} \qquad (1.4)$$

And c_{el} is given by the carrier concentration (n) and the Boltzmann constant.

$$c_{el} = \frac{3}{2} n k_B \qquad (1.5)$$

Putting (1.4) and (1.5) into equation (1.3), an expression for electronic contribution to thermal conductivity is given by

$$\kappa_{el} = \frac{3}{2} \frac{n\tau}{m^*} {k_B}^2 T \qquad (1.6)$$

Since electrical conductivity is given by

$$\sigma = \frac{ne^2\tau}{m^*} \qquad (1.7)$$

The electronic contribution to thermal conductivity is related to the electrical conductivity by the Wiedemann-Franz Law.

$$\kappa_{el} = \sigma LT \qquad (1.8)$$

Where σ is the electrical conductivity, T is the temperature and L is the Lorenz number, which is typically given by:

$$L = \frac{\pi^2}{3}\left(\frac{k_B}{e}\right)^2 \qquad (1.9)$$

A good thermoelectric has low thermal conductivity to maintain large temperature gradients and high electrical conductivity to effectively transport carriers across that temperature gradient. As can be seen from the Wiedemann-Franz law, the electrical conductivity and the electronic contribution to thermal conductivity are directly related to each other, so minimizing κ while maximizing σ is a major challenge in thermoelectrics. Since κ_{el} is usually fixed in order to maintain high electrical conductivity, the lattice contribution to thermal conductivity should be minimized. Introducing disorder to prevent lattice vibrations from propagating has been an effective tool to minimize κ_{lat}[5–8]. The ideal thermoelectric has a large power factor ($S^2\sigma$), which also implies that the Seebeck be large.

Current commercialized thermoelectric materials typically have a thermoelectric figure of merit, ZT, of about 1 at operating temperature[9]. ZT is related to overall maximum device efficiency, η, by the equation:

$$\begin{aligned}\eta = \frac{P}{j_q} &= \frac{(T_h - T_c)(\sqrt{1+ZT}-1)}{T_h(\sqrt{1+ZT}+\frac{T_c}{T_h})} \\ &= \frac{\Delta T}{T_h} * \frac{\sqrt{1+ZT}-1}{\sqrt{1+ZT}+\frac{T_c}{T_h}}\end{aligned} \tag{1.10}$$

Where P is power, j_q is the heat flux, T_h and T_c are the hot and cold side temperatures of the device in Kelvin. It can be seen that the efficiency of a thermoelectric device is a function of the carnot efficiency of a heat engine,$\Delta T/T_h$, so achieving high ZT does not directly correspond to high efficiency. Large ZTs can only approach the carnot efficiency limit.

An example of how ZT relates to device efficiency is shown in Figure 1.4 for a thermoelectric element on the tailpipe of a car. The automotive industry has shown considerable interest in thermoelectrics in recent years to increase the fuel efficiency of cars[10]. Studies have shown than an improvement in fuel economy by 1-5% can be realized by using a thermoelectric generator, generating on the order of hundreds of Watts [11, 12]. By putting a thermoelectric device on the tailpipe of a car close to the catalytic converter, a thermoelectric can be exposed to temperatures around 600˚C. The cooling network of the car can be easily extended to the thermoelectric device to maintain a maximum cold temperature around 100˚C. For this temperature range, it can be seen that a ZT of 1 is only 5% efficient. Using the best thermoelectric

materials to date with a ZT of about 2[5] would improve the efficiency to about 7% and a ZT of 10 cannot quite reach 15% efficiency, even without taking into account parasitic heat losses and contact resistance which brings the overall device efficiency down.

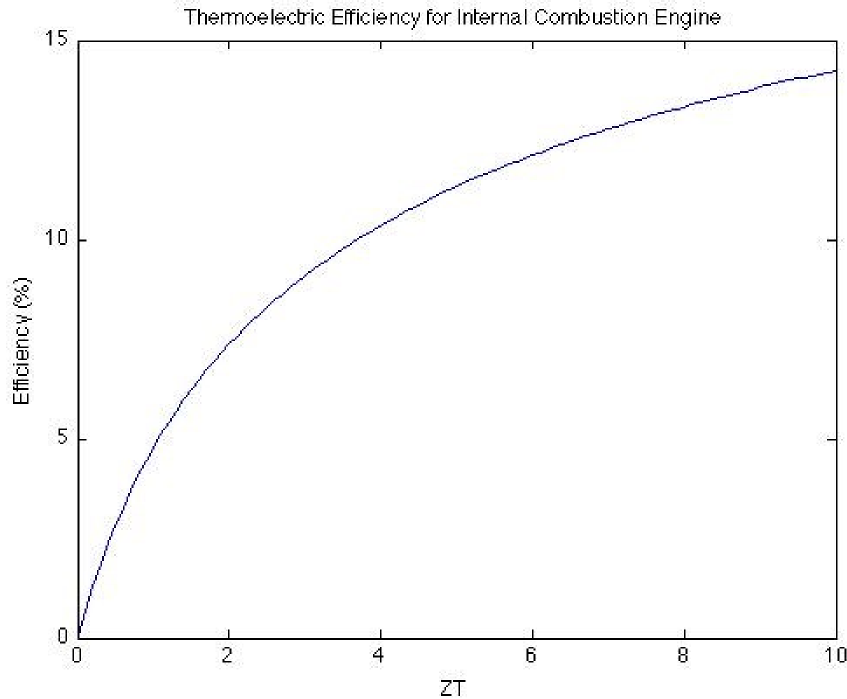

Figure 1.4 Thermoelectric Efficiency versus ZT for a Thermoelectric Element in an Automobile Environment
This calculation comes from equation (1.10)It assumes a hot temperature of 600˚C and a cold temperature of 100˚C. This does not take into account parasitic thermal and electrical losses in the thermoelectric device.

Figure 1.5 showcases thermoelectric efficiency in the context of existing energy technologies. It can be seen that the highest reported ZT values of 2 cannot reach the theoretical efficiency of any other energy technology. If a ZT of 4 were to be realized, thermoelectrics could compete with geothermal energy. However, a ZT of

20 would be needed to compete with existing energy technologies like coal, nuclear and solar. A ZT this large is not likely to be realized in the foreseeable future, so it can be concluded that the low efficiency of thermoelectrics will not be able to replace existing energy technologies. But by recovering even a small fraction of the very large amount of wasted heat from our energy use, a sizeable amount of energy can be recovered.

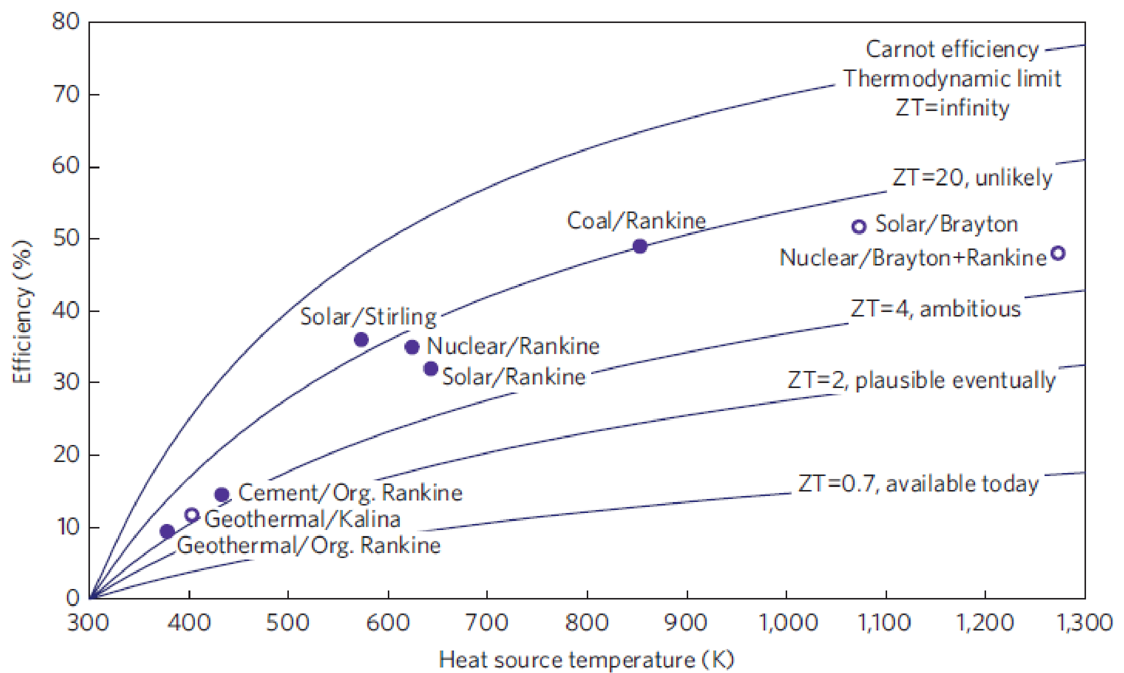

Figure 1.5 ZT Comparison to Other Energy Technologies[3]
The best thermoelectric materials to date have reached a ZT of 2, which has a maximum efficiency below any existing energy technology. With a ZT of 4, thermoelectrics could compete with geothermal energy. However, a ZT of 20, which is not likely to be achieved in the foreseeable future, is needed to compete with coal and solar energy technologies.

1.1.2 Limiting Factors to ZT

The biggest problem in thermoelectrics that limits ZT is that the different components of ZT, the Seebeck coefficient, electrical conductivity and thermal conductivity, tend to be inversely related, making it difficult to reach high values. For example, the thermoelectric properties of Bi_2Te_3, a common thermoelectric material, is modeled in Figure 1.6. It can be seen that as the carrier concentration increases, the electrical conductivity increases along with the thermal conductivity, due to the Wiedemann-Franz law. Furthermore, as the carrier concentration increases, the Seebeck decreases. Overall, a maximum power factor ($S^2\sigma$) is seen at 10^{20} cm^{-3} carriers and ZT is maximized at ~$3x10^{19}$ cm^{-3}. The next section will focus on why this inverse relationship is seen and what kind of materials should be used for thermoelectrics. Throughout this thesis, we will go deeper into how these relationships can be tuned by using the highly controllable growth method of molecular beam epitaxy.

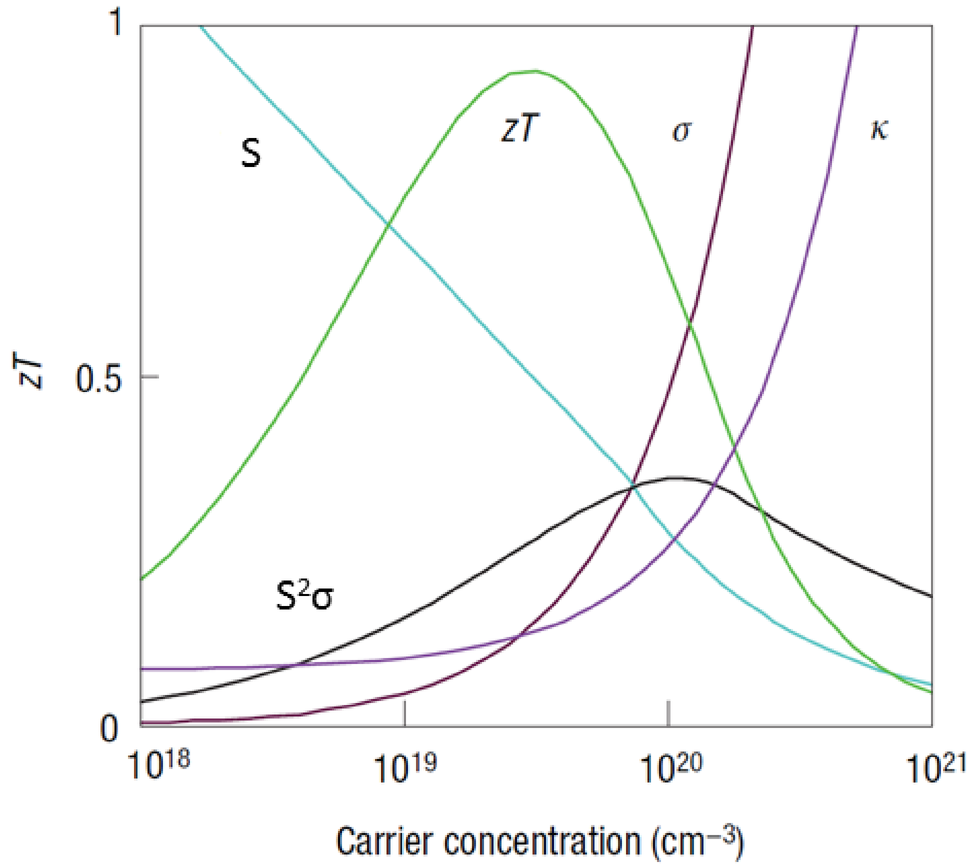

Figure 1.6 Thermoelectric Properties of Bi_2Te_3
Modelled thermoelectric properties of Bi_2Te_3[8].

1.1.3 The Ideal Thermoelectric

The ideal thermoelectric material is a phonon glass electron crystal (PGEC). This material maximizes electrical conductivity (electron crystal), while minimizing thermal conductivity (phonon glass). Adding impurities on multiple length scales and increasing interfacial area scatters phonons of different wavelengths, lowering thermal conductivity to make a phonon glass. To make an electron crystal, however, interfaces and impurities often scatter electrons in addition to phonons. One

approach to make a PGEC is alloying with isoelectronic elements, making complex unit cells that minimizes alloy scattering of charge carriers while creating large mass contrast to scatter phonons[8].

Although the thermoelectric effect was first discovered in metals, they are severely limited in their thermoelectric efficiency. Metals have partially filled bands, so there are many electrons and/or holes in conduction without the need for added thermal energy. Metals have too many carriers in conduction that are insensitive to temperature. Furthermore, the large electrical conductivity of metals leads to low Seebeck voltages due to Ohm's Law. To maximize the Seebeck voltage, it is important to reduce bipolar conduction. That is why semiconductors, with low minority carrier concentrations, are ideal. Furthermore, band engineering of semiconductors can be used to suppress minority carrier conduction for both thermal conductivity and Seebeck optimization[13, 14].

Since metals have many carriers thermally diffusing to the heat sink in a thermoelectric device, there will be significant heat transport from charge carriers associated with large carrier concentrations and electrical conductivities due to the Wiedemann-Franz law. High performing thermoelectrics effectively decouple the electrical and thermal conductivities. With κ_{el} dominating the thermal conductivity in metals, this is impossible to do, making metals poor thermoelectrics. Semiconductors have widely tunable electrical properties and typically much higher mobilities than metals due to their high crystal quality, low effective mass, and highly tunable carrier concentrations. The high mobility allows carriers to travel farther before scattering,

reducing the number of scattering events for an electron to transfer its energy to a phonon. The ability to achieve lower carrier concentrations also significantly decreases the electronic contribution to thermal conductivity, so that tuning the lattice thermal conductivity can effectively reduce the total thermal conductivity. This makes it possible to decouple the electrical and thermal conductivities to maximize ZT.

Semiconductors have bandgaps that take advantage of thermal excitations for enhanced electrical conduction at high temperatures. Large bandgap materials are ideal for high temperature thermoelectrics since charge carriers will receive sufficient thermal excitations at large k_bT to excite carriers into conduction from states in the bandgap, while still maintaining a low minority carrier concentration. Wide bandgap materials are, in general, more stable at high temperature. Using wide bandgap materials also reduces bipolar conduction. Narrow bandgap semiconductors are ideal for low to medium temperature applications since states in the bandgap do not require large thermal excitations (small k_bT) to conduct. Carrier concentrations in semiconductors can be orders of magnitude less than that in metals, which leads to higher Seebeck.

One of the most difficult challenges to overcome is the inverse relationship between Seebeck and electrical conductivity. Large electrical conductivity is good, but the high carrier concentration leads to a low Seebeck coefficient. Thermoelectrics have been around for a long time, but as can be seen in Figure 1.7, the maximum ZT stagnated for a number of years after the 1970s. In the early 1990s, Hicks and

Dresselhaus published a number of papers promising significant enhancement in ZT by moving to low dimensional structures due to quantum confinement effects[15–17]. Although their models were too simplistic, this spawned renewed interest in thermoelectrics, and the introduction of nanostructures into thermoelectrics realized great improvements in ZT over the next decade.

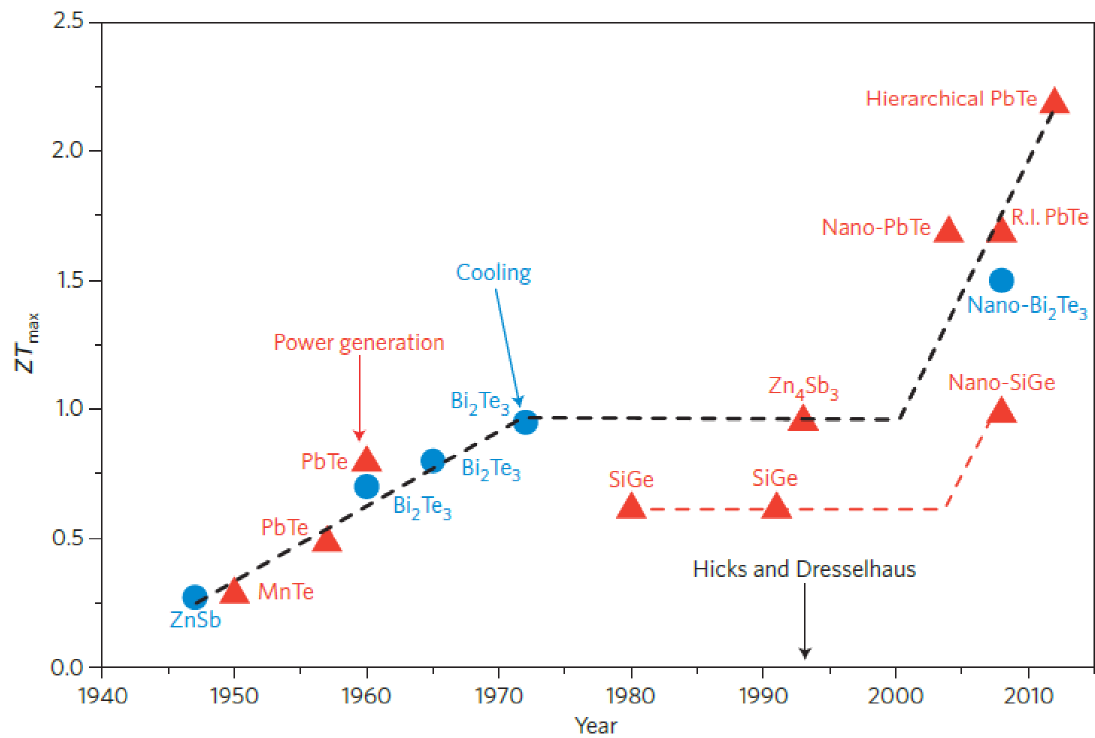

Figure 1.7 ZT Improvement over Time[9]
Thermoelectrics research improved ZT to about one in the 1970s, after which point research stagnated. Work by Hicks and Dresselhaus in the 1990s[15, 16] predicting thermoelectric enhancement from nanostructures spawned an increased interest in thermoelectrics research, leading to a ZT of 2.2 realized in 2012[5].

1.1.4 Low Dimensional Structures

To understand why this inverse relationship between Seebeck and electrical conductivity is seen, Cutler and Mott derived a relationship for bulk materials. Assuming charge carriers in a periodic potential traveling through band conduction, where the Fermi level is ~3k_bT below the conduction band edge or higher, the Seebeck coefficient can be defined as[18]:

$$S = -\frac{\pi^2 {k_B}^2 T}{3e} \frac{dln\ \sigma(\varepsilon)}{d\varepsilon}\Bigg]_{\varepsilon=\varepsilon_F} \qquad (1.11)$$

In order to increase the Seebeck coefficient, the electrical conductivity dependence on energy needs to be increased. Since the electrical conductivity is given by:

$$\sigma = qn(\varepsilon)\mu(\varepsilon) \qquad (1.12)$$

Equation (1.11) can be rewritten:[19]

$$S = -\frac{\pi^2 {k_B}^2 T}{3e}\left[\frac{1}{n}\frac{dn(\varepsilon)}{d\varepsilon} + \frac{1}{\mu}\frac{d\mu(\varepsilon)}{d\varepsilon}\right]_{\varepsilon=\varepsilon_F} \qquad (1.13)$$

Therefore, enhancing dn/dε, the density of states dependence on energy, around the fermi level will increase Seebeck, and in turn, ZT. Taking a look at the density of states in Figure 1.8 clearly shows how reducing dimensionality in materials increases the sharpness of the density of states. If the Fermi level can be tuned to one of those

sharp features, it should theoretically enhance thermoelectric performance, with the greatest improvements coming from 0D structures.

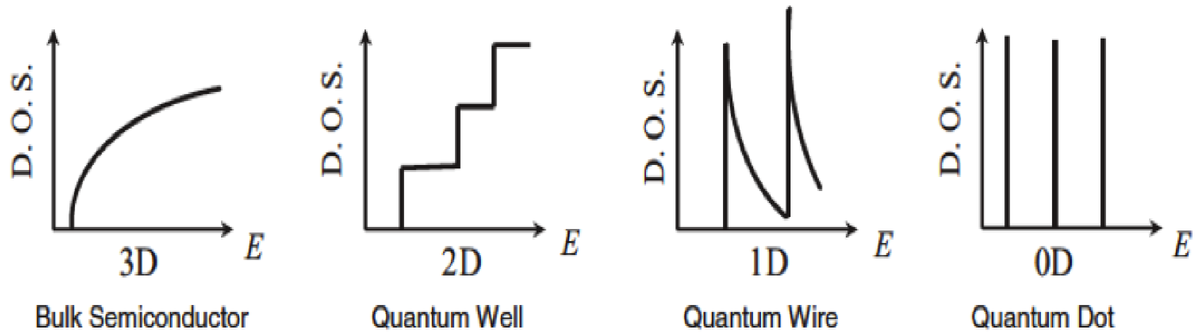

Figure 1.8 Density of States With Reducing Dimensionality[6]
The density of states has increasingly sharp features as the dimensionality is reduced from bulk. 2D wells sharp features at the steps from one energy level to another, 1D wires have sharper features at each energy level, but the sharpest features occur for the delta functions of a 0D material.

In addition to enhancement of the Seebeck coefficient, low dimensional structures increase boundary scattering of phonons at interfaces. Quantum confinement can also open up a bandgap in certain metals, as shown with Bi in Figure 1.9 and has been confirmed with absorption measurements[17, 20].

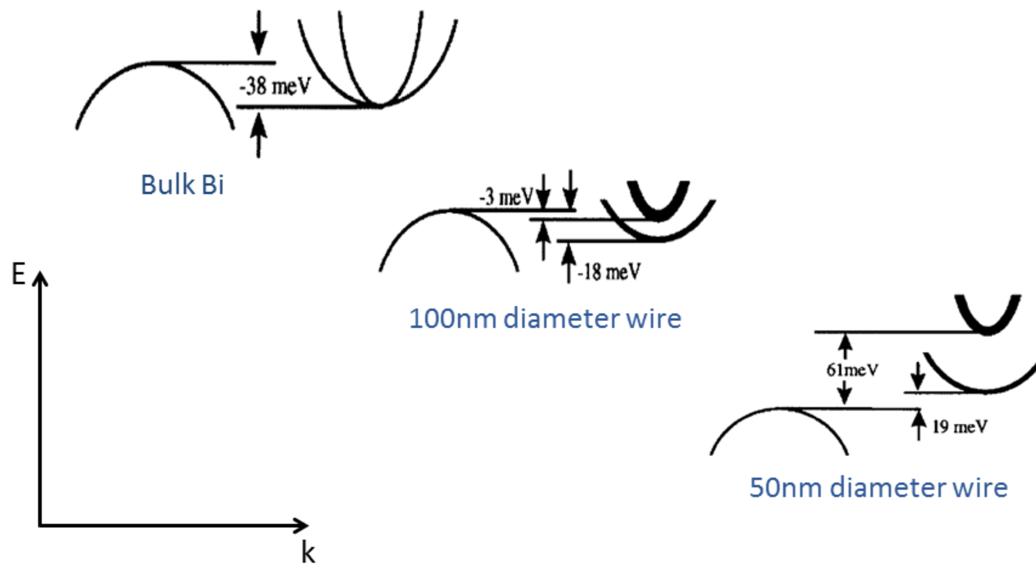

Figure 1.9 Quantum Confinement Opens Bandgap in Bi Wire[17]
As the diameter of a Bi wire is reduced, quantum confinement opens up a bandgap at about 50nm. Quantum confinement also splits the degeneracy seen in the conduction band of bulk Bi by raising the light band faster than the heavy band.

1.2 Recent Developments in Thermoelectrics

This section highlights recent developments in thermoelectrics to illustrate common beliefs to improve thermoelectric properties. Using various types nanostructures to improve both the electrical and thermal properties of materials for high ZT provides theoretical enhancement in a number of ways as explained in this section. Ultimately, it is seen that nanostructures effectively reduce the thermal conductivity of a material to improve ZT, but there is little experimental evidence for improvement in the power factor ($PF=S^2\sigma$) at reasonable operating temperatures.

1.2.1 Sharp Features in Density of States

The first experimental evidence of Seebeck enhancement from quantum confinement was demonstrated by gating an InAs nanowire to tune the Fermi level through the density of states. Figure 1.10 shows an increase in Seebeck corresponding to different sub bands from the 1D wire.

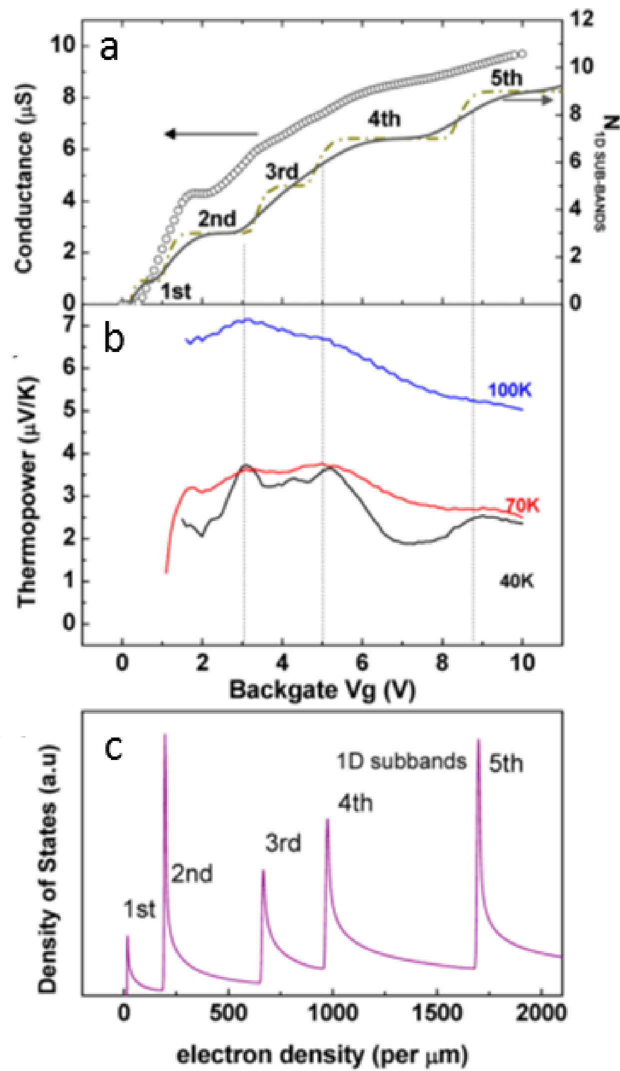

Figure 1.10 Increasing Seebeck From Quantum Confinement of Gated InAs Nanowire

Gate tuned a) conductance (DOS), b) Thermopower (Seebeck), and c) calculated density of states for a 23nm diameter InAs nanowire at low temperature[21].

It is important to note that these confinement effects are seen at low temperature, as thermal broadening of bands lessens the increase in Seebeck. As temperature is decreased, the overall magnitude of thermopower decreases. Furthermore, as

structures are decreased to the nanoscale, the number of states available for conduction decreases, causing the electrical conductivity to decrease well below that in bulk. Overall, it is not feasible to use these types of freestanding nanostructures for high ZT thermoelectrics. However, embedding nanostructures could be a more robust way to see enhancement.

1.2.2 Resonant Doping

Instead of using nanostructures, incorporating dopants that introduce sharp features in the density of states should be able to improve the relationship between Seebeck and conductivity as discussed in Section 1.1.4. Heremans et al. found that by doping PbTe with Tl, the Seebeck coefficient versus carrier concentration trends differed from what would be expected of single parabolic band transport as shown in Figure 1.11c[19]. This led to an increase in ZT at high temperature that was attributed to a resonant feature in the valence band density of states introduced by the Tl dopant.

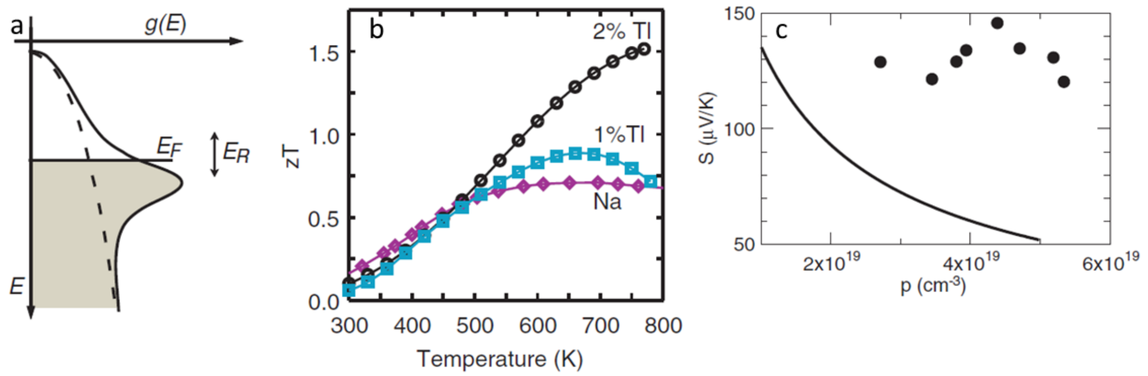

Figure 1.11 Tl as a Resonant Dopant in PbTe
a) schematic of the density of states of a resonant dopant, b) the high temperature ZT improves as more Tl is added, and c) Tl doped PbTe exceeds the traditional Seebeck versus carrier concentration relationships[19].

This is an interesting idea, providing a novel mechanism to improve ZT. However, experimental proof of this resonant feature has yet to be seen as the density of states was not measured. It is unclear exactly how Tl doping changes the PbTe. Since the experiment was carried out on bulk synthesized PbTe, there are many possibilities for unaccounted impurities or grain structuring that could contribute to the strange thermoelectric behavior.

1.2.3 Nanoinclusions

While zero-dimensional structures are predicted to see the greatest enhancement in Seebeck from quantum confinement, limited results on stacking faults in gated InAs nanowires show that this enhancement is at low temperatures and in structures that are not scalable to make thermoelectric devices[22].

Taking another approach, nanoinclusions can be selectively chosen to optimize the band alignment for thermoelectric enhancement at high temperature. Biswas et.

al. found good thermoelectric performance in p-type PbTe bulk material with coherently embedded SrTe nanoparticles[23]. Due to the crystal structures of PbTe and SrTe, the incorporation of SrTe particles that are stable at high temperature allows for a continuous Te sublattice when Sr is incorporated. This introduces interfacial phonon scattering without generating extended defects in the material that could compromise the electrical properties. Furthermore, the alignment of the valence bands in PbTe and SrTe[23] allows charge to propagate better through the nanoinclusions with temperature, while electrons are effectively blocked as shown in Figure 1.12b.

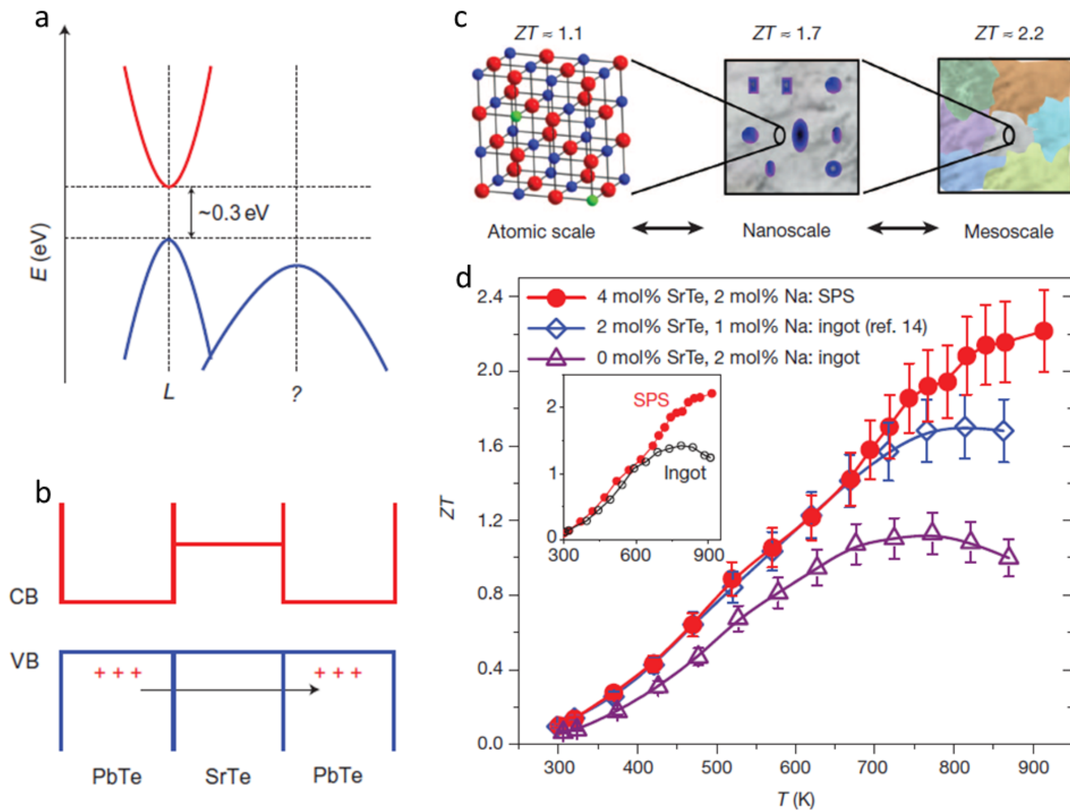

Figure 1.12 Band Alignment and Mesoscopic Disorder Improve ZT of PbTe

a) Valence band degeneracy contributes to conduction, b) band alignment of SrTe particles in PbTe allow holes to propagate and block electrons[23], c) disorder on many different length scales all contribute to d) high ZT of SrTe doped PbTe[5].

According to first principles electronic band structure calculations, the valence band maximum of PbTe lies lower than SrTe at low temperature. As temperature increases above room temperature, the heavy hole band of PbTe increases while that of SrTe decreases. Around 450K, the valence band edges line up, and holes can move more easily from one phase to another. Furthermore, multivalley conduction in

PbTe improves the conduction at high temperature. A maximum ZT of 1.7 was achieved at 815K[23].

This group was able to further improve ZT by incorporating disorder on many different length scales. Atomic dopants used to tune carrier concentration have the added effect of scattering short wavelength phonons. SrTe particles were used to scatter mid to long wavelength phonons, and the spark plasma sintering material synthesis process was used to create micron sized grains to scatter long wavelength phonons as shown in Figure 1.12c. Overall, this favorable band alignment combined with multi scale structuring to decrease thermal conductivity led to a maximum ZT of 2.2 at 900K[5].

1.2.4 Summary of Recent Developments

Recent research has clearly shown that nanostructuring materials can improve the thermoelectric properties. Nanostructuring can introduce sharp features into the density of states to optimize the Cutler-Mott relationship as described in equation (1.11)[18]. However, these enhancements have only been experimentally proven at low temperature. Bandgap engineering using nanostructures can effectively propagate majority carriers, while introducing impurities on a number of different lengthscales further reduces the thermal conductivity resulting in a ZT of 2.2 realized at high temperature. This high temperature result has not been shown to have improvements from quantum confinement effects. Although there is still some debate as to how thermal and electrical properties are altered from these nanostructures, it is clear that the thermoelectric properties are improved from bulk.

1.3 Background on Thermoelectric Properties of RE-As Particles in III-As Semiconductors

1.3.1 Embedded Nanoparticle System

This section lays the framework for exploring different rare earths embedded in InGaAs for high efficiency thermoelectrics. As explored in the previous section, nanoparticles incorporated into semiconductors have been used to increase phonon scattering and decrease the thermal conductivity, thus increasing ZT. Certain material systems have been theorized to provide electrical conduction enhancement while increasing the Seebeck coefficient by blocking low energy electrons (electron filtering) by tuning the conduction band alignment. Figure 1.13 shows how an InGaAs/InAlAs heterostructure can be used to block low energy electrons with an InGaAlAs barrier, while propagating high energy electrons. The Seebeck coefficient is effectively increased from bulk InGaAs in this way[24]. Incorporating this heterostructure simultaneously reduces the thermal conductivity.

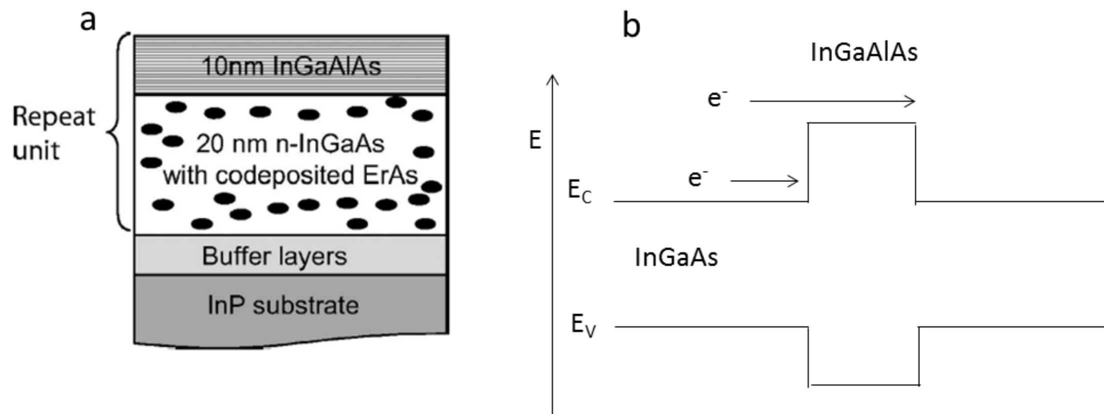

Figure 1.13 Electron Filtering in InGaAs
a) Using repeating units of Er doped InGaAs with InGaAlAs barriers[24] creates a band structure in (b), which scatters low energy electrons, but propagates high energy electrons to increase the Seebeck coefficient.

One such example of energy dependent electron scattering is epitaxial rare-earth arsenides (RE-As) embedded in III-As semiconductors[24–26].

RE-As are primarily cubic materials with the rock-salt crystal structure and have lattice parameters commensurate with many of the III-As based semiconductors as shown in Figure 1.14. The RE-As are thermodynamically stable with III-As up to high temperature and the rare-earth elements have low solubilities in the host semiconductors, leading to the precipitation of nanoparticles at relatively low concentrations[27, 28].

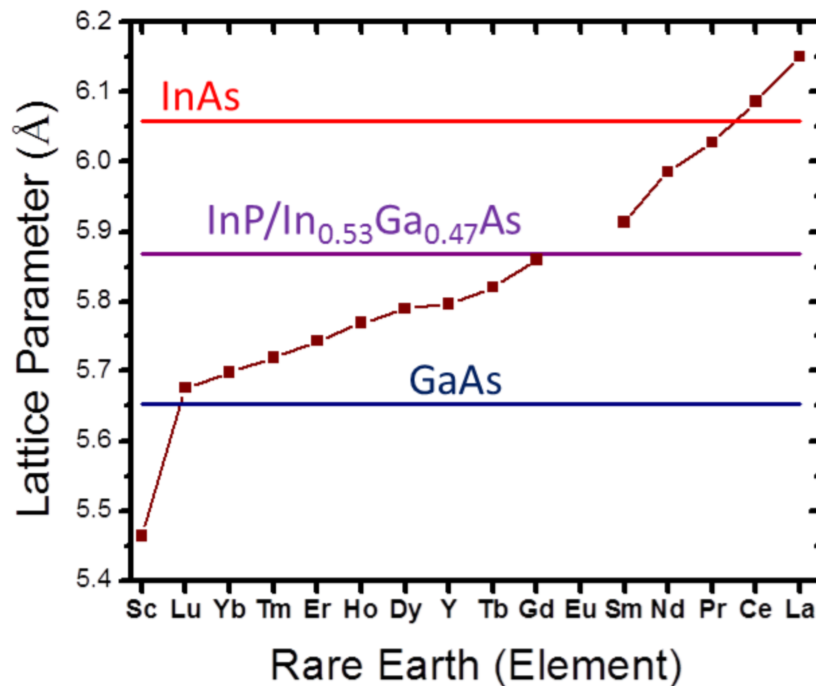

Figure 1.14 Lattice Parameters of Rare Earth-Arsenides
Rare Earth – Arsenides have lattice parameters commensurate with III-As semiconductors.

These nanoparticles are particularly interesting due to their crystal structure. The InGaAs matrix has the zinc blende crystal structure and the RE-As particles tend to form the rock salt crystal structure. These are two distinct crystal structures as shown in Figure 1.15a. The disruption to the periodicity of the InGaAs lattice by nanoparticles increases phonon scattering. Because these crystal structures have the same face centered cubic (FCC) As sublattice, the RE-As particles can be incorporated in InGaAs without creating extended defects by maintaining a continuous As sublattice.

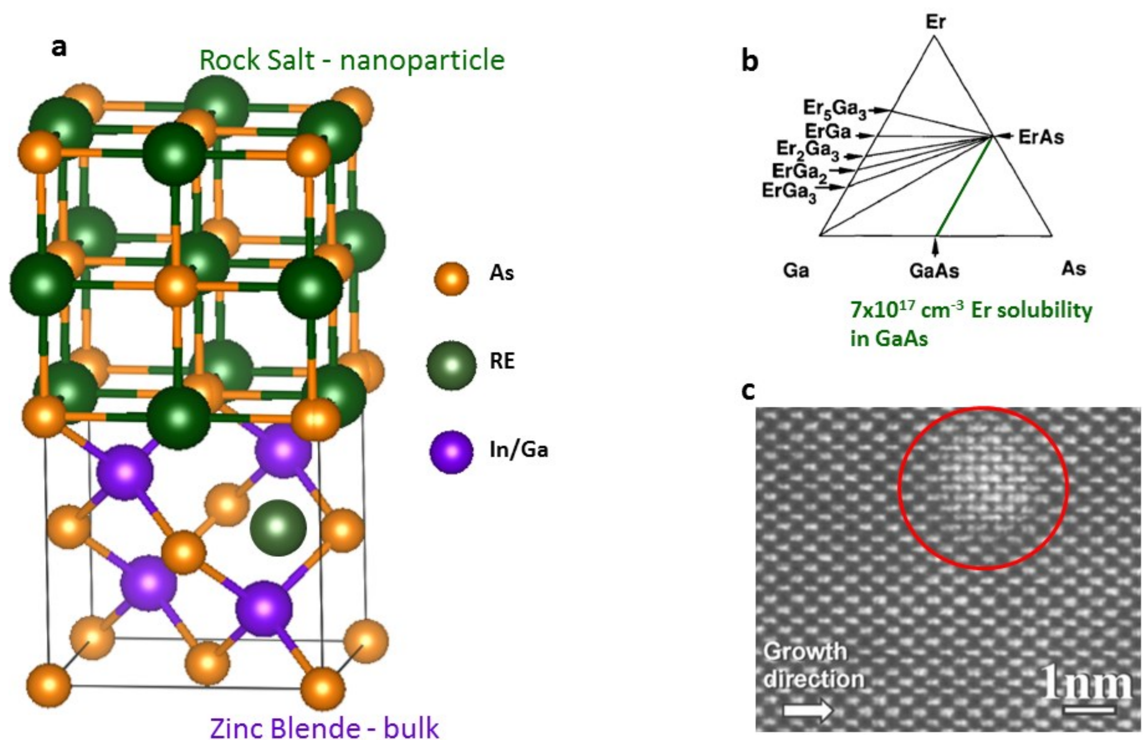

Figure 1.15 Rare Earth Arsenide Nanoparticles in InGaAs
a) The crystal structures of the InGaAs zinc blende matrix and the rare earth arsenide (RE-As) rock salt nanoparticle share the same FCC As sublattice. Rare earths also incorporate interstitially. b) the Ga-Er-As phase diagram showing the phase segregation of ErAs in GaAs[27] and c) a Scanning Transmission Electron Microscope image of an ErAs particle coherently embedded in an InGaAs matrix[29].

It is seen in Scanning Transmission Electron Microscopy (STEM), that the InGaAs lattice terminates in a group III element with an extended bond length in order to bridge the polar zinc blende (001) surface to the nonpolar rock salt (001) surface as shown in Figure 1.16[30]. This extended interfacial bond length leads to coherent, dislocation free interfaces that maintain high crystal quality for electron conduction. The Schottky barrier height of ErAs on n-type GaAs has been measured to be ~0.88eV[31]. Given the 0.45eV conduction band offset between GaAs and

InGaAs[32], it would be expected that the barrier height on InGaAs would be 0.43eV based on the band offset alone. Since the bandgap of InGaAs is 0.73, this would make ErAs an electron trap in InGaAs. However, it has been measured that ErAs has a barrier height of ~0.1eV on n-type InGaAs[33]. This discrepancy is likely due to surface pinning on GaAs, where this surface pinning is not seen on InGaAs[34].

It is seen in cross sectional scanning tunneling spectroscopy (XSTS) on GaAs substrates, that ErAs particles remain semimetallic despite theoretical predictions of quantum confinement opening up a bandgap[35]. An interfacial state from the ErAs particle is shown to propagate about 1.3 nm into the GaAs matrix, which, considering the lower conduction band edge of InGaAs could assist in carrier excitation from ErAs particles into the InGaAs matrix[36]. Overall, growth of these defect free nanocomposites allow for doping experiments that can effectively tune the electrical properties of InGaAs.

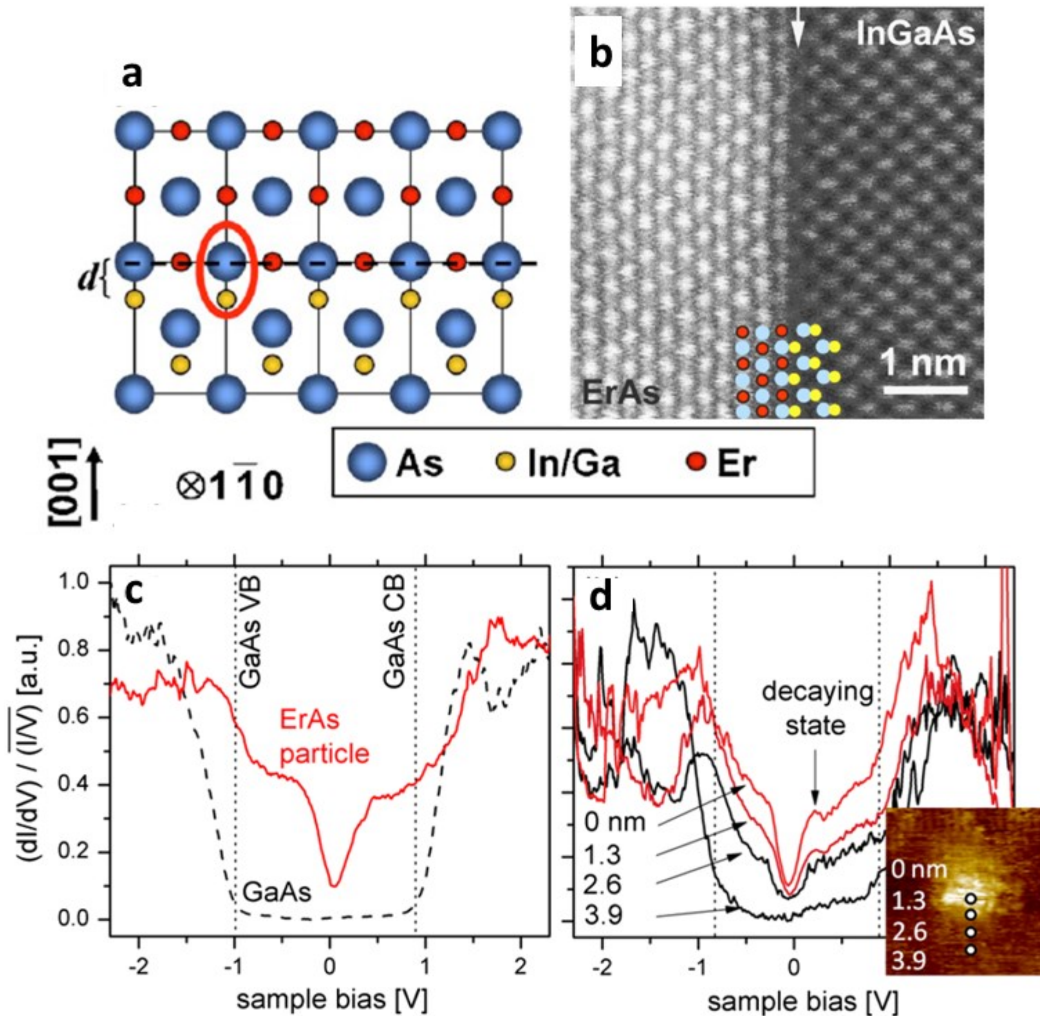

Figure 1.16 Interfacial Properties of ErAs

a) Schematic of the chain model and b) confirmation in STEM for the interfacial structure of ErAs in InGaAs[30]. c) Semimetallic local density of states for ErAs particle in GaAs matrix and d) the state at 0.2V on the ErAs particle edge that decays into the GaAs matrix[36].

Not only do these particles maintain electrical properties, due to the semimetallic properties and the expected position of the Fermi level of these nanoparticles close to the conduction band edge of InGaAs[33], these particles can behave as a new type of dopant, acting as a source of thermally excited carriers at high temperatures. Due to

the large carrier concentration of the semimetallic particles, carriers can be thermally excited from the conduction band of the RE-As nanoparticles into the InGaAs matrix. Quantum confinement effects from these small particles can raise the ground state energy level of the RE-As particles, reducing the thermal activation barrier as shown in Figure 1.17. The effective barrier height can be further reduced by defect assisted tunneling at the RE-As/InGaAs interface ash shown in Figure 1.18.

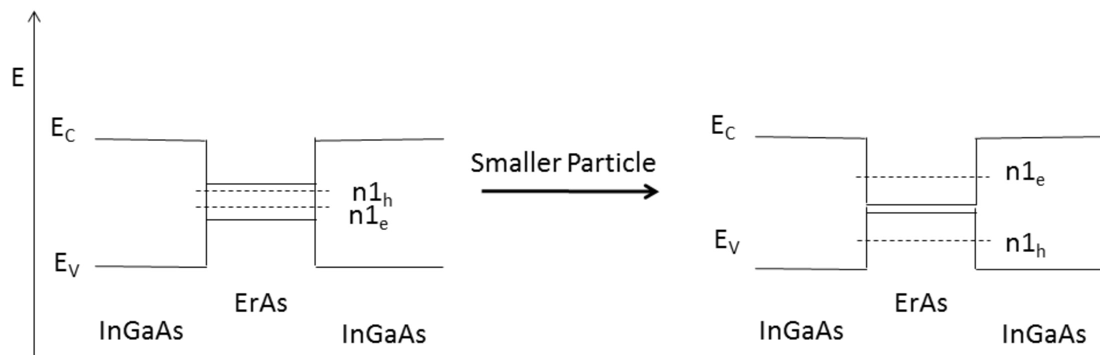

Figure 1.17 Quantum Confinement of RE-As Particles
The band structure of ErAs has an overlap of the valence band and conduction band edge. At smaller particle size, quantum confinement should increase the energy levels for electrons and decrease the energy levels of holes.

Furthermore, atomic impurities of rare earths occur in concentrations below the solubility limit. These atomic impurities sit on either interstitial or In/Ga substitutional sites, contributing donor levels to InGaAs below the conduction band edge. The levels from atomic impurities can also be a source of thermally ionized carriers. A schematic for the band alignment of rare earth doped InGaAs is shown in Figure 1.18.

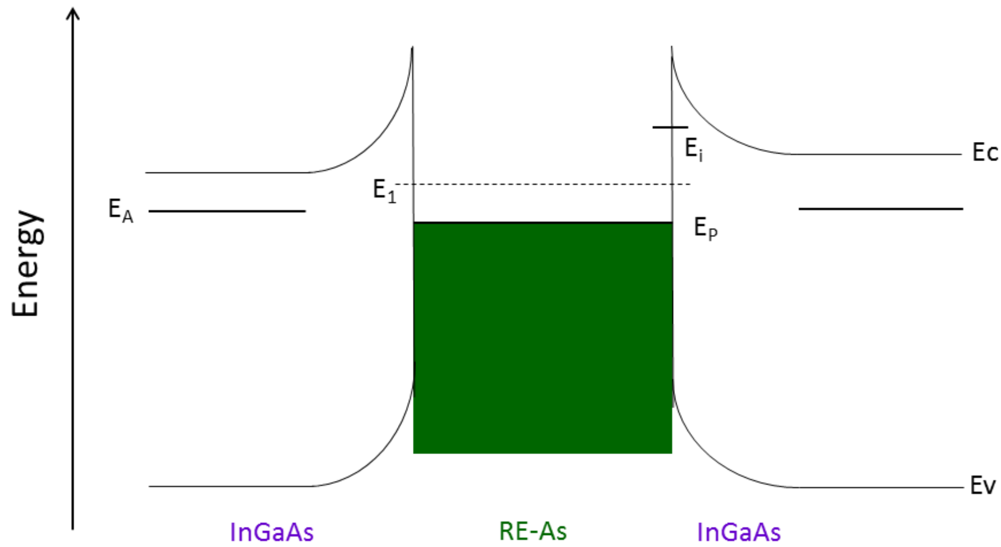

Figure 1.18 Band Alignment of RE-As Particles in InGaAs
Schematic for the double schottky barrier heterostructure from RE-As nanoparticles and atomic dopants. E_A represents levels due to atomic rare earth impurities, E_P is the Fermi level of the RE-As particle, E_1 is the ground state of the RE-As particle from quantum confinement and E_i is the interfacial state 0.2eV above the Fermi level observed for ErAs particles in GaAs[36].

Doping with rare earths can improve ZT by two mechanisms (particles and atomic impurities) to improve the electrical conductivity with temperature and one mechanism (particles) to decrease the thermal conductivity. This dissertation examines the effect of rare earths on electrical conductivity, Seebeck coefficient, and thermal conductivity.

1.3.2 History of Er doped InGaAs

The growth of ErAs nanoparticles in III-As semiconductors has been well characterized by an embedded growth mode[37]. First attempts to improve thermoelectric efficiency with ErAs used superlattice structures of ErAs islands or

embedded particles in InGaAlAs[38, 39]. Al was added to InGaAs in order to raise the conduction band edge of the matrix. Introducing these barriers was used to explore electron filtering as a tool to change the transport mechanism so that thermionic emission over a barrier will decouple the inverse relationship between electrical conductivity and the Seebeck coefficient[24]. Ultimately, it was seen that embedding nanoparticles in a homogenous film without using superlattice structures maximizes the mobility, and therefore the thermoelectric properties of the material. Incorporating ErAs particles in InGaAlAs was shown to provide thermoelectric enhancement over its Si doped counterpart with ZT values of 1.3 at 800K as shown in Figure 1.19[26]. This thermoelectric enhancement comes from the increasing electrical conductivity with temperature and the thermal conductivity reduction from Er incorporation.

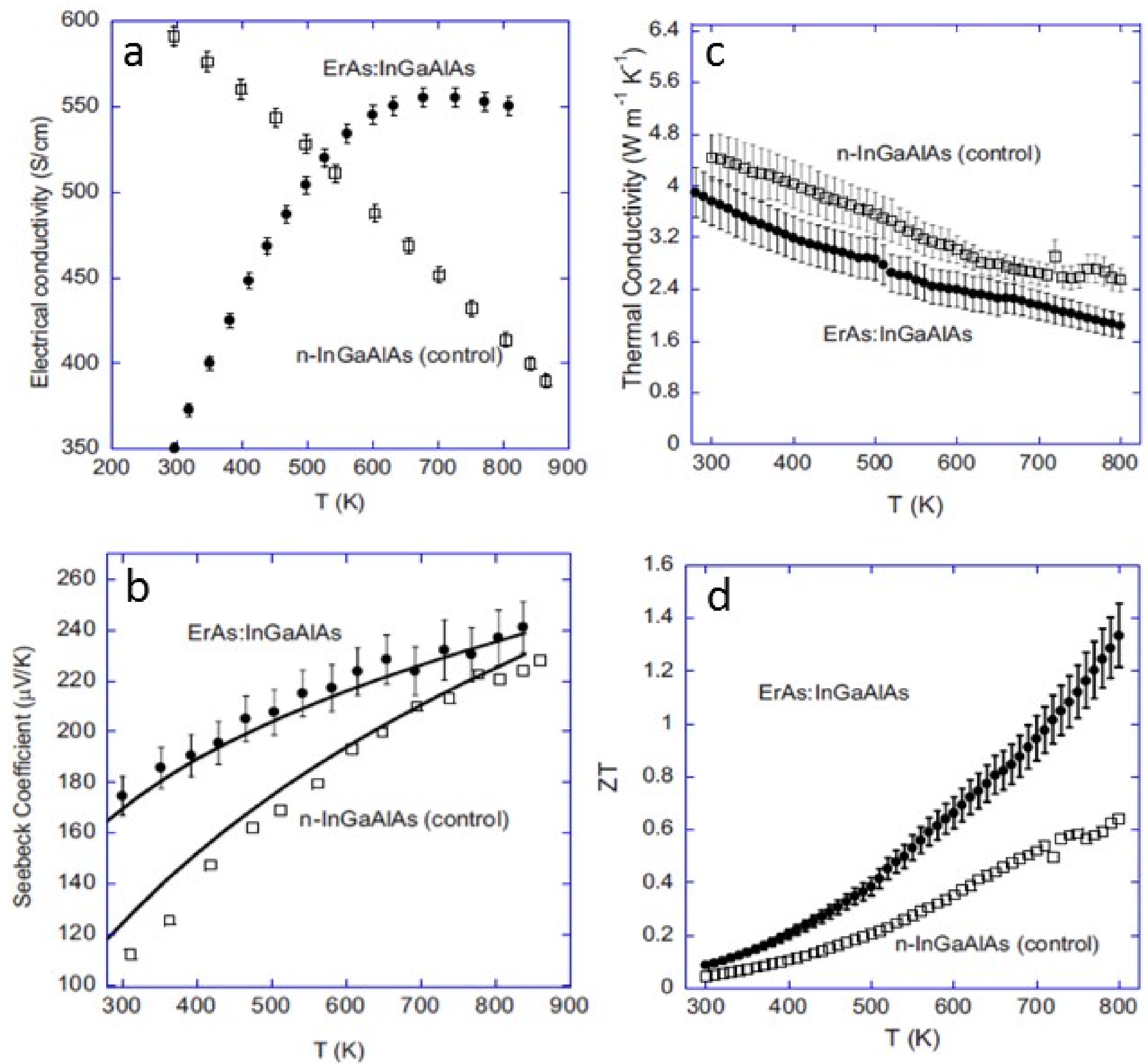

Figure 1.19 High ZT for Er Doped InGaAlAs
Temeprature dependent properties of a) electricalconductivity, b) Seebeck coefficient, c) thermal conductivity and d) ZT for Er doped InGaAlAs compared to Si doped InGaAlAs[26].

It was later seen that higher power factors could be realized in InGaAs without any Al content[40]. Subsequent improvements achieved a ZT of 1.7 at 850K for Er doped InGaAs[14]. However, the nature of how Er incorporation affects the electrical properties of InGaAs is poorly understood. Er has a solubility limit of

5×10^{17} atoms/cm^3 in GaAs[41] and begins to form coherently strained ErAs nanoparticles when codeposited with InGaAs above 8×10^{19} cm^{-3} by molecular beam epitaxy (MBE). It was also seen that Er acts as a shallow donor in InGaAs[42]. Er is a deep level in GaAs, while its doping efficiency increases as the conduction band edge of the surrounding matrix decreases by alloying with In[43]. It is not clear which contribution is from atomic Er impurities or from ErAs nanoparticles.

1.4 Overview of Thesis

This dissertation aims to better understand how rare earth arsenide particles affect the electrical properties of InGaAs by comparing different rare earth dopants in InGaAs. In order to understand why rare earths might be better suited as thermoelectric dopants, they must be compared to a traditional dopant in InGaAs, Si. Ultimately, it is seen that in this controlled study, Si has the potential to be a better thermoelectric dopant than any of the rare earths explored for this set of growths and measurements. There has been a big effort recently to survey a number of different rare earths in InGaAs, including Er, Tb[44–46], Ce, Sm, Eu, and Yb[14]. This work aims to systematically compare Sc, Gd and Er as dopants in InGaAs to understand how rare earths affect the thermoelectric properties. Rare earth doped InGaAs is also compared to Si doped InGaAs as a controlled material system where the doping mechanism is well understood.

This thesis lays the groundwork for the thermoelectric properties of InGaAs with traditional dopants and then compares different rare earths as dopants for thermoelectric applications. Ultimately, it is seen that Si, as a non-rare earth dopant

with a higher doping efficiency than any of the rare earths, can theoretically achieve as good or higher thermoelectric efficiency than any rare earth studied. The highest thermoelectric efficiencies of rare earth doped material are seen at rare earth concentrations below the point where a decrease in thermal conductivity is seen. Experimentally, Si doped InGaAs has been shown to result in power factors commensurate with the highest efficiency rare earth materials.

We begin detailing the experimental methods used to collect data. Chapter 3 introduces the InGaAs material system and low temperature transport properties by adding carriers from Si. The chapter will serve as a baseline for comparing to rare earth dopants.

Chapters 4 and 5 introduce new rare earths, Sc and Gd, respectively. It is verified that Sc and Gd form RE-As nanoparticles in InGaAs, similar to Er. The thermoelectric properties of Sc, Er, Gd and Si doping are compared to understand how rare earth doping behaves over a wide range of incorporation. A model is presented to explain the doping efficiency of different rare earth combinations.

Chapters 6 and 7 explores codoping with Sc and Si/Be as a tool to map out the thermoelectric landscape of InGaAs with these exotic dopants. This model is used to compare the theoretical thermoelectric properties of InGaAs to rare earth doped InGaAs in this work and previous studies in literature.

The high temperature thermoelectric properties of Si and rare earth doped InGaAs is examined in Chapter 8 and extrapolated to higher temperatures to predict the maximum ZT achievable at high temperatures for both Gd and Si doped InGaAs.

It is seen that Si is a more efficient thermoelectric dopant at high temperatures for this set of growths and measurements, with a thermoelectric power factor equal to that of the best performing Er doped InGaAs from literature[14]. Lastly, a summary of the work and suggestions for further studies are presented.

Chapter 2

2 Characterization Methods

This chapter details the experimental methods used to grow thin films and measure the thermoelectric properties of InGaAs at room and high temperature.

2.1 Introduction to Molecular Beam Epitaxy

Molecular beam epitaxy (MBE) is used to grow the InGaAs nanocomposites studied in this dissertation. This growth method allows atomic layer control over the sample structure and inherently has low impurity concentrations due to the ultra-high vacuum environment, allowing precise tuning of material properties that can be correlated to changes in the thermoelectric properties of a material.

$In_{0.53}Ga_{0.47}As$ (InGaAs) is lattice matched to InP, which is a commercially available substrate. Lattice matching InGaAs to the InP substrate allows epitaxial growth of high quality InGaAs films with low dislocation density. Furthermore, low concentrations of rare earth-arsenide nanoparticles can be coherently embedded in this material system during MBE growth.

MBE growth occurs in an ultra-high vacuum chamber as shown in Figure 2.1. Cells containing high purity source material are heated up to increase the vapor pressure of the material. When the shutters of the cells are opened, a molecular beam effuses out of the cell and into the ultra-high vacuum chamber. The flux of the

molecular beam can be tuned by changing the cell temperature for precise control over growth rate and structure. Due to the vacuum environment, the atoms do not interact until they reach the sample, at which point the atoms incorporate epitaxially.

The substrate is heated to a temperature where the impinging atoms have a high enough surface mobility to form a smooth surface, but there is not enough thermal energy to re-emit the incorporated group III or rare earth atoms into vacuum. As has a sticking coefficient less than one at high temperatures ideal for growth, so InGaAs must be grown under an As overpressure to ensure proper As incorporation.

For smooth surfaces, growth occurs at high enough temperature for step flow growth, so that impinging atoms have enough surface mobility to incorporate on a step edge. However, when incorporating nanostructures such as ErAs particles, lower growth temperatures are desired to achieve optimal nanoparticle size and density[47]. The temperature of the sample can be monitored by a pyrometer, measuring the blackbody emission. The surface ordering of the sample is monitored with Reflection High Energy Electron Diffraction (RHEED), which is a very useful tool in monitoring growth rate and surface quality *in situ*.

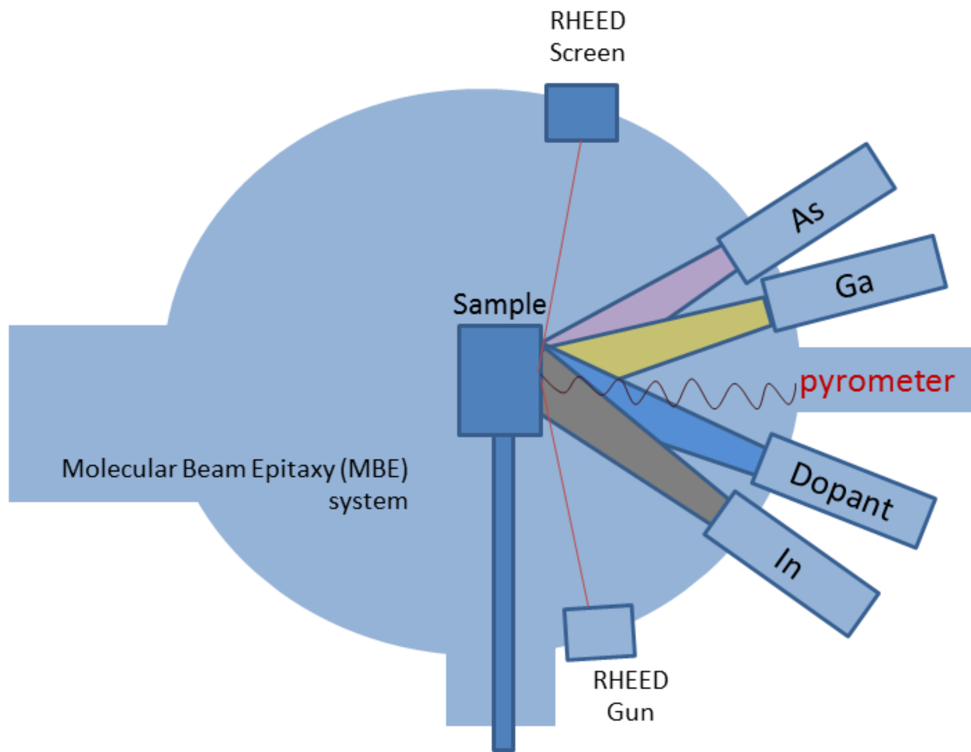

Figure 2.1 MBE Schematic
Schematic of MBE growth. The solid source cells are heated so that a molecular beam effuses into the ultra-high vacuum chamber and physisorbs onto the substrate. Growth can be monitored with a pyrometer and RHEED.

In this work, InGaAs was grown heteroepitaxially on InP. An As overpressure compensates for As desorption at high temperatures, allowing higher growth temperatures to be realized to improve the surface mobility of group III elements. To deposit InGaAs, In and Ga cells were opened under an As overpressure. Incorporation of traditional (Si/Be) or rare earth dopants was accomplished by codepositing with the dopant source. More details of the growth process will be discussed in Chapter 3.

2.2 Electrical Conductivity Measurements

Hall measurements and non magnetic four point probe were used to determine electrical conductivity of InGaAs films with good agreement between measurement setups. One of the most important techniques to understand transport in this material system is Hall effect measurements. In homogenous, isotropic films, Hall measurements using the Van der Pauw geometry are a useful way to extract the net carrier concentration and mobility.

2.2.1 Low Temperature Hall

Low temperature Hall and resistivity measurements were done on square samples with In dots placed at the four corners using a soldering iron consistent with the Van Der Pauw geometry. Samples were annealed and mounted onto a DIP package, where Au wires were soldered to connect the In dots to electrical pins. The DIP package was mounted onto a cold head and sealed under vacuum in order to reach a base temperature of ~10K. The sample was placed in a magnet that reaches up to 6kG magnetic field. The Hall coefficient and resistivity was measured at multiple temperatures in order to profile activation energies and scattering mechanisms.

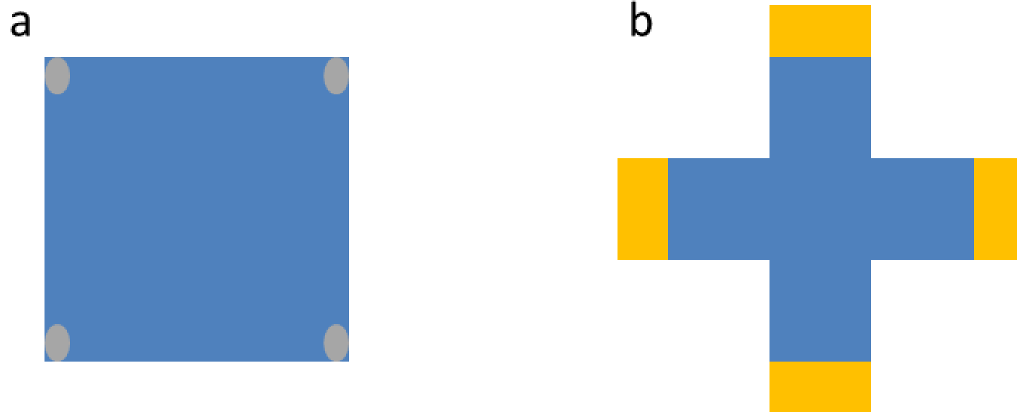

Figure 2.2 Hall Sample Schematic
a) Low temperature and room temperature Hall samples with In dots on the corners and b) Greek cross structures with lithographically defined mesas and TiWN/Au contacts for high temperature Hall/conductivity measurements.

2.2.2 High Temperature Hall

Hall measurements from 300K-800K were performed on InGaAs mesas passivated with SiN_x/SiO_2 200nm/100nm and contacts of TiWN/Au. TiWN was used as a sticking layer as well as a diffusion barrier for Au into InGaAs at high temperatures. Ohmic contact was made without the need for annealing before measurement. The sample is mounted onto a measurement stick held in place by tungsten probes that double as electrical contacts. Van der Pauw measurements were conducted up to 800K in an Ar environment to extract carrier concentration and mobility information. Further details about the high temperature Hall setup can be found in Peter Burke's thesis[14].

2.3 Seebeck Measurements

The Seebeck coefficient was measured in plane using the differential method[48]. At room temperature, a temperature gradient was applied using two Peltier elements simultaneously heating and cooling opposite ends of the sample. The voltage difference was measured at each end of the sample by electrical contacts made with In dots and the temperature difference was measured by subtracting the temperature of two thermocouples making contact with a silicone based thermal paste next to the voltage contacts. Under open circuit conditions, a thermal voltage can be measured. Plotting this thermal voltage over a range of temperature gradients results in a straight line with the slope equal to the Seebeck coefficient. A more detailed description of the measurement setup used can be found in Alex Sztein's thesis[49].

The same measurement technique was used at high temperature, except that the sample was passivated with SiN_x/SiO_2 and electrical contacts were made with TiWN/Au. A temperature gradient was applied with two differentially heated copper blocks and the thermocouples made thermal contact with hand placed dots of silver paste. This measurement occurred in vacuum to prevent the copper blocks from oxidizing.

2.3.1 Error in High Temperature Measurements

It is important to note the error in these high temperature measurements. The error of these measurement techniques can be judged based on the stability of the

measurement over multiple runs, over multiple measurement setups, and over different pieces of the sample.

Four point electrical conductivity and Hall measurements show excellent agreement between measurement setups. Different pieces of the same sample on a two inch wafers leads to 5-10% difference in the measurement result. In general, the electrical conductivity measurements are very repeatable.

Seebeck measurements, however, are less repeatable and are the largest source of error in high temperature power factor measurements. Typically there is ~10-20% error between Seebeck measurements on the room temperature Peltier setup and the high temperature bell jar. Since Seebeck is a squared term in power factor calculations, the error is compounded when analyzing power factor. The error in Seebeck measurements is mostly due to human error in placing thermocouple probes.

During Seebeck measurements, the voltage difference and temperature difference are simultaneously measured. Voltage measurements essentially measure the voltage at the edge of the voltage pads, where temperature measurements measure the average temperature across the entire area of the thermal paste. In the high temperature setup in particular, the dot of thermal paste is rather large since it must be placed by hand, so the average temperature is taken over a much larger area than the average voltage. This can lead to significant error in the measurement.

The schematic in Figure 2.3 illustrates how the Seebeck measurement is conducted. If the dot of thermal paste extends too far back from the edge of the voltage contact, the temperature difference measured will be systematically too large,

leading to a lower measured Seebeck. Conversely, if the dot of thermal paste extends too far in front of the edge of the voltage pad, the temperature difference measured will be systematically too low and the measured Seebeck will be high.

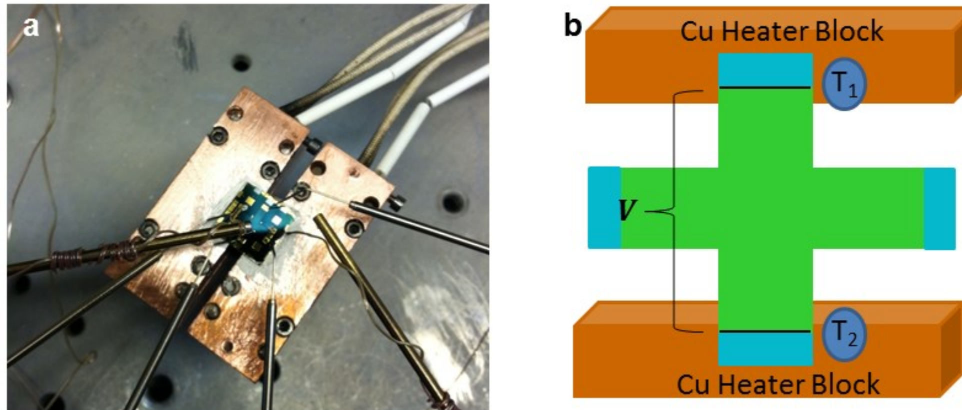

Figure 2.3 High Temperature Seebeck Schematic
a) Picture of a Seebeck and conductivity measurement in the high temperature bell jar and b) schematic of the Seebeck measurement in the high temperature bell jar.

The quickest way to improve the accuracy of the measurement is to use longer Seebeck bars so that there is a larger thermal area sink to the copper heater. This leads to smaller temperature gradients over the area of measurement, so that the thermal paste dot measures a more uniform temperature.

In order to make more precise Seebeck measurements that also eliminates the issue of independently controlling the temperature of two different copper heaters, lithographically patterned heaters and thermometers will achieve more precise temperature gradients and measurements. An AC technique to accurately measure small voltages and changes in temperature across a sample is described in these references[50, 51].

Since the temperature trends of Seebeck should be correct even with systematic error in the magnitude of the measured Seebeck, the high temperature Seebeck data is normalized to fit the more accurate measurements on the room temperature setup. A further error of +/- 10μV/K is expected due to the Seebeck effect from the voltage probes.

2.4 Thermal Conductivity Measurements

Thermal conductivity measurements are one of the most difficult and error prone measurements in the field of thermoelectrics, particularly in thin films. Although most of the improvements in ZT reported in literature come from reduced thermal conductivity, the poor accuracy of these measurement techniques should lead readers to be critical of findings reporting enhancement purely from a measured reduction in thermal conductivity. Thermal models can be paired with thermal conductivity measurements to illuminate different phonon scattering mechanisms in different material systems.

To begin, the units for thermal conductivity are W/m-K. In order to measure the thermal conductivity, one must apply a known power to a material and measure the temperature difference over a finite distance. Thermal conductivity measurements on thin films are inherently error prone due to the difficulty in accurately measuring temperature over short distances. There are two major experimental methods to determine thermal conductivities of thin films; the 3ω method[52, 53] and Time Domain Thermoreflectance[54, 55]. These methods each have their drawbacks and their strengths. We have used both techniques to characterize the samples discussed

in this thesis with reasonable agreement. Both of these techniques have large errors (~15-20%) associated with the measurement due to the sensitivity of the measurement setup and low signal to noise ratios. An overview of the measurements will be discussed in this chapter.

2.4.1 3ω Method

The 3ω method is the simpler and cheaper of the two measurements to set up. It also requires more sample processing to run the measurement. Furthermore, proper electrical isolation from conducting substrates must be achieved since this technique relies on an electrical signal to measure temperature differences. This is the method we have used at UCSB. The 3ω method was developed by David Cahill to measure the thermal conductivity of bulk materials in 1990 and later adapted to thin films[52, 53]. The basic principle of the 3ω method is that a heater wire is placed in good mechanical contact with the sample, but electrically isolated. An AC current is driven across the heater wire as shown in Figure 2.4 (below), which causes a temperature rise through the sample due to joule heating. This temperature rise is proportional to the third harmonic voltage.

$$\Delta T = 2\frac{dT}{dR}\frac{R}{V_{1\omega}}V_{3\omega} \qquad (2.1)$$

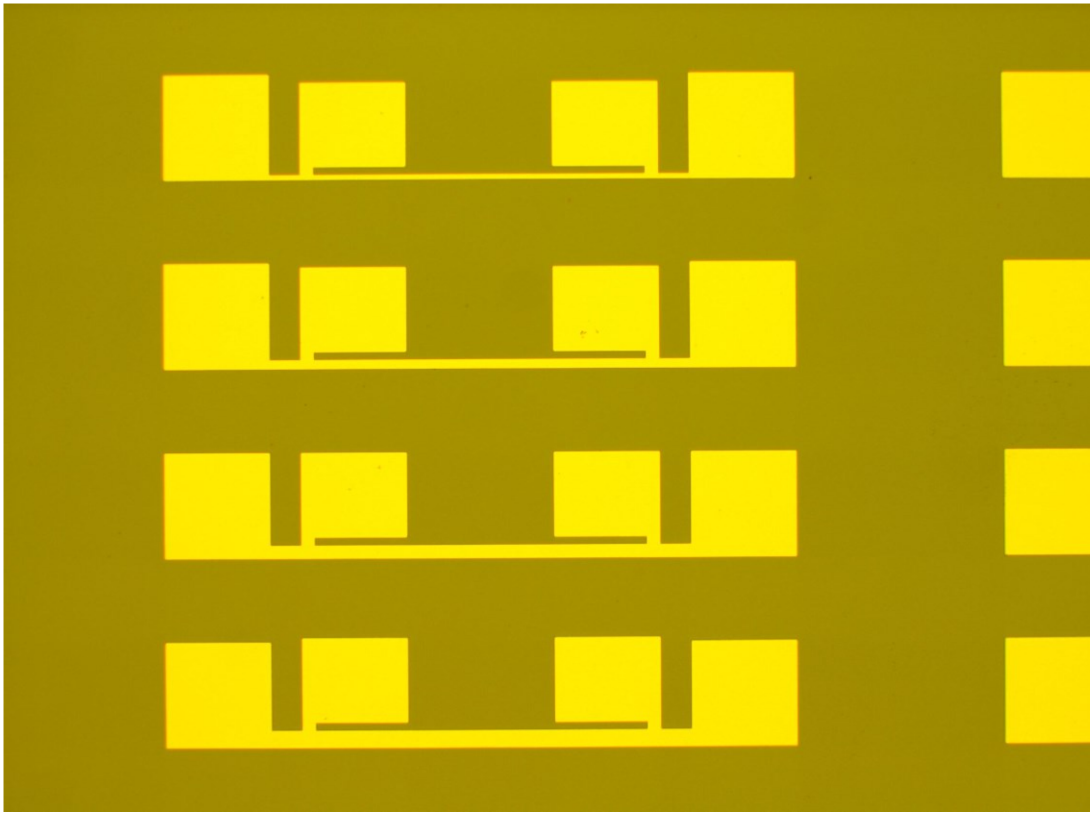

Figure 2.4 3ω schematic
This is an array of heater wires with different widths (power) to create a cross plane temperature difference to measure thermal conductivity.

When a reference sample containing the same structure except for the film is measured using the same technique, the temperature difference across the film for a given input power can be calculated. Using a known film thickness, the thermal conductivity can be calculated by:

$$\kappa_{film} = \frac{P * d}{w * l * \Delta T_{film}} \qquad (2.2)$$

Where P is the power of the heater wire, d is the thickness of the film, w is the effective heater width accounting for heat spreading[56], l is the length of the heater wire, and ΔT is the temperature drop across the film calculated from the third harmonic voltage. More details about the measurement setup and analysis are given in Woochul Kim and Joe Feser's dissertations[57, 58].

In this work, a 200nm SiO_2 electrical isolation layer was deposited on InGaAs films. 50nm/350nm Ti/Pt heater wires were deposited after electrical isolation. For high temperature thermal conductivity measurements, the heater wires must be annealed hotter than the measurement will go in order to ensure that phase changes do not change the electrical properties of the Pt heater wire. Thermal losses from the electrical isolation layer and thermal interface resistance can contribute error to this measurement. Thicker films are preferred in order to measure larger temperature differences across a film and minimize boundary resistance.

2.4.2 Time Domain Thermoreflectance (TDTR)

Time domain thermoreflectance is a newer method to measure thermal conductivity[54, 59]. This method is often preferred to the 3ω method because it can accurately measure the thermal conductivity very thin films.

These measurements were conducted by Joe Feser at UIUC. An Al transducer is deposited on the InGaAs films and is pulsed with less than 28mW laser at a modulation frequency of 1.1MHz. This pump beam effectively heats the sample with a corresponding steady state temperature increase less than 6K. A delayed probe

beam is pulsed to measure the temperature decay over time by measuring the change in reflectance of the Al transducer[54, 60].

One drawback to TDTR in the InGaAs material system, is that the fast modulation frequency of laser pulses cannot capture the entire range of phonons that contribute to thermal conductivity. Contributions from many of the longer wavelength phonons will not be captured in such high frequency measurements. In material systems that have a contribution to thermal conductivity from long wavelength phonons, this leads to artificially low thermal conductivity measurements. Incorporating ErAs nanoparticles is said to reduce the longer wavelength dependence to thermal conductivity, reducing error from this measurement[55]. Using a low modulation frequencies less than 1.1MHz should allow longer wavelength phonons to be measured, further reducing error. However, errors in setting the phase for low modulation frequencies leads to errors ~15%, compensating gains from capturing contributions from longer wavelength phonons.

2.5 Summary of Measurements

In summary, this section describes the main characterization techniques used in this dissertation, including electrical conductivity, Hall, Seebeck and thermal conductivity measurements. Further detail of relevant measurements will be discussed throughout the thesis.

Chapter 3

3 Si Doped InGaAs: an Experimental Base

This dissertation aims to understand how doping InGaAs with rare earths instead of traditional dopants like Si affect the thermoelectric properties. InGaAs lattice matched to InP is used as the material of choice for a number of reasons. The ~50:50 ratio of In:Ga maximizes the thermal resistivity due to phonon alloy scattering in the ternary semiconductor[61], while being lattice matched to the InP substrate allows high quality crystals to be grown with superior control over electrical properties. Furthermore, the Fermi level of ErAs has been shown to lie ~100meV below the conduction band edge of InGaAs[33], requiring activation of carriers at high temperature. To understand the dopant properties of rare earths in InGaAs, a comprehensive control study must be done to experimentally verify how traditionally doped InGaAs behaves. In this chapter, we discuss InGaAs growth conditions and study Si doped InGaAs over a wide range of carrier concentration to understand how InGaAs behaves as a thermoelectric without exotic dopants.

3.1 InGaAs Growth

This section details the MBE growth conditions of InGaAs grown heteroepitaxially on an InP substrate. InGaAs growth has a number of issues that InAs or GaAs homoepitaxy does not have because InGaAs is grown on a different

(InP) substrate. InP is used as a substrate because InGaAs can be grown lattice matched to it. Since there is no phosphorous source in the MBE used for these growths, removing the oxide and growing proper buffer layers becomes a crucial part of achieving high quality films. In this work, I have optimized the growth conditions, which have been confirmed with higher photoluminescence intensity and lower background impurity concentrations which will be described in this chapter.

To begin, a modified VG V80H solid source MBE system was used to grow $In_{0.53}Ga_{0.47}As$ (InGaAs) with an $In_{0.52}Al_{0.48}As$ (InAlAs) buffer layer on InP (001) substrates with an As_4 overpressure. These compositions were chosen because both the InGaAs and InAlAs are lattice matched to InP. Conventional effusion cells were used for Ga, In, Al and Si, and a valved cracker for As. For each sample, the wafer's native oxide was desorbed at 490°C under an As_4 overpressure and monitored with Reflection High Energy Electron Diffraction (RHEED).

Both InP and III-As compounds have a (2x4) surface reconstruction for a group V rich surface and a (4x2) reconstruction for a metal rich surface[62]. It is necessary to grow in the group V rich regime to avoid metal from accumulating on the surface. During growth in the group V rich regime, the group V element has a sticking coefficient less than one at growth temperatures, which prevents excess group V from accumulating. For InP, the oxide desorption process is tricky due to the thin layer of native oxide that makes it difficult to distinguish in RHEED when oxide desorption is complete[63]. If the substrate temperature is held at a streaky 2x pattern, subsequent growth of thick layers can lead to surface roughening due to

incomplete oxide desorption, particularly on larger, 2 inch, substrates. In order to maintain temperature uniformity, long settle times are used. Higher quality crystals were grown when the substrate was taken past the initial oxide desorption point until the surface changed from group V to group III rich. This is evidenced by the RHEED reconstruction change from (2x4) (group V rich) (4x2) (group III rich) around 520˚C. The transition to a metal rich surface occurs due to the decreasing sticking coefficient of P and As at high temperatures. Because this transition is dependent on As overpressure, the temperature at which the transition occurs can be suppressed by increasing the As overpressure from 3×10^{-8} mbar to 1×10^{-7} mbar.

Figure 3.1a-b shows the transition from group V rich to metal rich. The [011] direction shows the clearest transition of 2x to 4x and was used the determine a clean surface ready for epitaxial growth. Because the [0-11] is the fast diffusion direction, its surface is too rough to accurately determine oxide desorption until the surface is well into the metal rich regime. It is important not to take the sample too hot in the metal rich regime because In will desorb from the surface in addition to As and P, irrecoverably decomposing the crystal and rendering the sample unusable. The oxide desorption process was used to calibrate a pyrometer from which subsequent temperatures during growth were adjusted.

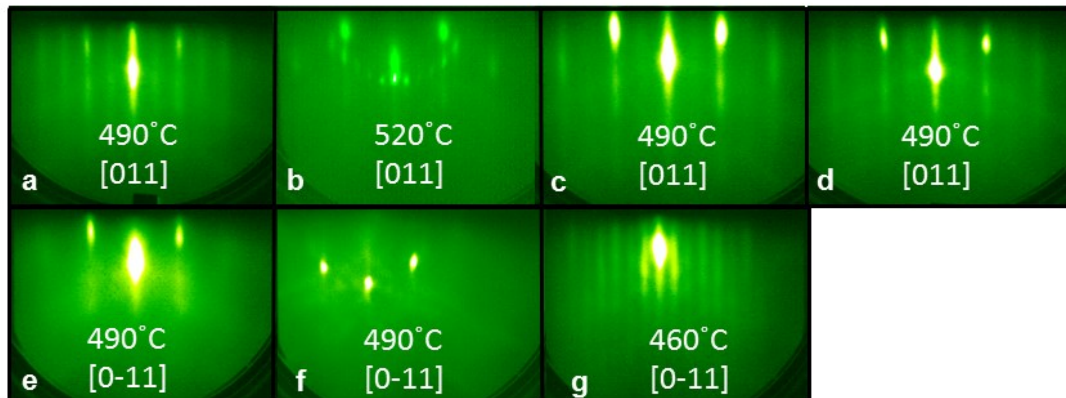

Figure 3.1 RHEED of InGaAs Growth

RHEED images depicting the different stages of InGaAs growth. The top row is taken along the [011] direction and the bottom row is taken along the [0-11] direction. In the [011] direction, RHEED during a) oxide desorbing from InP, b) transition to metal rich surface, c) recover As rich surface before growth, d) growth of InGaAs. In the [0-11] direction, RHEED during e) growth of InGaAs, f) annealing after growth at 490°C, and g) cooling down to 460°C under As4 overpressure.

Using InP substrates, during oxide desorption, a thin layer of InAs may form from an As-P exchange reaction as shown in Figure 3.2 [63–65]. A monolayer thick InAs layer shown in Figure 3.2 from growth initiated after annealing the substrate to 570˚C, but maintaining a (2x4) reconstruction due to a high As_2 overpressure of $1x10^{-5}$ Torr. Since the surface cleaning procedure in this work transitioned to a group III rich surface, it is likely that a thicker InAs interfacial layer (2-3ML) is present in our films[63]. This InAs layer can act as a parallel conduction path since the Fermi level is pinned in the conduction band[66, 67]. For this reason, it is important to electrically isolate the InP interface from the active region of the film for electrical measurements.

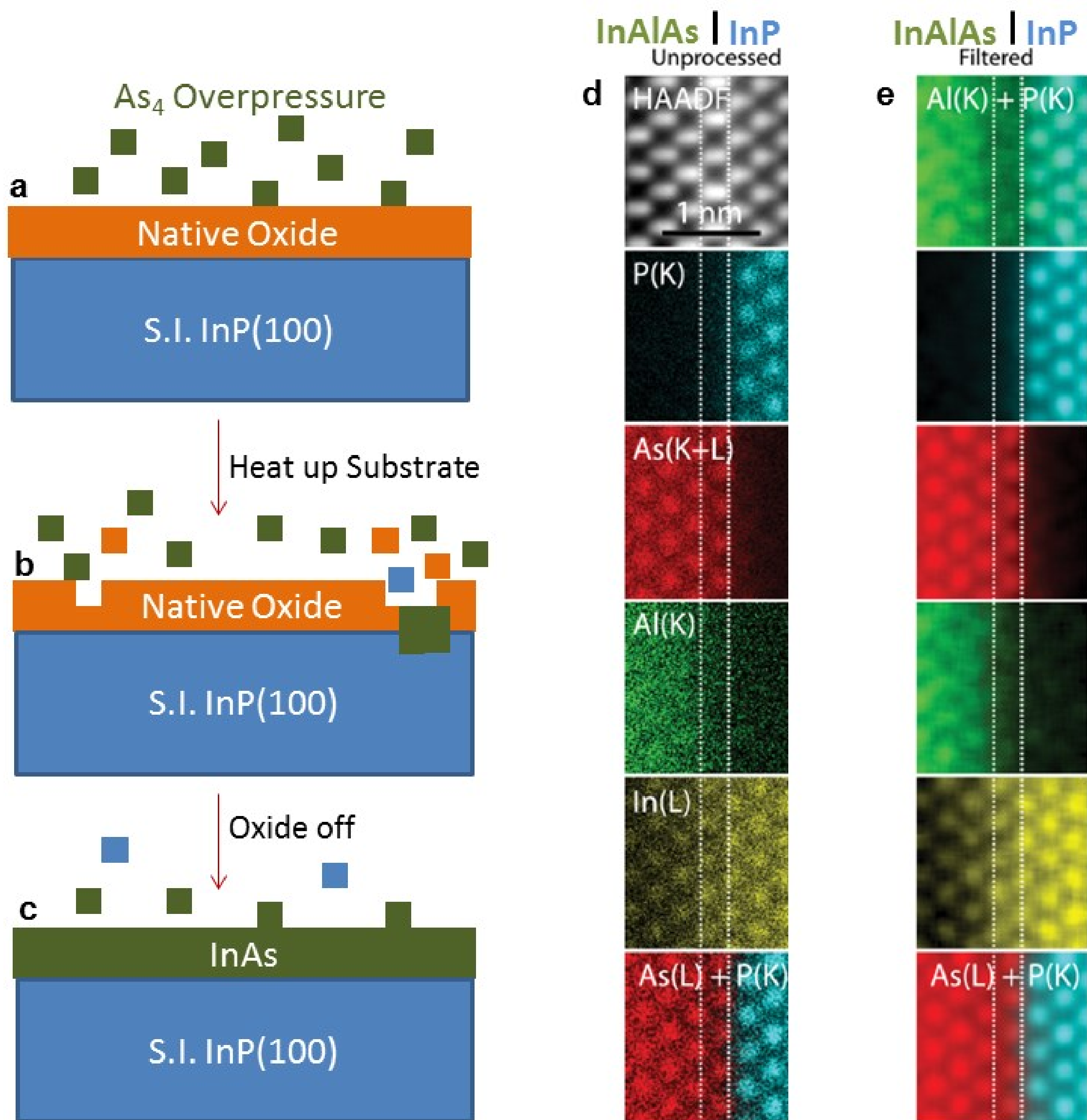

Figure 3.2 Schematic of Oxide Desorption on InP by MBE
Schematic depicting the oxide desorption process in MBE for heteroepitaxial growth of III-As compounds on InP. a) cold InP substrate is loaded into growth chamber with a native oxide layer protecting the InP surface. b) as the substrate is heated in an As overpressure, the oxide begins to desorb and the As embeds into the InP as P is desorbed. c) the oxide has fully desorbed and ~1 monolayer of InAs covers the InP substrate before growth begins. d) An unprocessed STEM image with Energy Dispersive Spectroscopy (EDS) map characterizing the elemental distribution in the InAs interfacial layer between InAlAs on an InP substrate and e) a filtered image highlighting the compositions in different layers[64].

After the substrate is annealed at the transition to group III rich surface for ~10 min, the sample is cooled down to the growth temperature of 490°C. During this cooling period, the surface should recover its group V rich surface as shown in Figure 3.1c. The surface becomes noticeably rougher in RHEED, necessitating the use of a buffer layer to smooth the surface. During ternary growth, the 2x RHEED pattern is not as strong, but still visibly present. Because of the disorder from the random alloy of InAs and GaAs, the [0-11] direction has a less sharp RHEED pattern during growth as shown in Figure 3.1e, which can only be described as a disordered 1x. Annealing at growth temperature smoothes the surface in this direction as noted by the distinct RHEED spots, but the reconstruction is still disordered. The [011] direction has a less distinct disordered 2x RHEED pattern during annealing, so annealed surfaces are characterized on the [0-11] direction. In an As rich environment, the [0-11] direction goes from a disordered 1x at 490°C, to an ordered 3x at ~460°C, consistent with reports in literature at this temperature[68].

The growth rate and composition of InGaAs and InAlAs layers was calibrated with RHEED oscillations during InAs, GaAs, AlGaAs, InGaAs, and InAlAs growth and confirmed with x-ray diffraction. Initially, individual cells are calibrated with RHEED oscillations to determine the flux over a wide range of temperatures. Using these calibrations, an estimate for the lattice matched condition is found. A lattice matching calibration sample is then grown choosing the calculated cell temperatures

and varying the Ga/Al cell temperatures in increments of 2-3 degrees while maintaining the In cell temperature constant.

X-ray diffraction was used to determine more precisely the lattice matched condition. In order to distinguish between the different peaks, a triple axis scan must be used. The slit in the detector for the triple axis, sharpens the peak widths so that they are easily distinguishable with ~0.2° separation in 2Theta. The layers must not be too thin because this leads to peak broadening, or if they are less than 30nm, strained layers. 200nm thick layers have relatively sharp peaks for identifying layers of similar composition. Figure 3.3a shows an InGaAs lattice matching calibration sample. Here, 5 different layers varying the Ga cell temperature by 2°C are clearly visible. The shoulder to the left of the InP peak is used as the "lattice matched" condition. It is important to note that even the most lattice mismatched peak here has less than 0.5% mismatch with the substrate. To determine the growth rate of InGaAs, in addition to using RHEED oscillations, a superlattice can be grown of 18nm InGaAs/1nm InAlAs. Clear thickness fringes that correspond to a superlattice period of 19nm as shown in Figure 3.3b can be correlated to growth times to determine growth rate.

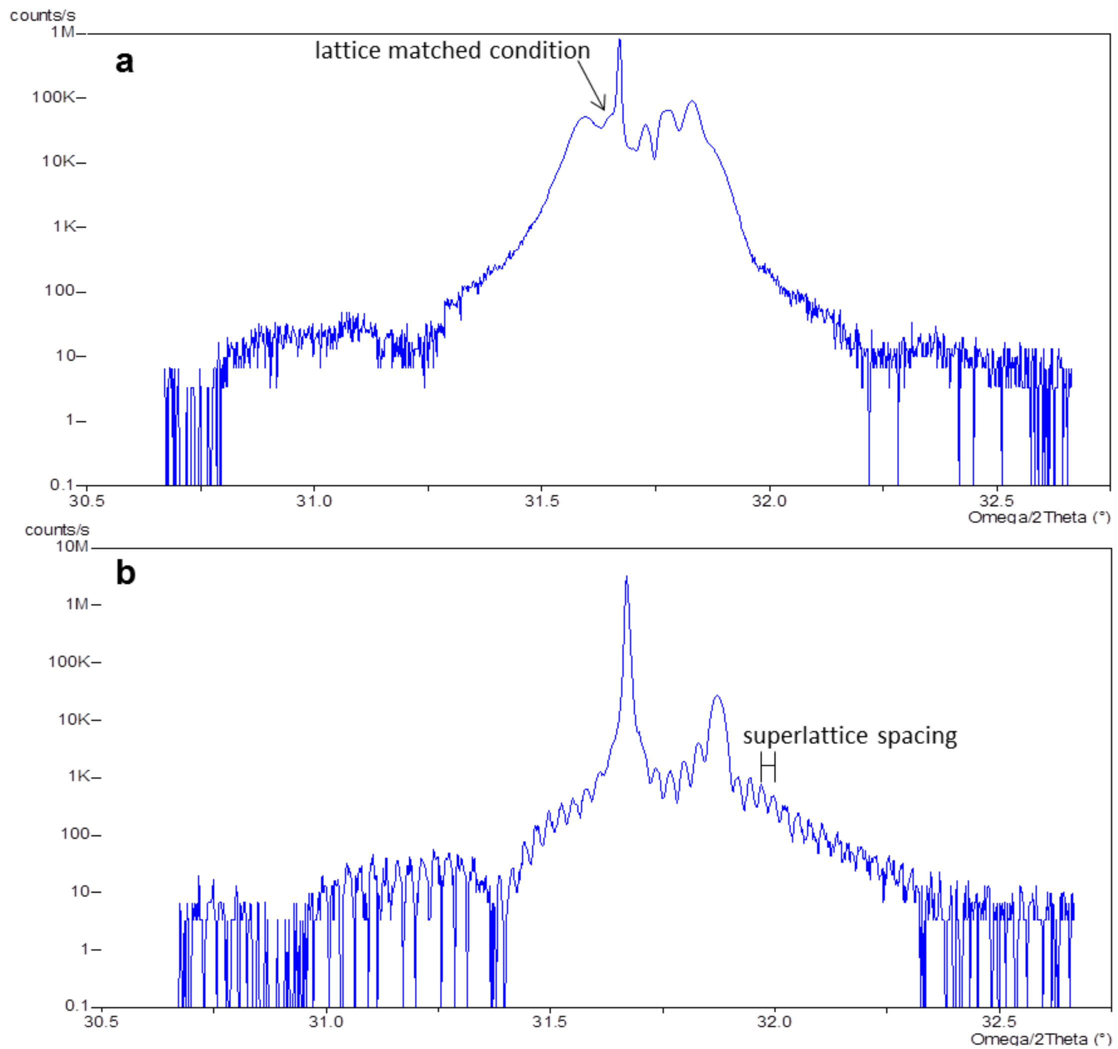

Figure 3.3 X-ray Characterization

a) X-ray diffraction using triple axis scan on the InP (004) peak to determine which layer is lattice matched. B) Triple axis scan to determine the superlattice period of 19nm as shown by the superlattice spacing.

For thermoelectric measurements, a 200nm thick InAlAs buffer layer was grown at 490°C over the InAs interfacial layer with the intent of minimizing parallel conduction in the InAs during electrical transport measurements. InAlAs has almost twice the bandgap of InGaAs and a conduction band offset of 500 meV that keeps

carriers confined to the InAs interfacial region. The bandgap of InAlAs straddles InGaAs, so it blocks both electrons and holes as an effective back barrier to InGaAs as shown in Figure 3.4. It is important to note that there is parallel conduction due to this InAs interfacial layer.

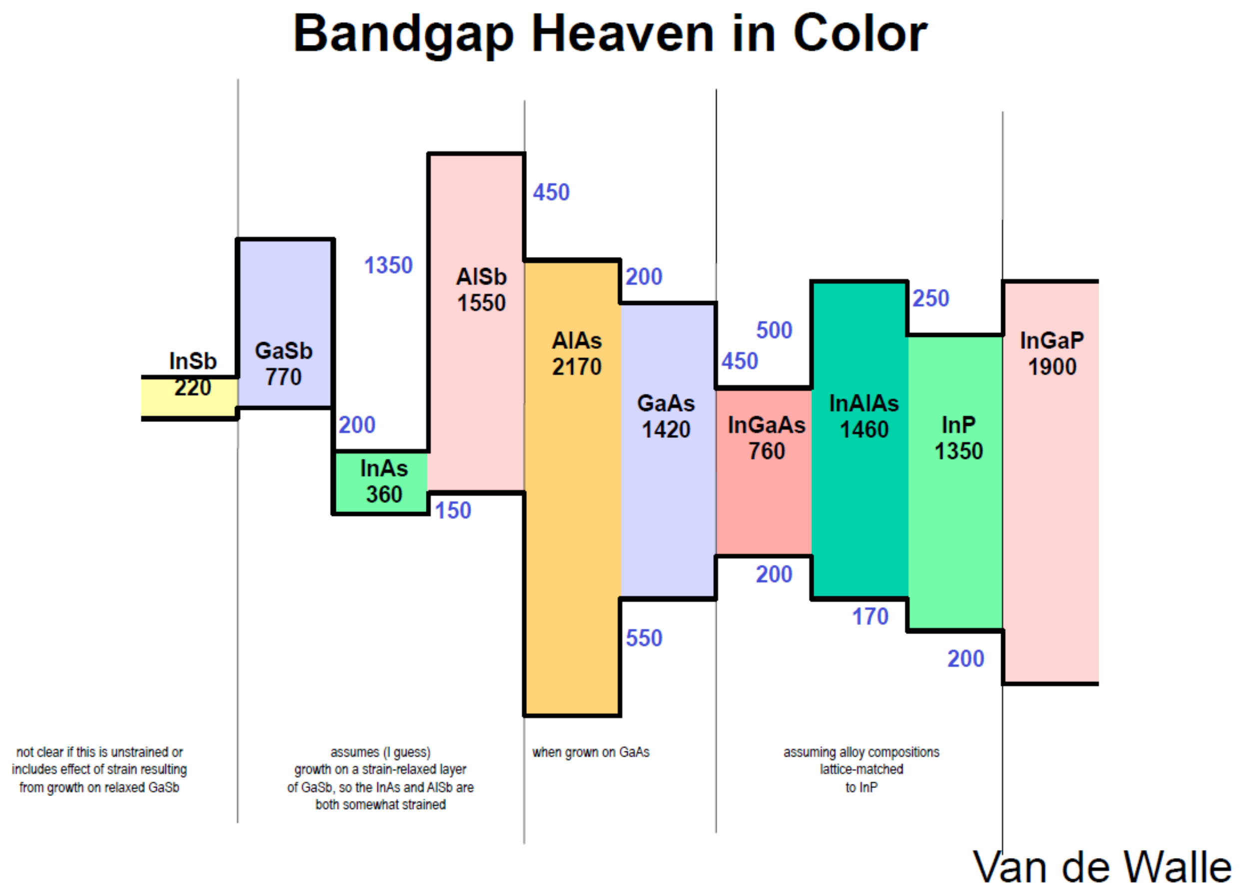

Figure 3.4 Bandgap Heaven
Schematic of the band alignment of various III-V semiconductors. Image courtesy of Chris Van de Walle.

The buffer layer creates an atomically clean, smooth surface for InGaAs growth. Next, InGaAs active layers were grown 4µm thick at 490°C at a rate of 1 µm/h and a

V/III beam equivalent pressure of ~10. Thick films ensure minimal contribution from parallel conduction in the InAs interfacial layer during electrical measurements and that low conductivity films are not completely depleted. Figure 3.5 verifies that undoped InGaAs films with an InAlAs buffer layer have higher crystal quality than films with an InGaAs buffer layer as noted by the higher intensity and sharper PL peak at 10K for InGaAs with an InAlAs buffer layer. The sample with an InGaAs buffer had a background carrier concentration of 10^{16} cm^{-3}, while the sample with an InAlAs buffer had a background carrier concentration of 10^{15} cm^{-3}, effectively isolating carriers in the InGaAs active region and minimizing parallel conduction.

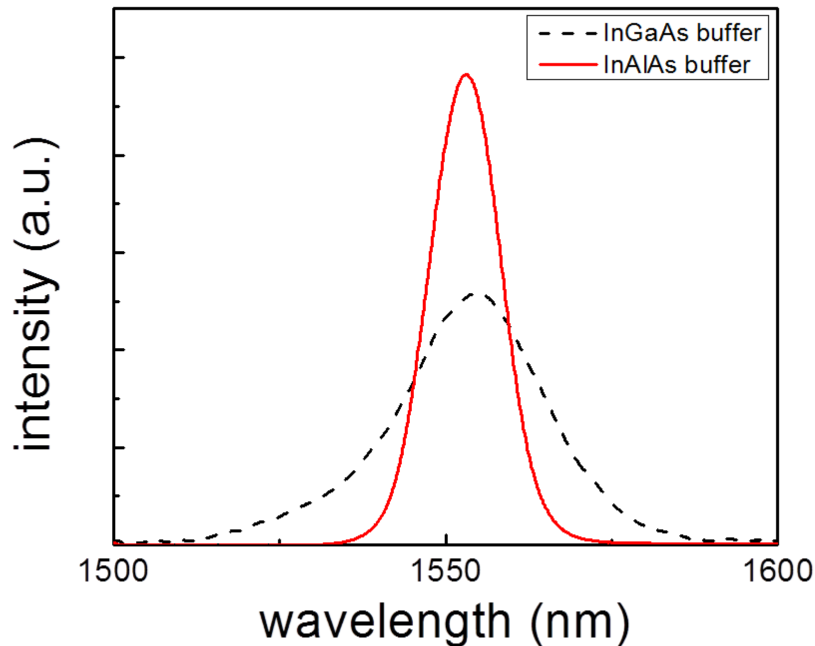

Figure 3.5 Photoluminescence of Isolated InGaAs
Photoluminescence at 10K of InGaAs on InP with an InGaAs buffer layer (black dashed line) has much lower intensity and broader peak than InGaAs with an InAlAs buffer (red solid line).

3.2 InGaAs Thermoelectric Properties

3.2.1 Doping with Si

For baseline thermoelectric measurements, silicon was incorporated in $In_{0.53}Ga_{0.47}As$ (InGaAs) films by codeposition. Si is an amphoteric dopant in III-V semiconductors, meaning that the impurity can sit on either a group III site as a donor or on a group V site as an acceptor. Studies have shown that at low Si concentrations and in a group V rich growth environment, Si preferentially sits on a group III site, acting as a donor[69, 70]. At high Si concentration, the percentage of Si on group V sites increases, eventually having a comparable concentration to Si sitting on donor sites. This compensation is exemplified by the decrease in electrically active carrier concentration from Hall measurements in Figure 3.6[71, 72]. No difference in doping efficiency is seen when As_4 is cracked to As_2.

The amphoteric doping properties of Si limit its doping efficiency, particularly at high growth temperatures. When Si sits on a group III site, it contributes one electron into conduction. Since the conduction band edge of InGaAs is lower than GaAs, the donor level of Si is shallower. At room temperature, Si should be a fully ionized donor.

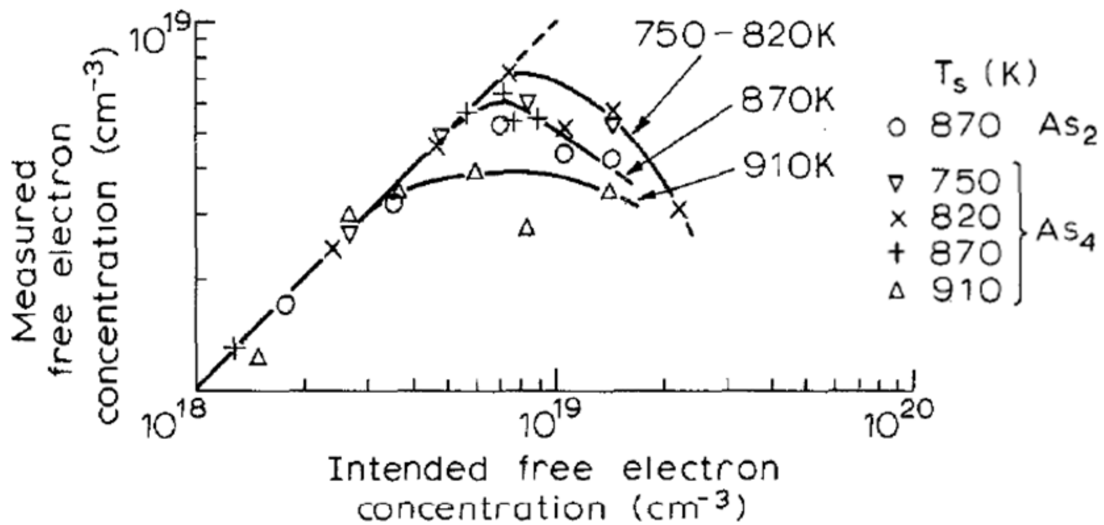

Figure 3.6 Si as an Amphoteric Dopant in GaAs
The Si flux verses measured carrier concentration. Doping efficiency of ~100% is seen until Si fluxes above 3x10^{18} cm^{-3}, at which point an appreciable concentration of Si sits on As sites, acting as acceptors that compensate the donor Si [71].

In these experiments, the Si flux was calibrated by Hall measurements of Si doped GaAs. Hall measurements give information on the net carrier concentration in a material, so if there is a large amount of compensating carriers, it will not give a good estimate of Si flux. Based on previous work as discussed earlier, it is assumed that the doping efficiency of Si doped InGaAs is roughly 100% over the concentrations studied, since InGaAs typically has higher solubilities than GaAs. It is seen in Figure 3.7, that even at 1x10^{19} cm^{-3} Si concentration, the Si cell calibration to predict carrier concentration is very accurate and no signs of amphoteric doping are seen at the Si concentrations studied. The Si calibration at low concentrations is not as accurate at predicting carrier concentrations from Hall measurements since the

background impurity concentration can affect the total carrier concentration in this regime.

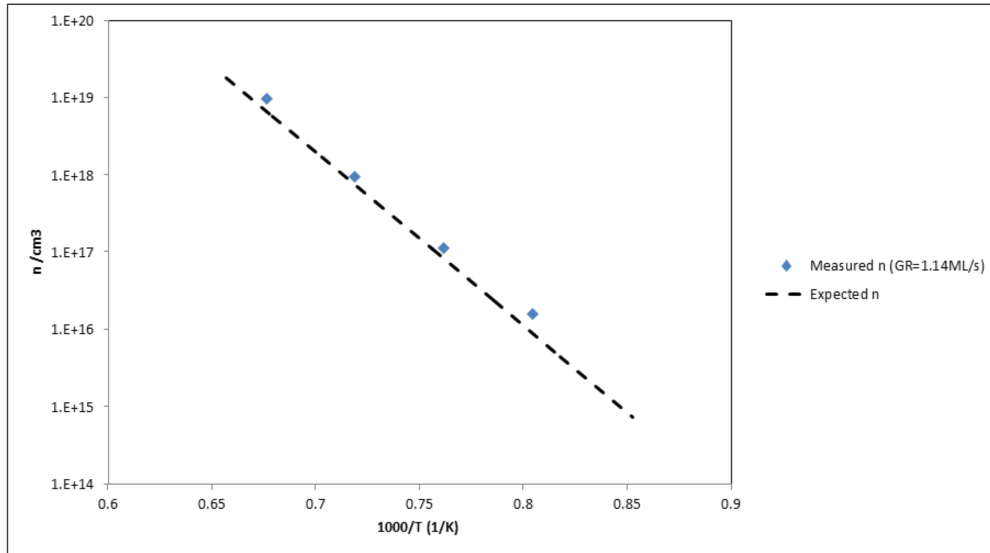

Figure 3.7 Si Doping Calibration
Measured electrically active carrier concentration compared to the expected carrier concentration from Si doped InGaAs.

3.2.2 Room Thermoelectric Properties of Si doped InGaAs

Figure 3.8 shows the room temperature thermoelectric properties of Si doped InGaAs from 10^{16} cm^{-3} to 10^{19} cm^{-3} electrically active carrier concentration and compares it to unintentionally doped InGaAs. Undoped InGaAs has a much lower electrical conductivity, and therefore ZT, than Si doped InGaAs.

The electrical conductivity of InGaAs increases proportional to the Si incorporation. An inverse relationship between carrier concentration and Seebeck coefficient is seen, consistent with single parabolic band transport. Note that all of the Seebeck coefficients were negative since Si is an n type dopant in InGaAs. The

absolute value of the Seebeck coefficient is plotted because it contributes a squared term to ZT. Lastly, thermal conductivity measurements by time domain thermoreflectance (TDTR) show that below 10^{18} cm^{-3} carriers, the thermal conductivity of InGaAs remains unchanged within the error of the measurement. The thermal properties of a material are much less sensitive to impurities than electrical properties. At 10^{19} cm^{-3} carriers, the thermal conductivity of InGaAs increases due to the electronic contribution to thermal conductivity rising from the Wiedemann-Franz law. This effect and how it can be overcome will be discussed in more detail in Chapter 5.4.

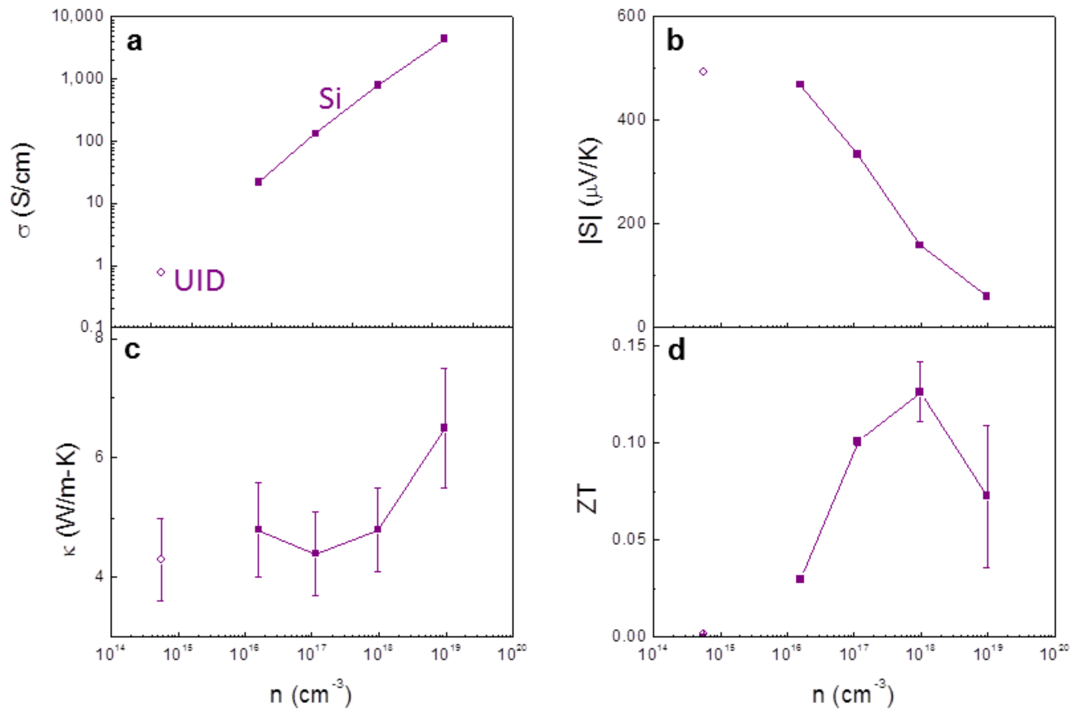

Figure 3.8 Thermoelectric Properties of Si Doped InGaAs
a) electrical conductivity, b) Seebeck coefficient, c) thermal conductivity and d) ZT of Si doped InGaAs as a function of carrier concentration at room temperature.

Overall, a maximum ZT=0.126 is achieved at 300K for 10^{18} cm^{-3} Si concentration as a result of the inverse relationship between electrical conductivity and Seebeck. The decrease in ZT above 10^{18} cm^{-3} carriers is exacerbated by the sharp increase in electronic contribution to thermal conductivity due to the Wiedemann-Franz Law. Overall, the reduction in thermal conductivity by alloying InAs and GaAs provides an order of magnitude enhancement in ZT while maintaining tunable electrical properties.

3.2.3 Low Temperature Transport

In order to understand how rare earths behave as exotic dopants in InGaAs, the transport mechanisms of Si doped InGaAs must be examined. Low temperature transport can give insight into different scattering mechanisms and doping properties such as activation energies of dopants. In general, temperature dependent transport of traditional III-V semiconductors is well understood and detailed information can be found in standard textbooks like S.M. Sze's *Semiconductor Device Physics*[73], where much of this analysis is taken from. Figure 3.9 shows the low temperature electrical transport properties of Si doped InGaAs compared to unintentionally doped InGaAs.

It can be seen that unintentionally doped InGaAs has the highest mobility over a range of temperatures and the highest doped sample, 10^{17} cm^{-3} Si, has the lowest mobility. Ionized impurities scatter carriers, therefore decreasing the mobility. These differences are exacerbated at low temperature, as will be discussed shortly, but remain quite large at room temperature as well. Note that the mobility is plotted on a log scale.

At low temperatures, carriers have little thermal energy and are therefore strongly scattered by ionized impurities. As temperature increases, carriers have more thermal energy to overcome the Coulomb forces of the impurity. Essentially, carriers spend less time close to impurities when they have more thermal energy, so impurities do not scatter as strongly. This causes the mobility to increase with temperature. At some point, there is so much thermal energy that the lattice vibrations, or phonons,

cause enough of a disturbance in the periodicity of the lattice that they cause carriers to scatter more strongly than impurities do. In this regime, mobility decreases with temperature. In the unintentionally doped sample, there are so few impurities that phonon scattering dominates mobility at 10K. By the time 10^{17} cm^{-3} carriers are reached, impurity scattering dominates until 80K. This is evidenced by the peak in mobility seen shifting to higher temperatures at higher impurity concentrations as well as more shallow decrease in mobility with temperature.

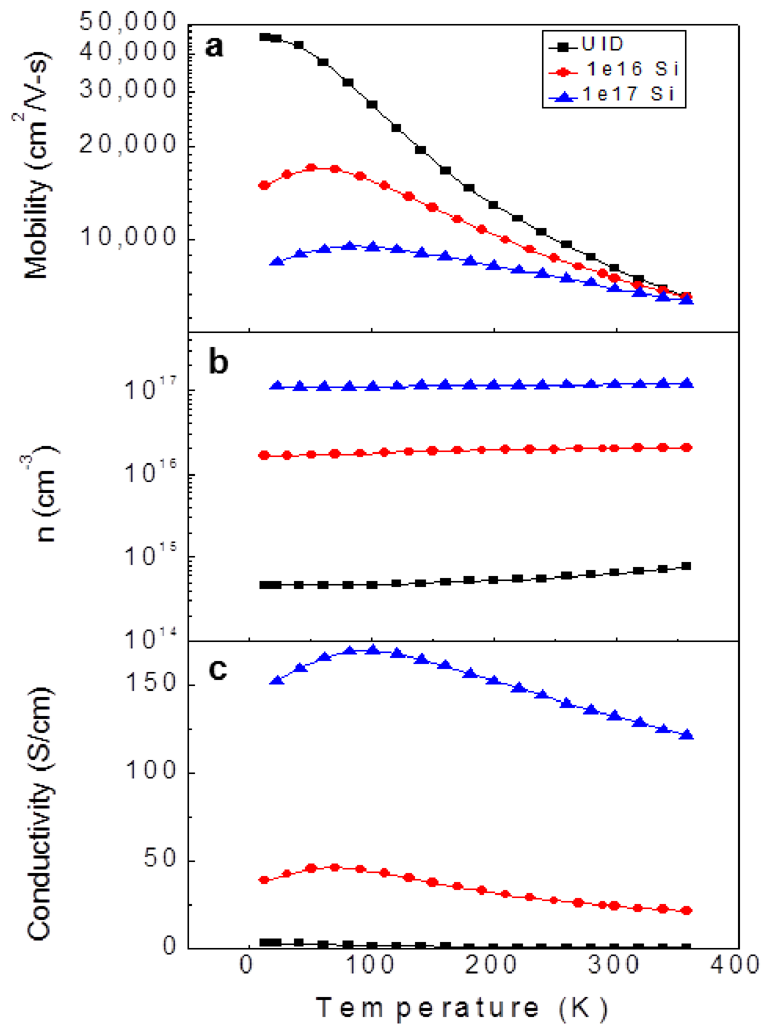

Figure 3.9 Low Temperature Transport of Si Doped InGaAs
a) mobility, b) carrier concentration, and c) electrical conductivity of Si doped InGaAs from 10-360K.

In nondegenerate semiconductors, carriers freeze out at low temperatures when there is not enough thermal energy to excite carriers from the impurity state into conduction. In Figure 3.9b, there are no signs of carrier freeze out, so the activation energy of Si cannot be experimentally verified at this temperature range. This is due to the fact that even at the lowest Si concentrations used, the dopant concentration is

above the Mott metal to insulator transition of ~2×10^{15} cm^{-3}. Since the radii of the donor atoms overlap at these high Si concentrations, an impurity band is formed. Furthermore, the Si impurities in the InGaAs matrix disrupt the periodicity so that the conduction band edge is broadened, even at low temperature, overlapping with the impurity band. This leads to band conduction through the donor impurities, even at low temperatures. Since the impurities form a band and do not need to be thermally ionized, the determination of activation energies from Si dopants at concentrations used for thermoelectrics is not feasible.

Even in unintentionally doped InGaAs, only a slight thermal activation of carriers is seen. In this regime, unintentional impurities, such as C or O, play a big role in transport. More precise characterization of the impurities in unintentionally doped InGaAs through techniques like Secondary Ion Mass Spectroscopy could lead to more information about transport in this InGaAs system. Overall, the electrical conductivity is higher for InGaAs with higher carrier concentration since doping with Si allows control of carrier concentration to many orders of magnitude. Temperature dependent trends are determined by the mobility, showing that higher impurity incorporation leads to a shallower decrease in mobility with temperature and a shift in the temperature where peak mobility occurs.

3.3 Conclusions from InGaAs Growth and Transport Properties

In summary, the growth and transport properties of InGaAs are reported. The heteroepitaxial growth of InGaAs films on InP by MBE is optimized for

thermoelectric applications and the benefits of using an InAlAs buffer layer are shown. The room temperature thermoelectric properties of traditionally doped InGaAs are discussed as a baseline to compare with rare earth dopants later in this thesis. A maximum ZT is seen at 10^{18} cm^{-3} carrier concentration. This maximum occurs at approximately 1-2 orders of magnitude lower carrier concentration than is typically seen in high efficiency bulk materials like Bi_2Te_3[8]. Lastly, low temperature Hall measurements illuminate different transport regimes at different temperatures depending on the impurity concentration. Ultimately, the most important tool we have to optimize the thermoelectric properties of InGaAs is changing the carrier concentration.

Chapter 4

4 ScAs Particles in InGaAs

This chapter examines the thermoelectric properties of ScAs nanoparticles embedded in an InGaAs matrix and compares it with alloyed ErScAs particles as well as previously studied Er particles. The embedded growth mechanism is discussed as well as atom probe tomography, which has been used as a novel way to image dilute nanoparticles when TEM is not a viable option.

4.1 ScAs nanoparticles

Embedding Er-V nanoparticles in III-V semiconductors has been shown to improve thermoelectric properties by effectively improving electrical conductivity while decreasing thermal conductivity[25, 26, 40]. In order to understand how these rare earths effect the thermoelectric properties, a survey of rare earths has been studied in InGaAs, including TbAs[45] and CeAs[14]. In this work, we explore Sc as a potential rare earth dopant in InGaAs for thermoelectric applications. Sc was chosen as a dopant in this because ScAs has the smallest lattice parameter out of all the rare earths, allowing us to study potential strain effects on thermoelectric properties. The small ionic radius and mass of Sc provides a strong material contrast to the lanthanide based particles. As the lightest rare earth, Sc allows us to investigate if these nanocomposite structures reduce thermal conductivity from

distortion to the lattice periodicity or from heavy atoms, such as Er, acting as "rattlers"[6, 74, 75].

4.1.1 Growth of Mechanism of Embedded ScAs Nanoparticles

Although not strictly speaking a rare earth element, Sc has the same valence structure with one d electron and is typically found in the +3 oxidation state. Sc is more similar in chemistry to the lanthanides than it is to Al or Ti. Thermodynamically, Sc reacts with As to form ScAs, which has the same favorable heat of formation as the majority of the RE-As compounds[27]. It has been shown that ScAs grows epitaxially on GaAs(001)[76] in the same way that ErAs is grown[77]. Previous studies report that rocksalt ScAs is the only Sc-As compound that forms under As rich conditions[78]. To understand why ScAs nanoparticles form in InGaAs during codeposition, it is necessary to first understand the growth mechanism of particle formation of a similar, well studied system: ErAs. There has been a lot of work to understand the growth mechanism of embedded Er-V particles in III-V semiconductors, and this can act as a basis for understanding ScAs[29, 37, 79–82].

When ErAs is initially grown on GaAs at 350°C, ErAs islands embed in GaAs and eventually coalesces into a continuous film after 3 monolayers (ML) deposition, at which point ErAs grows layer by layer[27]. Since we are interested in growing nanoparticles and not continuous films, we will look more closely at the first couple monolayers of growth.

As shown in Figure 4.1, after 0.1ML of ErAs growth on GaAs, the surface remains atomically flat, except where ErAs has formed into clusters. A (2x4) reconstruction of GaAs is maintained across the surface. After 0.5ML ErAs, the GaAs surface is significantly rougher, with 1ML step heights due to ErAs incorporation. These mounds maintain the GaAs (2x4) surface reconstruction, suggesting that they are As terminated GaAs. At 1ML of ErAs, there are dark ErAs features that are unreconstructed, suggesting ErAs island formation, surrounded by areas of GaAs reconstruction. This dark region increases in density until full ErAs coverage is reached[37, 83]. Due to the very large heat of formation of ErAs compared to GaAs, Er impinging on the GaAs surface kicks out a Ga atom and bonds with As. This leaves excess Ga on the surface which can react with the As overpressure to created a textured GaAs surface.

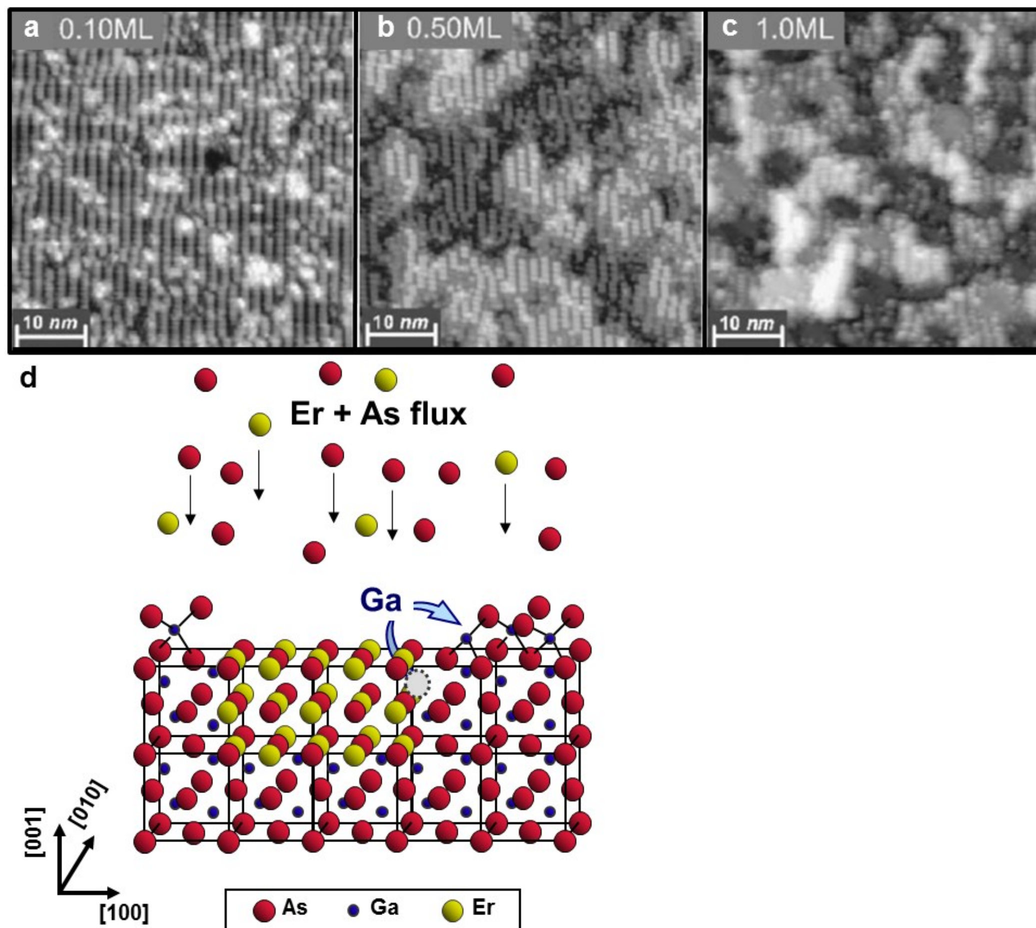

Figure 4.1 Embedded Nanoparticle Growth Mechanism
STM filled states image of ErAs growth on GaAs for a) 0.1ML, b) 0.5ML and c) 1.0ML. d) schematic illustrating how Er embeds into GaAs and kicks out Ga[37].

4.1.2 Codeposition of ScAs Particles

When codepositing Er with GaAs or InGaAs, above a solubility limit, ErAs particles form. ErAs nanoparticles have been observed in InGaAs above $8x10^{19}$ cm^{-3} Er concentration[42]. It has been shown that increasing the growth temperature can decrease the solubility limit of Er as well as increase anisotropy in the shape of

particles, leading to an optimal growth temperature of 490°C for thermoelectric applications[47]. Using these growth parameters, codeposition of Sc in InGaAs leads to high quality single crystal growth as evidenced from RHEED images before and after 4 μm thick nanocomposite film growth as well as X-ray diffraction shown in Figure 4.2. Along the [011] direction, a streaky 2x reconstruction is seen on both the InAlAs buffer layer and the 4um thick film of Sc doped InGaAs. A high intensity film peak is seen in the InGaAs layer with 0.07% lattice mismatch.

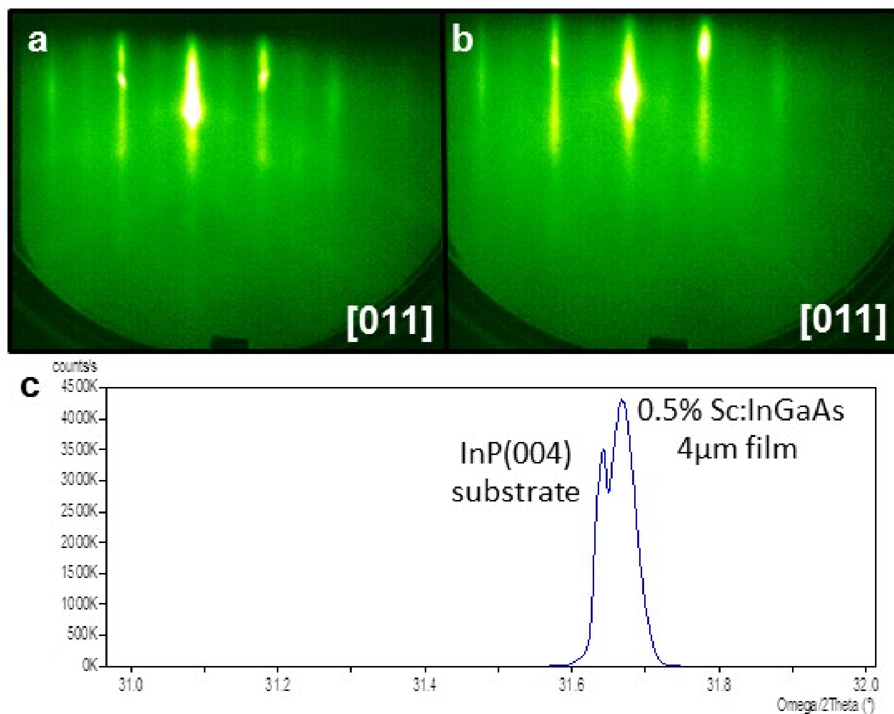

Figure 4.2 Sc Doped InGaAs RHEED
RHEED along the [011] direction of a) 200nm InAlAs buffer layer and b) 4um InGaAs doped with 0.6% ScAs. c) shows the small lattice mismatch between the InP substrate and the Sc doped InGaAs film.

4.1.3 Atom Probe of ScAs Nanoparticles

Since Sc doped InGaAs has not been thoroughly explored, it is important to confirm the presence of ScAs nanoparticles. This proves to be a difficult task because the traditional way of imaging these particles uses z-contrast in TEM. This works very well for high Z elements like Er, but Sc has a Z of only 21, making it difficult to discern Sc in particles from group III elements in the InGaAs matrix. Finding dilute nanoparticles from this contrast is not feasible and preliminary TEM results were not able to resolve nanoparticles in InGaAs. For this reason, atom probe tomography was used to build a reconstruction of the sample and analyze the presence of Sc clustering.

Atom probe tomography is a technique that uses a position sensitive, mass to charge time of flight detector to image individual atoms ablated from a sample, creating a compositional reconstruction of the sample. By detecting the mass to charge ratio of individual atoms, Sc can be easily discerned from the underlying InGaAs. Atom probe is a novel imaging technique that is not as widely known as techniques like TEM, so a brief overview of atom probe tomography will be discussed here.

Atom probe uses high electric fields at the ends of sharp features like nanowires or fabricated tips to ablate material. In our case, we used a focused ion beam (FIB) to mill out a wedge from the Sc doped InGaAs sample and place it on a prefabricated conductive Si post as shown in Figure 4.3a. The wedge is attached to the post with Pt and then milled with a Ga ion beam into a sharp tip as shown in Figure 4.3b. These

nanometer size tips are electrically and mechanically connected to conductive Si substrates as shown in Figure 4.3c.

An electric field is applied to the substrate, changing the energy landscape of an atom on the fabricated tip from the light green curve in Figure 4.3e, to the dark green curve. This new energy landscape has a local minimum, so that atoms on the surface are in a metastable state. In order to ablate the surface atoms on the tip, a localized laser pulse is applied to the tip. The energy from the laser pulse is enough for the surface atoms to overcome the metastable potential well and fly off of the sample as shown in Figure 4.3d. The ionized atom is then detected by the position sensitive time of flight detector (Figure 4.3c), which identifies the type of atom, where it came from and which layer (z-spacing) it belongs to.

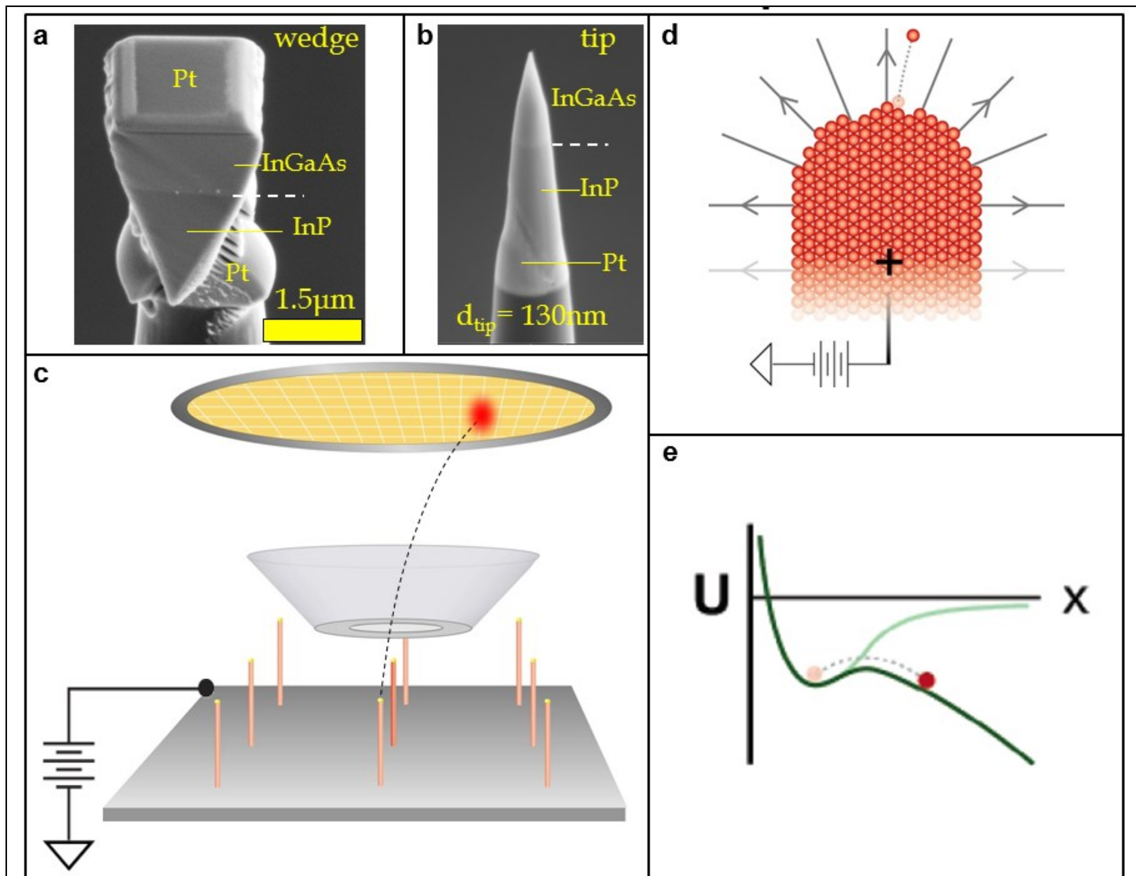

Figure 4.3 Atom Probe Schematic

a) Wedge of InGaAs placed on a Si post. b) atom probe tip milled with FIB. c) schematic of atom probe operation, d) electric field ablation of tip, and e) energy landscape of tip under applied bias and laser ablation[84].

Pulsed-laser atom probe tomography was performed using a Cameca Local Electrode Atom Probe 3000X HR system to confirm nanoparticle formation and investigate its properties. This technique uses a time of flight mass spectrometer coupled with a position-sensitive microchannel plate detector, enabling a three dimensional reconstruction of a sample's composition and structure at the nanoscale[85]. Atom probe samples were milled into tips with average diameters of

~135 nm using a focused Ga-ion in an FEI Helios Dual Beam FIB system[86]. The tip was cooled to 30K during atom probe tomography, and evaporated at an applied voltage between 4 and 6kV. Pulsing of a Nd:YAG 532nm laser at 100kHz and a pulse energy of 0.025nJ enabled controlled field evaporation from the tip surface. The applied voltage, laser pulse energy and frequency were tuned for controlled evaporation from the tip surface. If the parameters were not optimized, either no evaporation occurred, or very high electric fields would lead to many atomic layers ablating at once, essentially destroying the tip. The details of atom probe instrumentation and reconstruction algorithms can be found elsewhere[87, 88].

To provide some measurement of the ScAs nanoparticle distribution and size, atom probe tomography was performed on 2% ScAs:InGaAs nanocomposites. A concentration of 2% ScAs was used to ensure sufficient particle formation for statistical analysis while still allowing order of magnitude comparison to previous ErAs particle size measurements from TEM. Figure 4.4 shows representative distributions of the Sc, In + Ga, and As atoms based on these measurements. Without filtering any of the signal, the distributions of the group-III elements and As appear completely uniform, while the distribution for Sc shows significant texturing indicative of the clustering associated with ScAs nanoparticle formation. The curvature observed in the Sc signal is indicative of a lower evaporation field, confirming the semimetallic properties of the ScAs nanoparticles. An isoconcentration surface (Figure 4.4b) of high Sc content shows that there are ScAs clusters in the InGaAs film. A statistical analysis of the Sc distribution using a

maximum separation algorithm with the envelope and eroding method[89] implemented by the Imago Visualization and Analysis Software package roughly estimates the average diameter of isotropic ScAs clusters to be between 2 to 3 nm. This diameter is slightly larger than the 1.5-2 nm generally observed for ErAs nanoparticles[29]. However, it is difficult to make claims in the difference in particle size for Sc versus Er due to the fact that spatial resolution of atom probe relies heavily on nanostructures as a reference. For example, known superlattice spacings can be used to calibrate length scales of the atomic reconstruction. Since this film was a single 1 μm film with unknown size nanoparticles and an unknown portion of the top of that film was milled away in the tip fabrication process, the cluster analysis can only act as a way to determine the order of magnitude of the size of the particles.

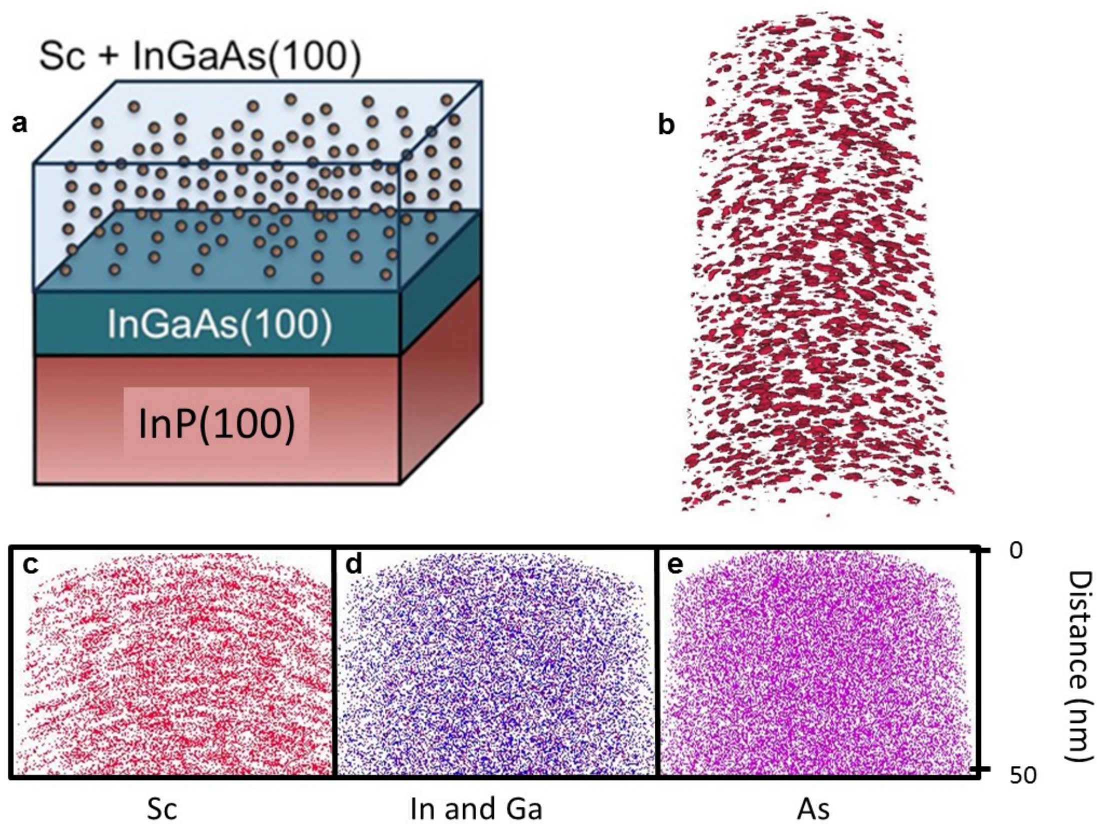

Figure 4.4 Atom Probe of ScAs Nanoparticles
a) Schematic of embedded ScAs nanoparticles in InGaAs. b) isoconcentration surface of high Sc content showing clustering. Signal for c) Sc, d) In and Ga, and e) As from atom probe.

4.2 Room Temperature Electrical Properties of ScAs Particles in InGaAs

Since ScAs nanoparticle formation has been confirmed, the effect of these particles on the thermoelectric properties of InGaAs can be explored. Figure 4.5 shows the electrical properties of Sc doped InGaAs over a range of ScAs incorporation. 200nm InAlAs buffer layers were grown on InP substrates to smooth the film and electrically isolate the active region from the interface with the InP

substrate as discussed in the previous chapter. 4 μm thick InGaAs with varying Sc incorporation was then grown to ensure that low conductivity films were not completely depleted. The Sc composition is chosen to begin below the expected solubility limit of Sc in InGaAs and continue to a concentration with dense nanoparticles. Since the error on Hall measurements is typically <5%, error bars cannot be seen on a plot of this scale. Furthermore, the stability of the Sc cell withing +/- 1˚C leads to variation in composition <0.02% depending on the Sc flux, also not visible on a plot of this scale.

The most striking feature is that Sc acts as an n-type dopant, increasing the electrically active carrier with a steeper slope with ScAs incorporation, until the carrier concentration starts to plateau above 0.1% ScAs concentration, where particles are believed to have forme, if assuming a similar solubility limit to Er[42]. It is also seen that the mobility of Sc doped InGaAs increases as more Sc is incorporated below the solubility limit. Once ScAs particles have formed, the mobility decreases with increasing impurity concentration, as expected. The inverse relationship between carrier concentration and mobility leads to a peak electrical conductivity at 0.5% ScAs incorporation. Lastly, a clear inverse trend is seen between the Seebeck coefficient and carrier concentrations, consistent with single parabolic band transport[18].

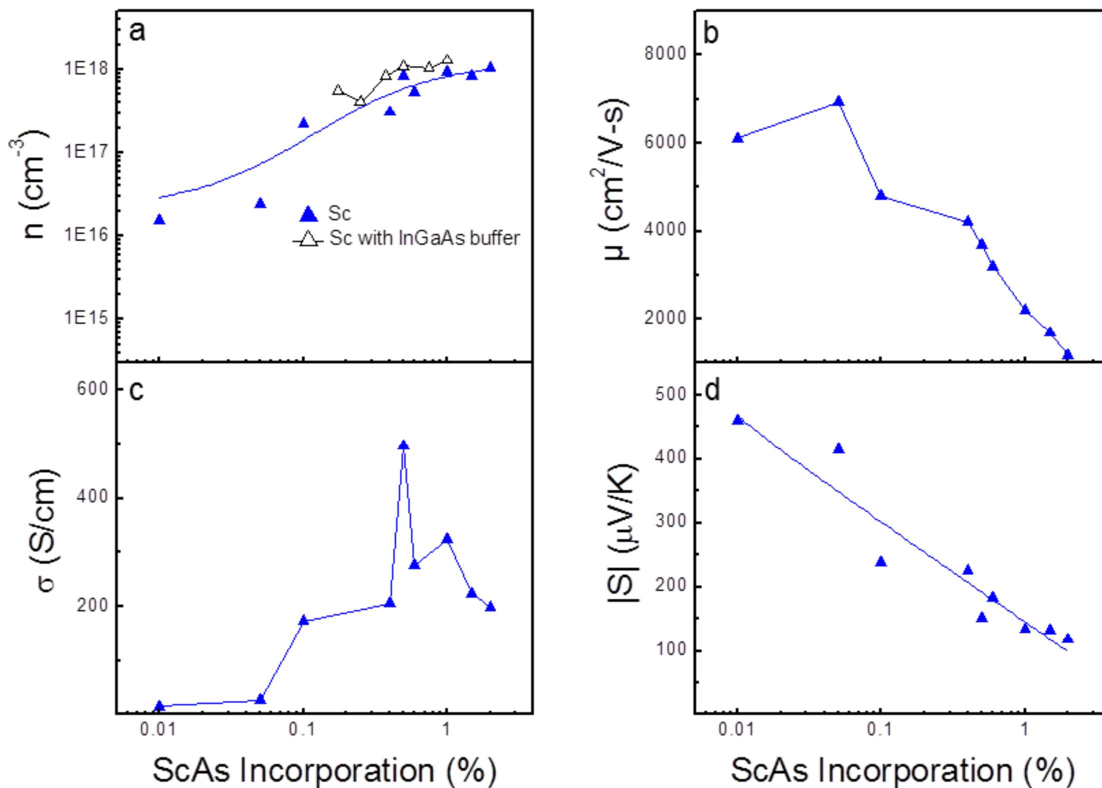

Figure 4.5 Electrical Properties of Sc Doped InGaAs
a) Carrier concentration, b) mobility, c) electrical conductivity and d) Seebeck coefficient as a function of ScAs Incorporation.

In the plot of carrier concentration vs ScAs incorporation, two trends are seen for the same ScAs incorporation. The open triangles are 1 µm thick Sc doped InGaAs grown on an InGaAs buffer layer at a growth rate of ~0.5µm/hr. Samples with InGaAs buffer layers were initially grown, but it can be seen that there is a higher measured carrier concentration for all of these samples. Analyzing possible error in Sc composition and Hall measurements show that differences shown in measured carrier concentration are representative of differences in transport in the samples. Error in the Hall measurements leads to deviations less than 5%, which cannot be

seen on the scale of carrier concentration represented in Figure 4.5. Furthermore, temperature fluctuations in the Sc cell during growth of 1-2˚C contribute deviations in composition less than 0.02%. The It is believed that the difference in measured carrier concentration is due to parallel conduction in the InGaAs buffer layer, since there is a very low barrier (if any) at room temperature to electron transport from this high carrier concentration InAs interfacial layer into the InGaAs buffer layer. Furthermore, it is probable that 1 μm thick layers have a larger 3D contribution from the InAs interfacial region formed during oxide desorption on InP discussed in Chapter 3.1. Higher 3D carrier concentrations were also seen for thinner unintentionally doped InGaAs films with InGaAs buffer layers. Lastly, it is possible that higher growth rates lead to Sc preferentially incorporating as atomic impurities rather than as nanoparticles, but this has yet to be properly investigated.

4.3 Room Temperature Properties of ErScAs particles in InGaAs

This section compares the electrical and thermal properties of rare-earth nanoparticle alloys embedded in InGaAs nanocomposites to determine whether alloying of the nanoparticles can be used as a means of further increasing thermoelectric efficiencies. The thermoelectric properties of single crystal nanocomposites formed by codepositing Er and Sc together with InGaAs were measured and compared to the thermoelectric properties of InGaAs nanocomposites formed with Er and Sc individually.

Rare earth nanocomposites were grown on semi-insulating InP(001) substrates by molecular beam epitaxy. A 100 nm undoped InGaAs buffer layer was grown at

490ºC to smooth the surface. Later experiments have shown that using an InGaAs buffer layer is not ideal for testing thermoelectric properties, as discussed in section 4.2. Following the buffer layer, a 1 μm thick active region was grown by codepositing the rare-earth elements along with the InGaAs. A growth rate of ~0.5 μm/hr was used for all samples and rare-earth concentrations ranging from 0.175% to 4% with respect to the total number of rare-earth and group-III elements deposited.

Hall effect and sheet resistivity measurements were performed using a Van der Pauw geometry and annealed indium contacts. The in-plane Seebeck coefficient was measured using two thermoelectric heating and cooling sources to maintain a temperature gradient while measuring the induced voltage difference as a function of the temperature difference via equidistant thermocouple and voltage probes. Thermal conductivity was measured in the thin films using the differential 3ω method[52, 53] with a corrected effective heater width to account for heat spreading[56] as described in section 2.4.1. A SiO2 layer was deposited on the surface to electrically isolate the sample followed by an 18 μm wide Pt thin film resistor with four bonding pads for the 3ω heating and voltage measurements.

The thermoelectric properties of three sets of single crystal InGaAs nanocomposites were measured as a function of rare earth concentration. The sets were formed by depositing either Sc, Er, or an equal mixture of Sc and Er with InGaAs. Codeposition with either Sc or Er is known to produce ScAs and ErAs nanoparticles embedded in the InGaAs. Nanocomposites codeposited with both Sc and Er are referenced simply as Sc+Er since it was not clear a priori whether

codeposition would produce $Sc_{0.5}Er_{0.5}As$ nanoparticles, separate ScAs and ErAs nanoparticles, or some convolution of the two embedded in InGaAs. Thin films of $Sc_{1-x}Er_xAs$ form a solid solution[27, 76], and as will be discussed shortly, even at dilute concentrations, the nanoparticles appear to alloy as well[90].

Figure 4.6 contains plots of the measured carrier concentration (n), mobility (μ), conductivity (σ), and Seebeck coefficient (S) for the three sets of RE-As particles as a function of RE-As concentration. It can be seen that the addition of ScAs nanoparticles to InGaAs produces generally the same electric behavior as adding ErAs nanoparticles despite their differences in lattice parameter and atomic number.

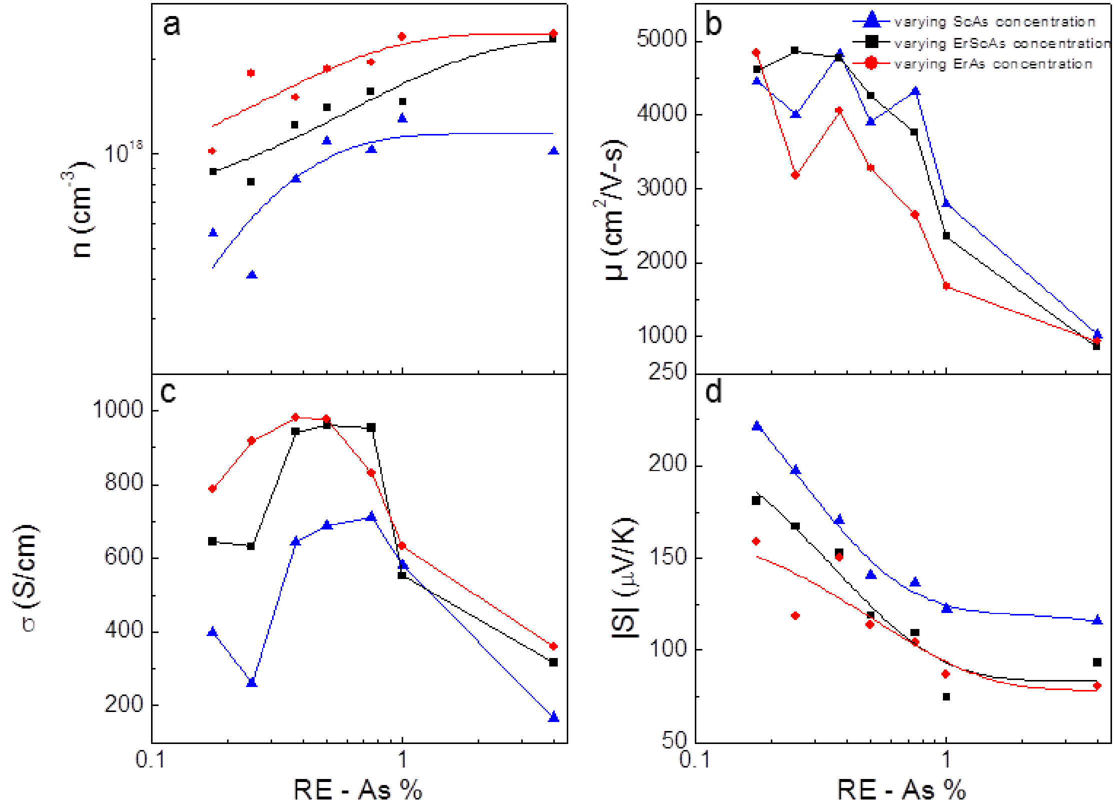

Figure 4.6 Thermoelectric Properties of $Er_xSc_{1-x}As$:InGaAs
Room temperature a) carrier concentration, b) mobility, c) electrical conductivity and d) Seebeck coefficient as a function of rare earth concentration for single crystal nanocomposites. The lines are guides for the eye.

The carrier concentration of the nanocomposites is found to initially increase as more RE is added and then level out for concentrations above ~1%. All the samples produced n-type behavior. ScAs nanoparticles consistently produce fewer carriers for a given concentration than ErAs. Alloying Sc+Er produced carrier concentrations roughly in between those of pure ScAs and pure ErAs. Mobilities of all the films steadily falls as higher RE concentrations are introduced. Conductivity rises initially over the first 0.25% of RE incorporation before peaking around 0.25-

0.75% and then falling off precipitously. The maximum conductivity of the Sc films is found to be about 2/3 the maximum of Er films. The Seebeck coefficient tracks inversely with the measured carrier concentrations with a steady decrease for all three types of RE particles up to 1% before leveling off.

Electrical transport through these nanocomposites are more complicated than the addition of just an electron donor source. The number of particles and their sizes clearly affect this relationship. At a given rare earth concentration, Er doped InGaAs has a lower Seebeck coefficient than Sc doped InGaAs at that same rare earth concentration. As the rare earth concentrations increase to 1%, the carrier concentrations rise and the Seebeck coefficient falls, indicating the maximum enhancement is confined to lower rare earth concentrations.

4.3.1 Doping Mechanism From Rare Earths

Nanoparticles formed from codeposition of Sc+Er are likely alloyed based on the active carriers they produce. If ScAs and ErAs nanoparticles nucleated independently, then the carrier concentration should be roughly the sum of the corresponding concentrations of Er and Sc. However, the carrier concentration appears to be an average of the carriers generated by equivalent amounts of Er and Sc, suggesting the formation of nanoparticles of an intermediate size between ScAs and ErAs.

Much work still needs to be done to understand how rare earth incorporation in InGaAs contributes charge carriers to the matrix. It has been theorized that interstitial atomic impurities are the main source of donors in InGaAs, as it has been seen that

larger lattices have higher doping efficiencies from rare earths[43]. However, this does not explain the difference in doping efficiency of different rare earths, since Sc is the smallest rare earth examined and has the lowest doping efficiency. This is in disagreement with the interstitial argument since smaller atoms should be able to more readily incorporate as interstitials. Furthermore, it is unlikely that substitutional atomic impurities are electrically neutral.

Here we present a hypothesis based on an anticorrelation between lattice mismatch and doping efficiency in rare earths. It is a simplistic model meant to be a base for further experimental verification through schottky barrier height measurements, DLTS, and TEM. It is important to note that Er doped InGaAs has more electrically active carriers for a given rare earth concentration than Sc. This is consistent with the nanoparticle size dependence argument for carrier concentration put forth in Ref. [90].   In general, larger lattice mismatch corresponds to the formation of larger RE-As nanoparticles[91]. For a given atomic incorporation of rare earth above the solubility limit, the larger lattice mismatch forms larger strain nucleated particles. With less total number of particles, there is less interfacial area available for carriers to thermionically excite from the semimetallic particle into the conduction band of the InGaAs semiconductor. Therefore, less lattice mismatch between the particles and InGaAs correlates to higher carrier concentration. A schematic of how electrons can be thermally excited from either atomic impurities or nanoparticles is shown in Figure 4.7

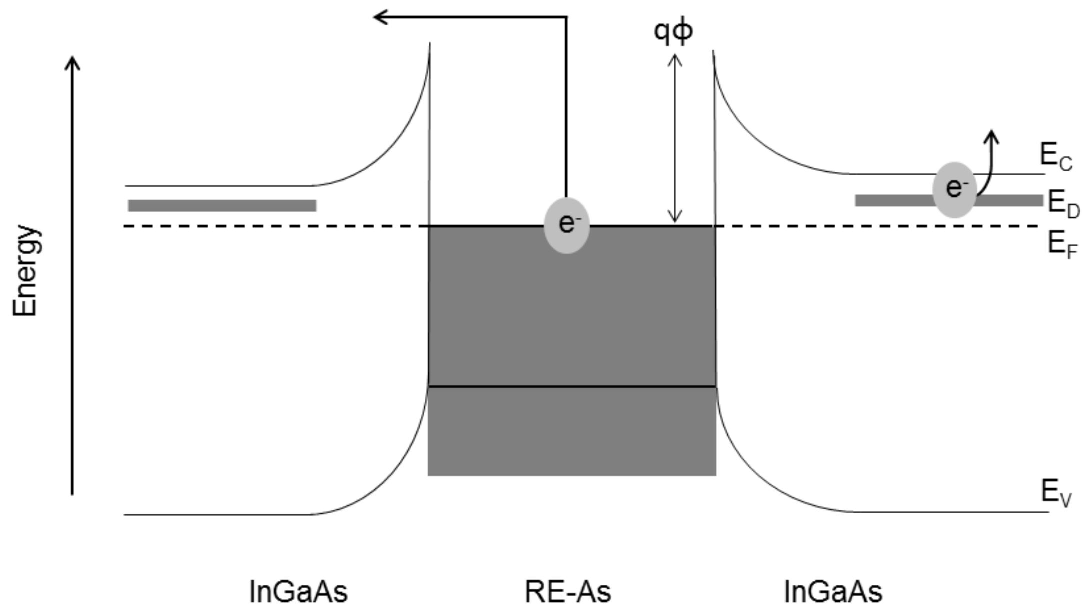

Figure 4.7 Schematic of Doping Mechanism for Rare Earths in InGaAs
Band diagram of the double schottky barrier heterostructure for RE-As nanoparticles embedded in InGaAs. Carriers can be excited into conductions from the metallic nanoparticles as well as from impurity levels from atomic rare earth impurities.

Electrons can be excited into conduction from an impurity band formed by atomic impurities in InGaAs. Electrons can also be excited into conduction from the particles themselves in the double schottky barrier structure as shown above. The barrier height for ErAs on InGaAs has been measured to be ~100meV at room temperature[33]. High temperature Hall measurements on Gd doped InGaAs discussed in Appendix B lead to an activation energy of ~39mev. This is a poor approximation to barrier height as significant thermal excitation from other defect levels in InGaAs can contribute to the extracted activation energy.

4.3.2 Thermal Conductivity of Er and Sc Doped InGaAs

Epitaxial lightly doped InGaAs films lattice matched to InP have a reported thermal conductivity between ~4.8-6.4 W m/K-1 as measured by time-domain thermo reflectance, the 3ω method and thermal diffusivity measurements[92]. The addition of epitaxial RE-As nanoparticles reduces the overall thermal conductivity of InGaAs. Figure 4.8 shows the thermal conductivity of InGaAs films determined from the 3ω method as a function of rare earth concentrations and elements. The 3ω method for measuring thermal conductivity leads to an experimental uncertainty of ±15% in the samples measured. Due to the inherent noise resulting from difficulties in measuring the thermal conductivities of thin films[55, 58], it was desired to find an analytical expression to represent the thermal conductivity of each rare earth compound as a function of rare-earth concentration.

The formation of RE-As nanoparticles occurs in stages. Below the solubility limit, the rare earth elements act as individual impurities. At concentrations slightly above the solubility limit, RE-As nanoparticles start to nucleate[37, 41]. Over a finite concentration range, the size of particles remains constant with increasing concentrations only producing more particles[79]. Once a critical concentration is reached, the particles begin to coalesce and can form new structures like nanorods or sheets[82, 93]. The changing nanoparticle growth regimes and the uncertainty regarding the number of individual rare earth impurity atoms in the lattice make modeling the thermal conductivity challenging and unlikely to elicit more information than an empirical fit.

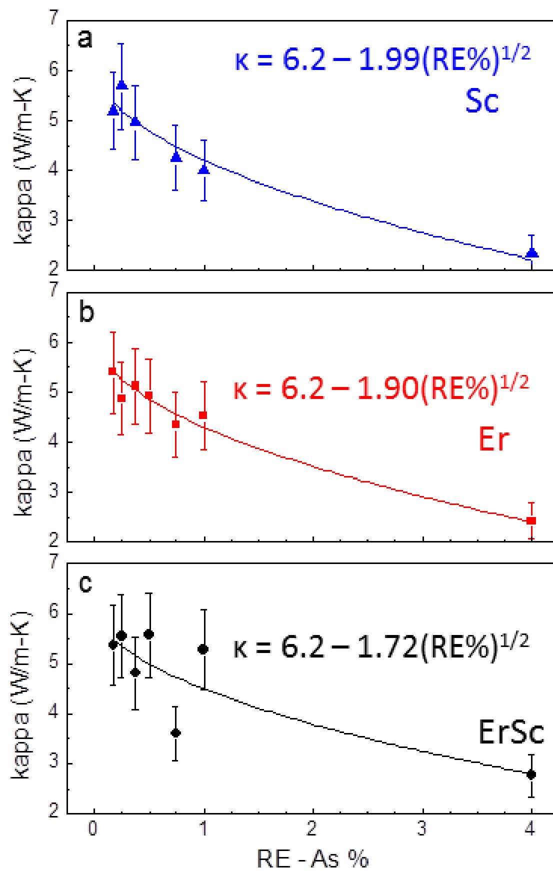

Figure 4.8 Thermal Conductivity of $Er_xSc_{1-x}As$:InGaAs
Room temperature thermal conductivity of a) Sc, b) Er and c) Er+Sc doped InGaAs. The lines are empirical least squares fits to the experimental results.

A simple one-parameter power law was found to provide agreement for the three types of nanoparticles. The thermal conductivities were represented by the expression $6.2 - A \bullet (RE\%)^{1/2}$ in W/m-K. The coefficient A provides a measure of the rate at which the thermal conductivity of InGaAs decreases for each type of nanoparticle. The fits to Sc (A = 1.99) and Er (A = 1.90) correlate well with the data; however, significantly more scatter is found in the Sc+Er (A = 1.72) measurements making for a poorer fit. The empirical fits show that there is no significant difference

in choice of nanoparticle with regards to thermal conductivity. Despite the fact that Er and Sc have very different masses, no direct relationship between these factors and phonon scattering is seen in this system.

The empirical fits to the thermal conductivity provide a means of minimizing the uncertainty of the individual measurements from propagating into the estimates for ZT. The thermal conductivity is expected to follow a monotonically decreasing function over the rare earth concentrations investigated here. Figure 4.9 shows the ZT values for the three nanocomposites as a function of rare earth concentration. All three curves follow the same trend and have maximum room temperature ZT values between 0.11 and 0.13, similar to ZT for the best Si doped InGaAs. In contrast, unintentionally doped 1 μm thick InGaAs films without any rare-earth elements were found to have ZT values around 0.0045.

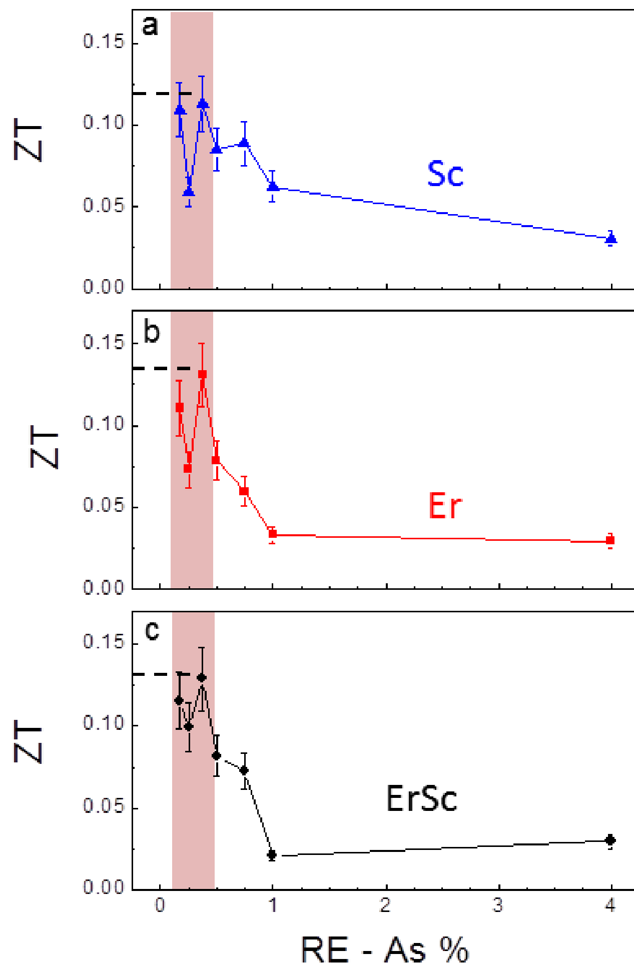

Figure 4.9 ZT of $Er_xSc_{1-x}As$:InGaAs
Room temperature ZT of a) Sc, b) Er and c) Er+Sc doped InGaAs.

The properties of rare earth based nanoparticles composed of crystal structures other than rocksalt, as in the Eu-As system, or nanoparticles that introduce different strain profiles in the InGaAs have the potential to deviate significantly from those reported here. It has also been seen that CeAs particles do not contribute carriers in the same way as Er and Sc[94]. The electrical properties of Sc and Er based

nanocomposites may also begin to depart from each other at higher temperatures that are closer to the optimal thermoelectric temperature of the materials.

Consequent mixing of rare-earth elements to produce nanoparticle alloys do not provide significant enhancement in the thermoelectric figure of merit for InGaAs RE-As nanocomposites at room temperature, but does offer a way to tune doping levels and cluster size. The analysis shows the highest ZT values occur for rare earth concentrations below 0.5% in all three cases and that the lower rare earth doped regimes may hold greater promise for enhancing ZT values in III-V semiconductors.

4.4 Conclusions from Sc and ErSc Doping

This chapter discussed the growth mechanism for embedded RE-As nanoparticles and how that effects the thermoelectric properties at room temperature. Epitaxial nanocomposites composed of ScAs, ErAs, and ScErAs nanoparticles embedded in InGaAs were grown by MBE. The use of an InAlAs buffer layer and thicker active region was shown to reduce the 3D carrier concentration, suggesting higher quality material. The presence of ScAs nanoparticles was confirmed by atom probe tomography and found to be larger than ErAs nanoparticles in InGaAs The main difference electrically between the nanocomposites is that Er incorporation tends to produce more active carriers in InGaAs than Sc. This leads to a higher Seebeck coefficient for Sc based nanocomposites, but also to a lower electrical conductivity. Alloying Er and Sc in individual nanoparticles affects active carriers generated in the material, and they provide a means of tuning the electrical properties

in these thermoelectric nanocomposites. Thermal conductivity measurements show that as rare earth concentration increases, thermal conductivity decreases monotonically; however, no strong dependence is found based on the choice of rare earth particle. The maximum room temperature ZT values were found to be around 0.13 and to occur at rare earth concentrations less than 0.5%.

Chapter 5

5 GdAs Nanoparticles in InGaAs: a Survey of Rare Earths

This chapter presents Gd as a new thermoelectric dopant in InGaAs and compares it to the previously studied rare earths, Er and Sc. Si doped InGaAs is used as a benchmark for the thermoelectric properties in InGaAs as a way to understand how the nanoparticle properties of rare earth doping behaves. Gd is a promising thermoelectric dopant because it has similar atomic structure to the high efficiency dopant, Er, while GdAs is lattice matched to the InGaAs host matrix, allowing us to study how strain affects the thermoelectric properties of this material system. We report the growth of epitaxial GdAs and Gd-doped $In_{0.53}Ga_{0.47}As$ (InGaAs) on InP (001). We show that above the solid solubility limit, Gd incorporates as coherent GdAs nanoparticles when codeposited during molecular beam epitaxy of InGaAs. This behavior is similar to other previously studied rare earth (RE) dopants (e.g. Er, Sc, Tb)[26, 45, 90].

Room temperature electrical measurements show that Gd has a higher electrical activation efficiency in InGaAs than either Er or Sc, making it the most effective n-type RE electronic dopant studied to date. The higher doping efficiency of Gd in InGaAs leads to a larger electrical conductivity, leading Gd to be a more efficient rare earth dopant for thermoelectrics. This trend supports the hypothesis put forth in the previous chapter that lower lattice mismatch between the RE-As compound and

the InGaAs matrix leads to smaller nanoparticles with higher density and more electrically active carriers for a given dopant concentration. Overall, Si is seen to have a higher ZT over a range of carrier concentration, with the exception of the peak ZT for Gd doped InGaAs.

5.1 Growth of GdAs Thin Films

Since GdAs had not been grown by MBE to our knowledge, in order to get an understanding of how GdAs nanoparticles might form during codeposition in InGaAs, the growth of epitaxial GdAs films was first studied. It has been shown that LaAs and does not grow epitaxially on GaAs without special growth procedures and that CeAs does not form nanoparticles when codeposited with InGaAs[14, 95]. ErAs and ScAs epitaxial thin films have been grown successfully on GaAs [76, 77]. Hence, GdAs films were initially grown on GaAs(001). This makes it a ternary (Gd-Ga-As) rather than a quaternary system (Gd-In-Ga-As), reducing the number of potential interfacial phases that might form. Furthermore, the lattice mismatch between GdAs and GaAs allows for separation of their x-ray diffraction peaks.

A modified VG V80H solid source MBE system was used to grow GaAs buffer layers on GaAs (001) substrates, with an As_4 overpressure. A conventional effusion cell was used for Ga, a valved cracker for As and a high temperature effusion cell for Gd. For each sample, the wafer's native oxide was desorbed at 580°C under an As overpressure. The oxide desorption process was also used to calibrate a pyrometer from which subsequent temperatures during growth were adjusted. Reflection High Energy Electron Diffraction (RHEED) was used to determine when the oxide had

desorbed as shown upon the appearance of a diffraction pattern on the [010] direction. A GaAs buffer layer was grown at 580°C to obtain a smooth, atomically clean surface for GdAs growth. Growth temperature was varied from 250°C to 550°C in order to find the growth window for single crystal epitaxial GdAs. The Gd cell flux was calibrated by Rutherford backscattering measurements on Si substrates.

While ErAs and ScAs thin films have previously been shown to grow epitaxially on GaAs (001) at 350°C [76, 77], attempts to grow GdAs at this temperature resulted in both (001) and (111) oriented domains as shown in Figure 5.1 by the spotty rings in RHEED and x-ray diffraction. Since the ring diffraction pattern is indicative of polycrystalline growth, RHEED images lose their directionality when looking at different directions on the sample. The growth of (111) orientated GdAs is possibly a way to create lower energy interfaces at low temperature on GaAs. GaAs (001) is a polar surface with alternating layers of Ga and As, but GdAs (001) is a non-polar surface. GdAs (111), however, is a polar surface, so can easily be grown epitaxially on GaAs(001) and can also provide a better template for GaAs overgrowth[27]. As the growth temperature is increased, the RHEED spots become brighter and there are also sharper x-ray peaks. The ratio of the intensity of (001)/(111) peaks increases with temperature until a growth temperature of 550°C, where single crystal GdAs(001) epitaxial thin films were grown, as verified by RHEED and later x-ray diffraction.

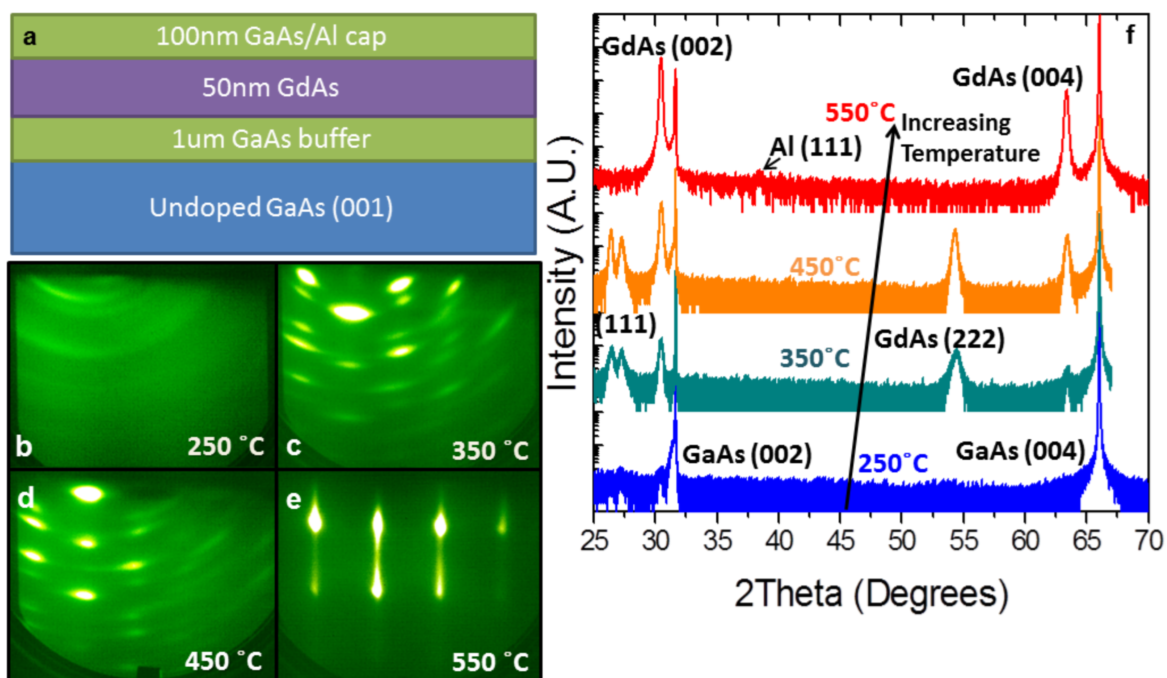

Figure 5.1 GdAs Temperature Series
a) the growth stack used to determine GdAs growth conditions. RHEED patterns along the [010] direction after GdAs deposition changing growth temperature from 250-550˚C (b-e), and (f) Corresponding X-ray diffraction patterns for each growth temperature: the blue scan is 250˚C, teal is 350˚C, orange is 450˚C and red is 550˚C single crystal GdAs growth.

The GdAs films showed the same (1x1) surface reconstruction as both ErAs and ScAs thin films as shown in Figure 5.2 (a-c), suggesting that the compounds have similar structure. The extra spots seen in RHEED in the [110] direction in Figure 5.2c were initially thought to be a result of strain from the lattice mismatch with GaAs. However, 5nm GdAs on InGaAs grown at typical InGaAs growth temperatures of 490°C show that these spots persist (Figure 5.2d). When the sample is annealed in a low As environment or grown with a low As overpressure, the extra spots disappear as shown in Figure 5.2 e-f. The RHEED pattern in the [0-11] direction remained unchanged while tuning these low As conditions, suggesting that

the extra spots seen in the [011] direction are induced by excess arsenic decorating the surface in the fast diffusion direction, [0-11]. It is important to note that GdAs films grown on InGaAs at a typical InGaAs growth temperature of 490°C showed (001) single crystal growth.

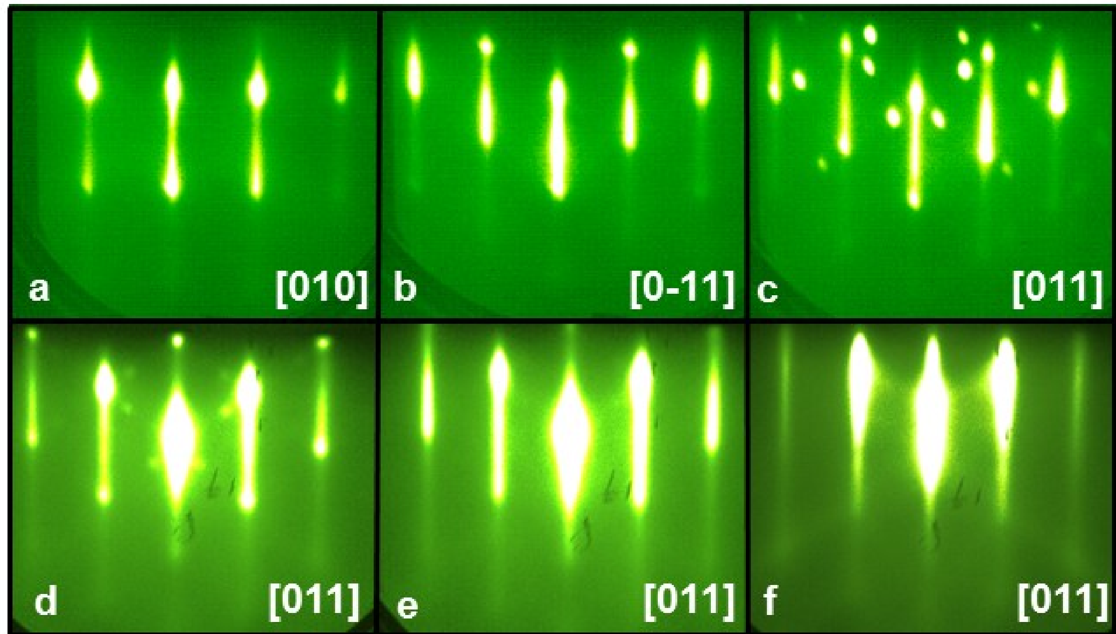

Figure 5.2 GdAs Single Crystal
a-c) show the 1x1 surface reconstruction of GdAs on GaAs in RHEED. d-f) shows RHEED spots persisting of GdAs grown on InGaAs with a high As overpressure that can be annealed away in a low As environment in (e) or grown without As accumulation in a low As overpressure in (f).

5.2 TEM of GdAs Nanoparticles in InGaAs

Having confirmed single crystal GdAs growth conditions on GaAs and InGaAs, codeposition was used to grow InGaAs thermoelectric films doped with Gd. Confirmation that GdAs nanoparticles form in the InGaAs matrix was made using

high resolution transmission electron microscopy (HRTEM). The TEM sample prep and imaging was done by Ryan Need and Stephan Kraemer. This technique uses z-contrast to identify regions of excess Gd. Since Gd has a large atomic number, it scatters electrons much more than the underlying InGaAs matrix. When looking at high resolution TEM, the beam's intensity is measured on axis. Since regions of GdAs have much higher Z, it results in more scattering and a dimmer image than the lower z of Ga or In atoms. A cross-sectional TEM lamella was prepared using focused ion beam (FIB) milling. The high-resolution image, displayed in Figure 5.3, confirms the presence of GdAs nanoparticles at 1.2% GdAs concentration with average particle diameter of 1-2 nm. There are no nanoparticles present in the InAlAs buffer layer, confirming sharp interfaces and low diffusion of Gd atoms once they have embedded in InGaAs due to the very stable GdAs bond. The inset shows the coherent GdAs/InGaAs interface due to the underlying As sublattice.

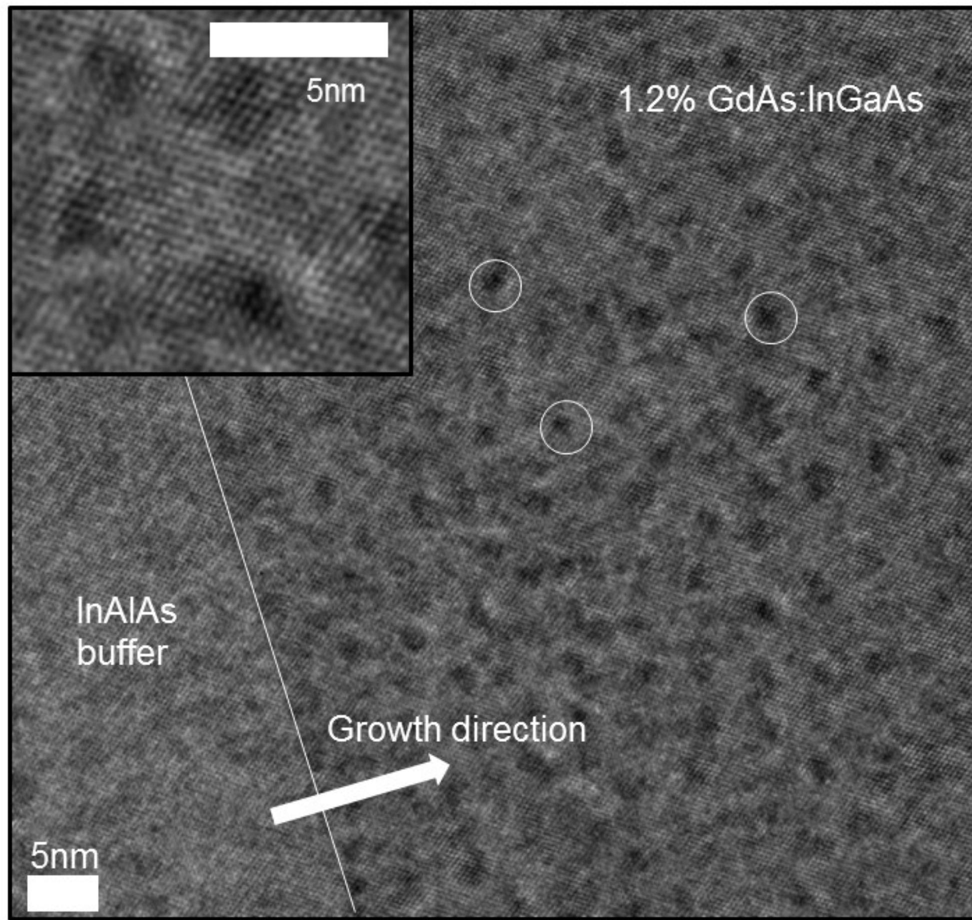

Figure 5.3 GdAs Nanoparticles in TEM
GdAs nanoparticles embedded in an InGaAs matrix. The presence of nanoparticles is confined to the active region as the InAlAs buffer shows no signs of particles. The inset shows coherent interfaces across the nanoparticle/semiconductor interface.

5.3 Room Temperature Thermoelectric Properties of Embedded GdAs Particles in InGaAs

Once GdAs nanoparticle formation was confirmed, the thermoelectric properties of films with varying concentrations of Gd was studied. InAlAs and InGaAs layers were grown on InP (001) substrates, with an As_4 overpressure. Conventional effusion

cells were used for Ga, In, and Al, a valved cracker for As and a high temperature effusion cell for Gd. For InP heteroepitaxy, during oxide desorption, a thin layer of InAs may form from As-P exchange reactions that can act as a parallel conduction path [64, 65]. A 200nm thick InAlAs buffer layer was grown at 490°C over this interfacial layer with the intent of minimizing parallel conduction in the InAs during electrical transport measurements by acting as a back barrier and also for obtaining a smooth, atomically clean surface for InGaAs growth. Next, InGaAs active layers were grown 4µm thick at 490°C at a rate of 1 µm/h to further reduce the contribution from the InAs interfacial layer. Thick films also ensured that low conductivity films were not completely depleted. The substrate heater power was reduced for Gd doped InGaAs growth because the large heat flux from the high temperature Gd cell causes the substrate temperature to increase by about 30°C. Gd was incorporated in the InGaAs layer by codeposition. Rare earth doping concentrations were chosen to examine the thermoelectric properties of doping below and above the estimated solid solubility limit and to maximize power factor and ZT.

Room temperature Hall measurements were done on square samples with In dots as ohmic contacts to the film. Room temperature Seebeck coefficients were measured using differential heating between two commercial Peltier elements and calculated using the slope method as described in Section 2.3 [48]. Room temperature thermal conductivity measurements were done by Joe Feser at UIUC using time domain thermoreflectance (TDTR) at 1.1 MHz modulation frequency to

ensure penetration depth longer than the average mean-free-path of phonons in the material[55]. More details about TDTR can be found in section 2.4.2.

Figure 5.4 shows the electrical transport properties of doping InGaAs with Gd. Consistent with both Sc and Er doping, below the estimated solubility limit (~0.1% GdAs concentration)[42], the electrically active carrier concentration of Gd doped InGaAs increases rapidly compared to unintentionally doped InGaAs. Above the estimated solid solubility limit, the carrier concentration starts to plateau due to the different mechanism for carrier activation from GdAs particles. Hall measurements show that the carrier mobility decreases above this solubility limit as the GdAs particle density increases, resulting in a peak electrical conductivity at about 0.5% GdAs concentration. Seebeck measurements show a strong inverse relationship with carrier concentration, consistent with band transport through InGaAs.

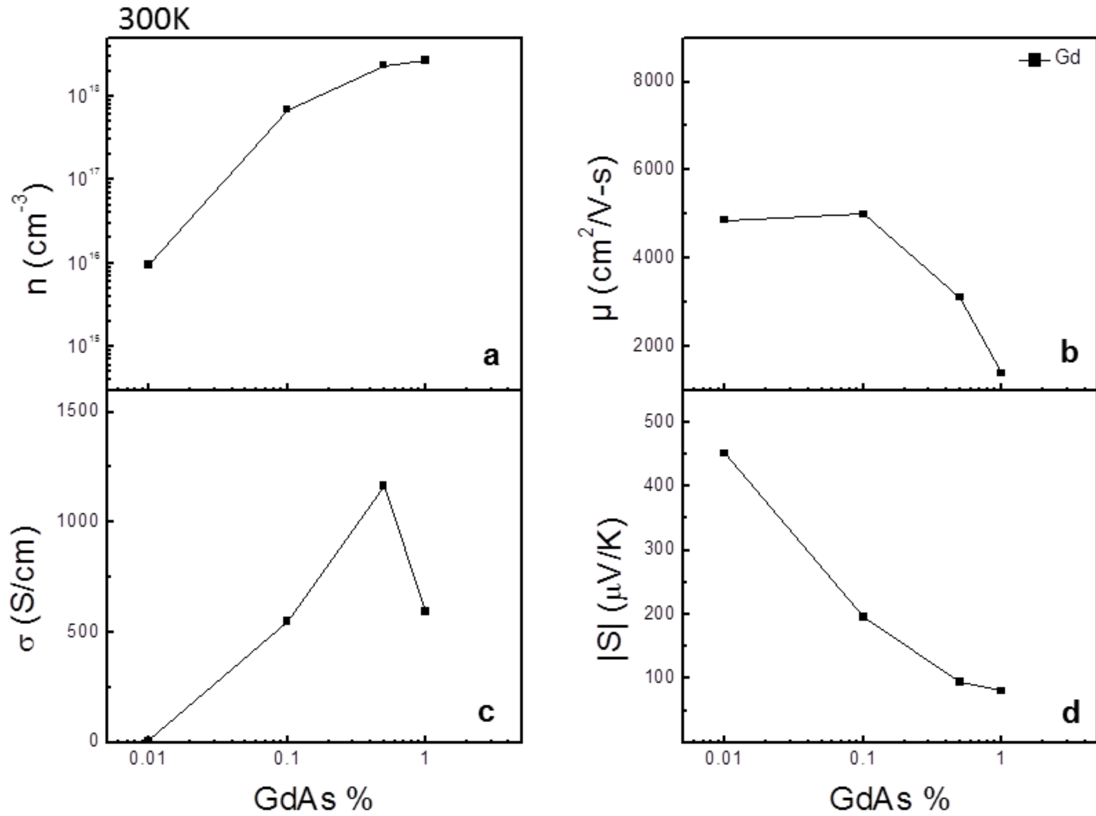

Figure 5.4 Electrical Properties of Gd doped InGaAs

a) Carrier concentration, b) mobility, c) electrical conductivity and d) Seebeck coefficient of Gd doped InGaAs.

The combination of peak electrical conductivity at 0.5% GdAs concentration with the decreasing Seebeck coefficient with Gd incorporation leads to a peak power factor at 0.1% GdAs concentration as shown in Figure 5.5, at the expected onset of nanoparticles[42]. Thermal conductivity results show that as more Gd is incorporated into the film, the thermal conductivity decreases. Particularly above the solubility limit, where the density of nanoparticles increases. It is important to note that the

decrease in thermal conductivity below 0.5% GdAs incorporation is within the error bars of the measurement.

Overall, the peak ZT at room temperature occurs at 0.1% GdAs concentration, consistent with the peak power factor. Although incorporating Gd increases the electrically active carriers while decreasing the thermal conductivity, the largest increase in power factor (therefore ZT) occurs before Gd incorporation helps by reducing thermal conductivity. As GdAs nanoparticles form, electrically active carriers are exchanged for a decrease in thermal conductivity. However, this new transport regime where the thermoelectric properties are improved by thermal conductivity reduction cannot compensate for the decrease in power factor at room temperature. Therefore, efforts to improve thermoelectric efficiency should be directed at improving electrical transport.

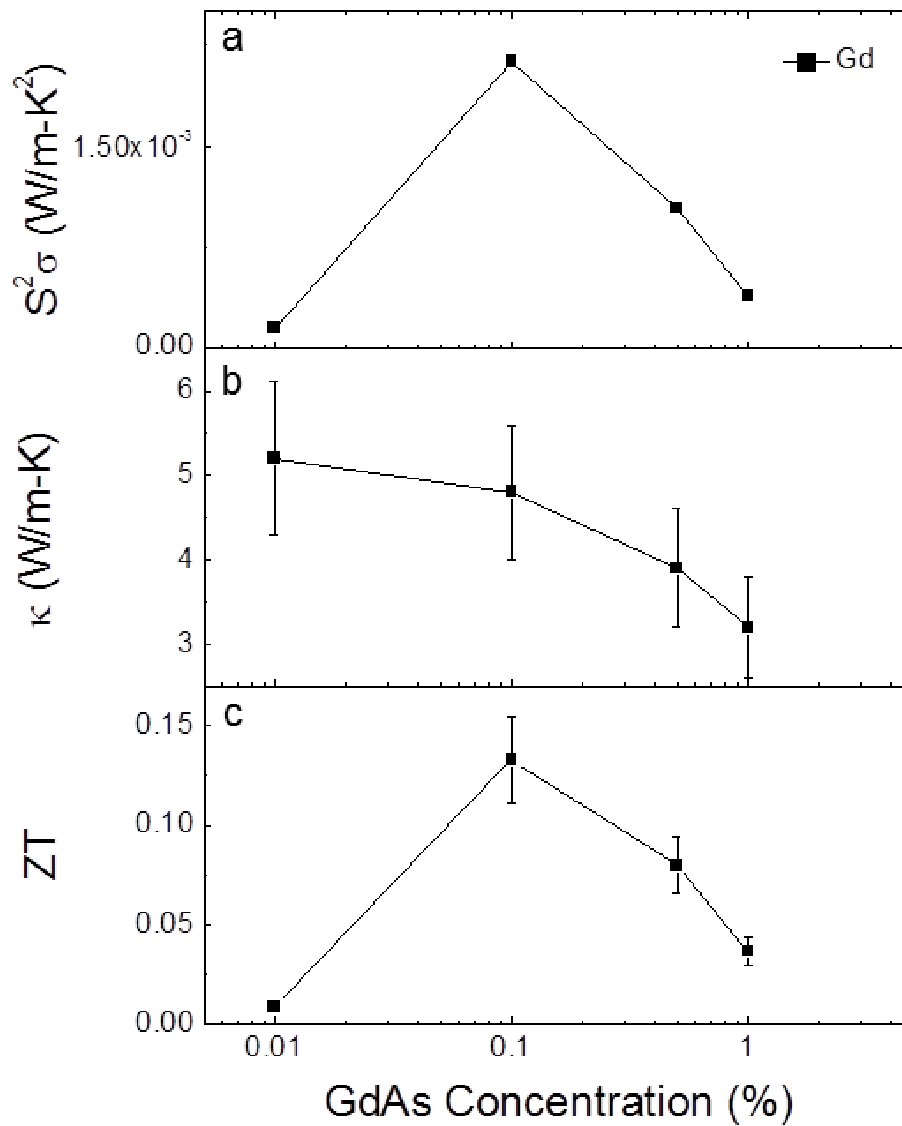

Figure 5.5 Thermoelectric Properties of Gd doped InGaAs

a) Power factor, b) thermal conductivity, and c) ZT of Gd doped InGaAs at room temperature.

5.4 Comparison of Doping with Si to Different Rare Earths at Room Temperature

In order to understand the mechanism of charge and phonon transport in these nanocomposites, doping InGaAs with Gd was compared with doping of Er and Sc. These samples were grown under the same growth conditions as the Gd doped samples as described in section 5.3. InGaAs layers 4µm thick were codeposited with Er, Sc or Gd over 200nm InAlAs buffer layers on InP (001) substrates. The rare earth fluxes were calibrated with RBS measurements and the InGaAs flux was calibrated with RHEED oscillations and X-ray diffraction. For consistency, the same rare earth concentrations were used for all three rare earths.

5.4.1 Doping Mechanism of Rare Earths in InGaAs

Room temperature Hall measurements show that each rare earth exhibits the same trends in electrical transport. As seen in Figure 5.6, the carrier concentration increases sharply below the estimated solid solubility limit and plateaus after nanoparticles start to form. The low doping efficiency of rare earths as compared to Si doped InGaAs is shown in Figure 5.7. To confirm the presence of nanoparticles, low temperature photoluminescence has been performed with limited success as discussed in Appendix C. The sharp increase in carrier concentration below the estimated solubility limit suggests that atomic impurities contribute carriers to the InGaAs matrix, but the nature of contribution of carriers is still poorly understood. At 0.01% RE-As incorporation, there are $2x10^{18}$ cm^{-3} rare earth atoms. However,

there are only ~10^{16} cm^{-3} electrically active carriers, leading to doping efficiencies of less than 1%. It has been suggested that below the solubility limit, Er sitting on interstitial sites in a III-As matrix contributes electrons, while Er sitting substitutionally on a group III site is electrically neutral[43]. However, since rare earths do not have p orbitals in their valence shell to contribute to bonding (they have 1 d electron), it is impossible for rare earths to have sp^3 bonds with As, which is how bonding with group III elements occurs. This different bonding should contribute states to InGaAs instead of being electrically neutral, although it is unknown exactly how. It is possible that these states can act as deep levels in InGaAs, contributing to a doping efficiency less than unity that is seen. In order to study the levels contributed from rare earth dopants, techniques such as Deep Level Transient Spectroscopy (DLTS) would be useful.

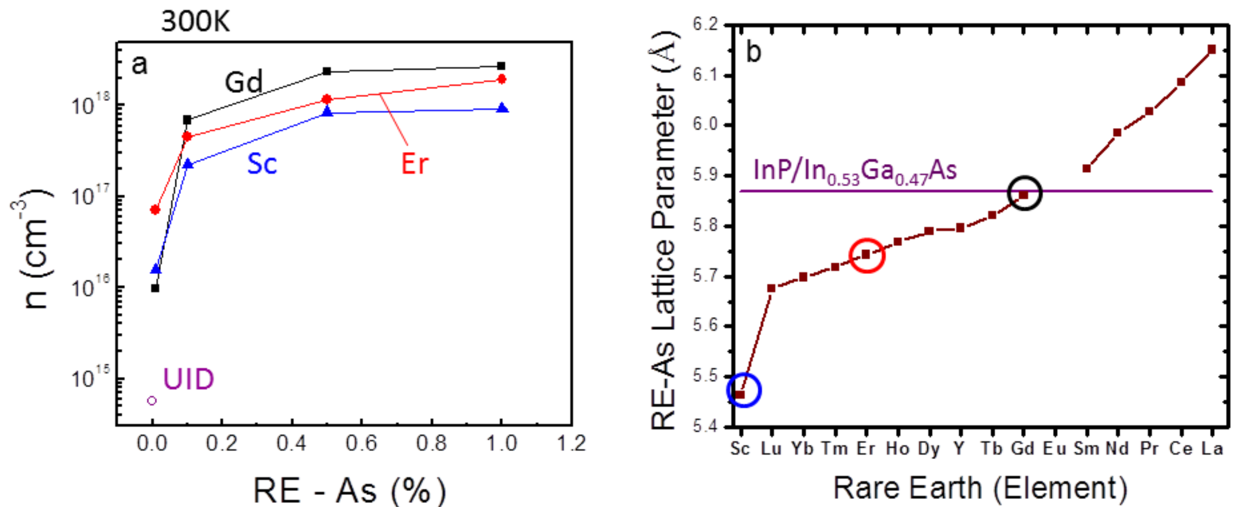

Figure 5.6 Doping Efficiency of Different Rare Earths

a) Electrically active carrier concentration at room temperature for Gd, Er, and Sc doping InGaAs. b) lattice mismatch of the three RE-As correlates with doping efficiency.

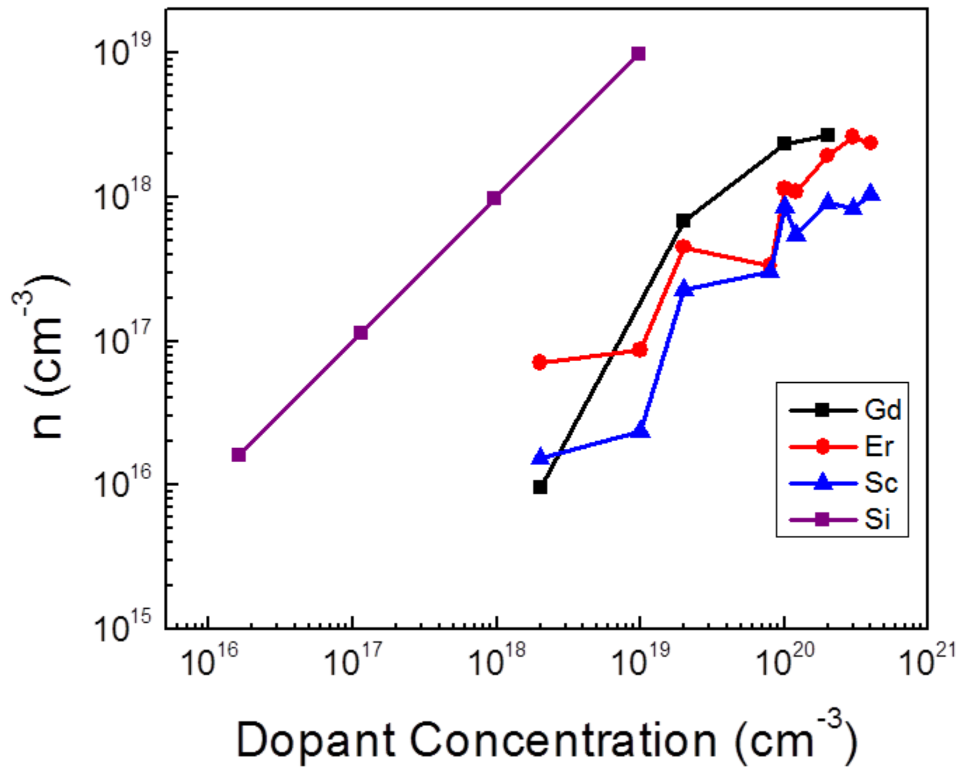

Figure 5.7 Doping Efficiency of Rare Earths and Si in InGaAs
The doping efficiency of Si doped InGaAs is much higher than any of the rare earths. It can be seen that overall, Gd is a more efficient dopant and Sc is a less efficient dopant in InGaAs at a given rare earth concentration.

In Figure 5.6, it is seen that although doping with different rare earths have the same trends with increasing rare earth concentration, each rare earth has a different doping efficiency. Gd doping contributes the most electrically active carriers of the rare earths studied while Sc doping contributes the least. It is important to note that this trend in doping efficiency correlates inversely to lattice mismatch of the RE-As with InGaAs.

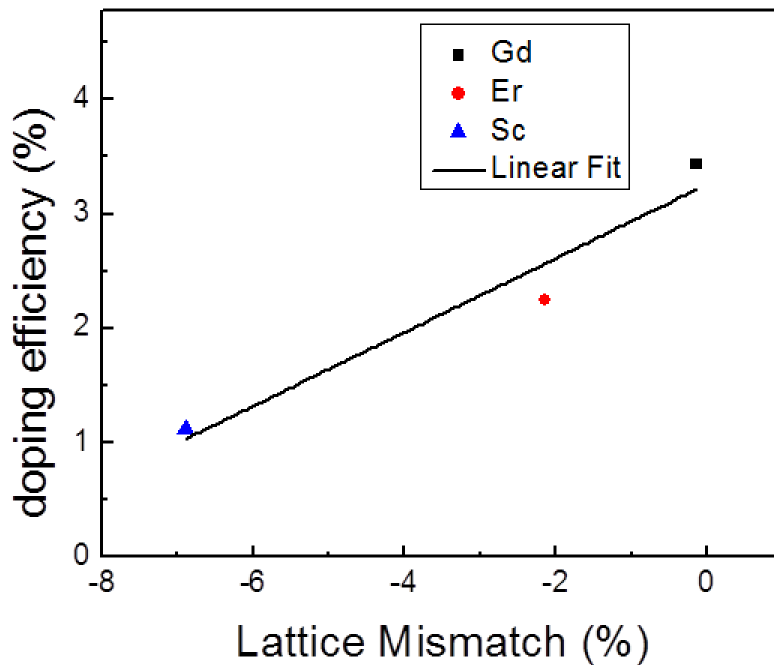

Figure 5.8 Lattice Mismatch Correlates with Doping Efficiency
Peak doping efficiency of each rare earth (at 0.1% RE-As concentration) as a function of lattice mismatch.

ScAs has the most lattice mismatch and the least electrically active carriers, while GdAs is nominally lattice matched and contributes the most electrically active carriers. This lattice mismatch trend is consistent with the strain nucleated particle argument put forth in Section 4.3.1.

5.4.2 Transport in Rare Earth Doped InGaAs

In order to look for resonant dopant features theorized to improve thermoelectric transport in semiconductors[19], tracking how the Seebeck coefficient changes as a function of carrier concentration illuminates how band transport occurs in these InGaAs composites. This section compares rare earth doped InGaAs to Si doped

InGaAs. Rare earths incorporate in InGaAs in a number of different ways, as atomic impurities on interstitial or substitutional sites, or as particles. It is not clear how exactly these different impurities affect transport. It is likely that different impurity bands are formed in InGaAs from these rare earths, but it is unclear how this affects the overall properties of InGaAs. Si provides a good basis for comparison since it is well understood how Si incorporates in InGaAs and contributes carriers through minimal lattice distortion. Plotting the Seebeck coefficient versus carrier concentration can serve as a qualitative comparison to identify if transport occurs primarily through InGaAs or if nanoparticle incorporation leads to new transport phenomena.

Si doped InGaAs provides a base material system to compare with other doping mechanisms. It is seen that Si doping can span a wide range of carrier concentration. It is important to note that all of the rare earth data follows the same InGaAs trends. The main difference is that Gd cannot reach as high of carrier concentrations as Si doping, where Er cannot reach as high of carrier concentrations as Gd, and Sc even less. The fact that all three rare earths follow the same transport trend as Si doped InGaAs indicates that even when these semimetallic nanoparticles are embedded in InGaAs, conduction occurs primarily through the semiconducting matrix.

It is important to note that previously published theory for Seebeck coefficient of InGaAs generated by Ashok Ramu using the model developed in reference [96] lies slightly below experimental values for Si doped InGaAs. This model solves the Boltzmann transport equation without recourse to the Relaxation Time

Approximation for improved accuracy. It takes into account multiple scattering mechanisms; including alloy, polar optical phonon, acoustic phonon, and ionoized impurity scattering. Calculating the contributions from these different scattering mechanisms requires material specific information about the doping profile in the material (donor and acceptor levels), dielectric constant, lattice parameter, effective mass, bandgap, mass density, and speed of sound. Overall, this is too simple to include all scattering mechanisms and experimental data provides a more accurate comparison. If these rare earths acted as a resonant dopant, the data points would lie above the line for Si doped InGaAs or increase Seebeck coefficient with increasing carrier concentration. The comparison of rare earth dopants to traditional (Si) dopants shows no enhancement in thermoelectric properties by incorporating RE-As nanoparticles.

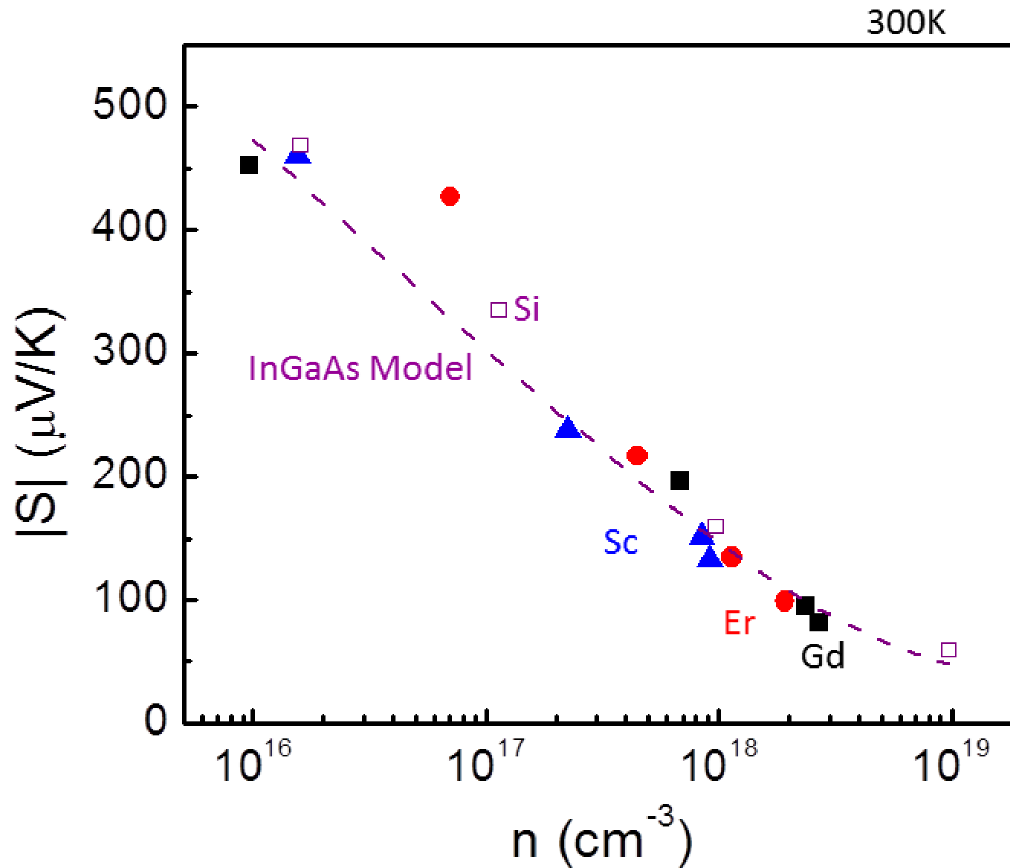

Figure 5.9 InGaAs Electrical Transport
Seebeck coefficient versus carrier concentration in InGaAs at 300K for InGaAs doped with Si, Sc, Er, and Gd. The dashed line is a model for InGaAs plotted as a comparison[96].

5.4.3 Scattering from Rare Earths

The Seebeck coefficient is largely insensitive to scattering as seen from the same Seebeck versus carrier concentration trends independent of dopant type. Mobility gives further information about crystal quality and scattering mechanisms. Figure 5.10 highlights how different dopants affect the crystal quality and transport mechanisms in different ways. Si doped InGaAs provides a baseline as the addition

of more impurities steadily decreases the mobility as to be expected. The lowest Si concentration maintains a very high mobility on par with unintentionally doped InGaAs.

On the other hand, rare earth dopants have more complicated trends in mobility given that they incorporate in InGaAs in several different ways: substitutionally, interstitially, or as particles. It can be seen that even at the lowest rare earth concentration, where particles have not yet formed, the mobility is reduced to two thirds to one half of Si doped InGaAs. However, the mobility does not continue to decrease with carrier concentration at the same rate of Si doped InGaAs, but plateaus or even increases in the case of Er as more rare earth impurity is added. After 0.1% RE-As concentration, where RE-As nanoparticle density increases, the mobility decreases much faster than Si doped InGaAs due to the contribution of semimetallic nanoparticles, which intrinsically have lower mobilities than the semiconducting InGaAs matrix.

The intersection between the regimes of slowly decreasing mobility and quickly decreasing mobility occurs at the estimated onset of nanoparticle formation. This is also the point where the mobilities of RE doped InGaAs are closest to Si doped InGaAs. Although there was no difference seen in Seebeck coefficient between the different rare earths and Si, there is a clear difference between the mobility. Rare earth doping has lower mobilities overall than Si doped InGaAs. This makes sense considering that rare earth doping is much less efficient than Si doping. Overall the fact that the Seebeck coefficient depends on carrier concentration in a very similar

way for both rare earth and Si dopants while mobility does not, shows that mobility trends are much more sensitive to scattering than Seebeck coefficient trends.

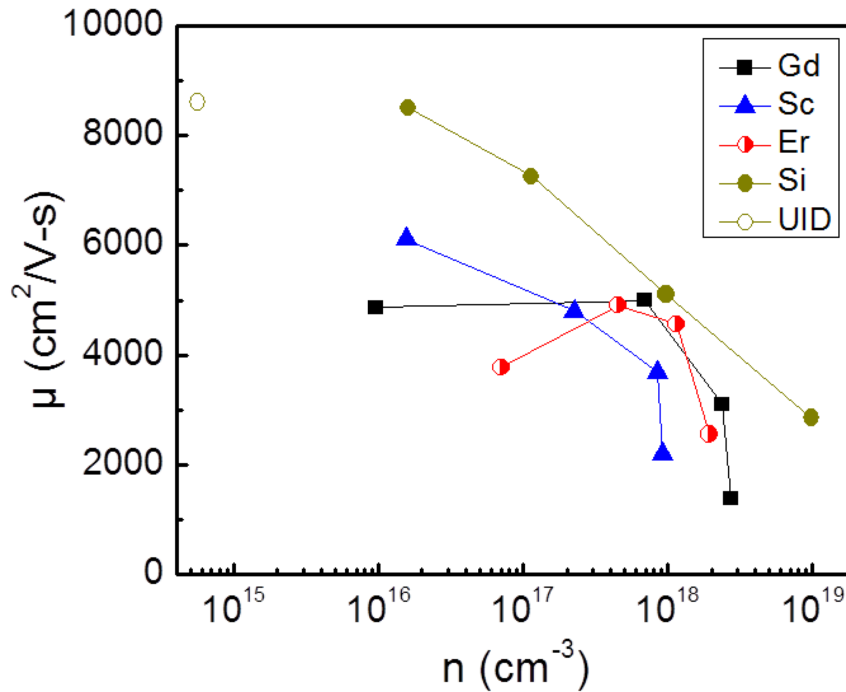

Figure 5.10 Mobility of Doped InGaAs
The mobility of Er, Sc, Gd and Si doped InGaAs as a function of electrically active carrier concentration compared to unintentionally doped InGaAs. The rare earth concentrations are the same as in Figure 5.6.

5.4.4 Reducing Thermal Conductivity in RE Doped InGaAs

In general, a key component to improving ZT has been to maintain a low thermal conductivity. Many of the recent improvements in high ZT materials have come from reducing thermal conductivity by introducing disorder into the material at different lengthscales[5, 13, 97, 98]. By alloying InAs and GaAs in a roughly 50/50 mixture, the thermal conductivity is reduced by an order of magnitude from a value of 55

W/m-K for GaAs to between 4-6 W/m-K for $In_{0.53}Ga_{.47}As$. Using TDTR to measure the thermal conductivity, we can compare how different dopants affect the thermal conductivity of the film. Specifically if atomic mass plays a significant role in scattering phonons.

Figure 5.13a shows that below 10^{18} cm^{-3} carriers, the thermal conductivity remains relatively constant since there are not enough impurities or nanostructuring to significantly distort the periodicity of the lattice for phonon propagation. This is in contrast to previous thermal conductivity measurements claiming a reduction in thermal conductivity from the presence of dilute nanoparticles[26, 98]. It has been shown that the error in the thermal conductivity measurements is larger than originally thought, so that no statistically significant difference in thermal conductivity is realized at RE-As concentrations below 0.5%. As the electrically active carrier concentration increases above 10^{18} cm^{-3}, the thermal conductivity of Si doped InGaAs increases with carrier concentration due to the Wiedemann-Franz law, which states that the electronic component to thermal conductivity is directly proportional to the electrical conductivity.

This can be verified by calculating the electronic thermal conductivity $\kappa_{elec}=\sigma LT$, where T is the temperature in Kelvin, σ is the electrical conductivity and L is a constant, $L=1/3*(\pi k_b/e)^2$. Below 10^{18} cm^{-3} carriers, κ_{elec} is less than 1 W/m-K; insignificant compared to the lattice contribution to thermal conductivity (κ_{ph}). Above 10^{18} cm^{-3} carriers, κ_{elec} starts to increase quickly and has a value of more than 3 W/m-K at 10^{19} cm^{-3} Si concentration. The effect of the Wiedemann-Franz law is

seen as the thermal conductivity of Si doped InGaAs increases at 10^{19} cm^{-3}, although not by as much as κ_{elec} would indicate. This is likely due the a combination of a compensating decrease in κ_{ph} from added impurities and the fact that TDTR tends to underestimate the thermal conductivity in InGaAs because it does not measure the long wavelength phonon contribution to thermal conductivity when operating at high frequency[92]. This issue has not been as severe in rare earth doped InGaAs due to the increased scattering of mid to long wavelength phonons[55].

While the thermal conductivity of Si doped InGaAs increases with carrier concentration, the rare earth doped InGaAs decreases in thermal conductivity. The increased density of RE-As nanoparticles effectively scatters phonons. In this way, rare earth doping overcomes the Wiedemann-Franz law where the total thermal conductivity decreases due to increased phonon scattering which overcompensates for the increase in κ_{elec}. This improves upon traditionally Si doped InGaAs in that rare earths effectively decouple the electrical and thermal conductivities. ZT can be improved by increasing the electrical conductivity while decreasing the thermal conductivity.

5.4.4.1 Thermal Conductivity Comparison

Most recent improvements in thermoelectric efficiency has come from reduction in the thermal conductivity of materials[99–101]. It is important to note that thermal conductivity measurements are the largest source of error in accurately measuring ZT. Particularly in thin films, where small temperature gradients must be measured by techniques that have low signal to noise ratios such as TDTR[60] and 3ω[52].

This leads to precision of approximately 20% on thin film measurements. However, different measurement techniques have much larger error, with thermal conductivity of bulk and thin film InGaAs ranging from 4.7-6.4 W/m-K[61, 92, 102]. The large error associated with thermal conductivity measurements lead to poor quantitative comparisons over different measurement setups and techniques. Instead, qualitative comparisons within the precision of the measurement setup can be made.

The difference between measurement techniques has been studied in the past[55]. Since the 3ω technique uses lower frequencies, the thermal penetration depth is larger than the film thickness and a frequency independent temperature difference across the film is measured. Interface thermal resistance is neglected in this measurement. This implies that the measured temperature difference is proportional to a larger, more comprehensive range of phonon frequencies. The main sources of error in the 3ω technique are from accurate measurement of film thickness and thermal resistance at interfaces.

TDTR uses a high frequency technique to measure thermal conductivity, leading to smaller thermal penetration depths. In this setup, the thermal resistance of the bottom interface of the film does not contribute to the measurement. However, this technique tends to underestimate thermal conductivity due to the high frequency regime that it captures. Figure 5.11a shows that as the modulation frequency of the measurement is decreased, the measured thermal conductivity value increases due to capturing a wider range of phonon frequencies with a larger thermal penetration depth.

This is particularly prominent in InGaAs, where there is a strong frequency dependence on thermal conductivity. Figure 5.11b shows that as the thermal penetration depth increases (modulation frequency decreases), the measured thermal conductivity increases. This is due to the fact that as the frequency decreases and the thermal penetration depth increases, the measurement begins to capture thermal conductivity from longer wavelength phonons. It can be seen that as more Er is incorporated into the material, the frequency dependence diminishes due to the fact that ErAs particles effectively scatter mid to long wavelength phonons. However, at 0.3% ErAs, the doping range where optimal thermoelectric performance is seen, there is still a strong frequency dependence since the particle concentration is not high enough to have a large effect on phonon scattering. Using larger thermal penetration depths reduces error by including more phonon frequencies, but has larger error associated with setting the phase for low modulation frequencies[55].

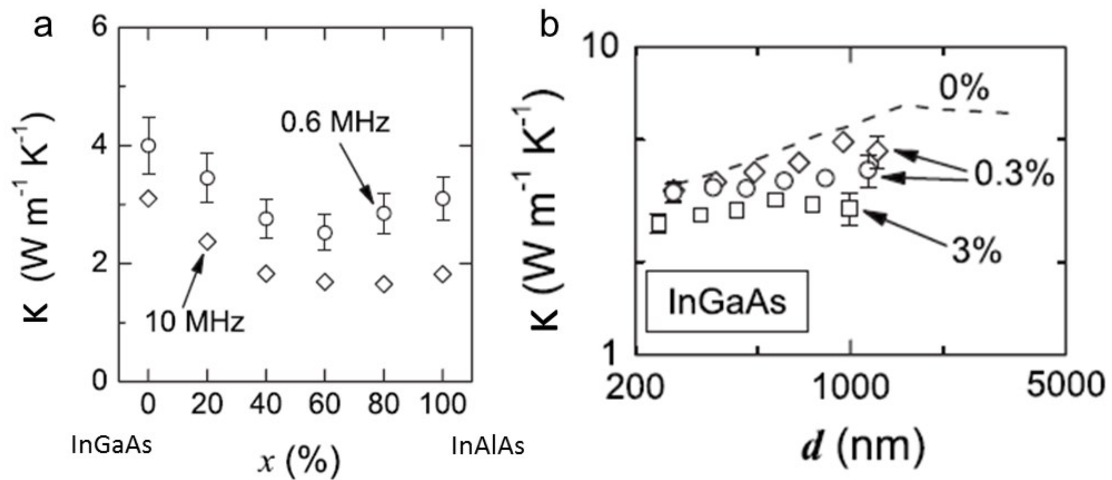

Figure 5.11 Error in TDTR Measurements[55]
a) The difference in thermal conductivity measurements using higher modulation frequencies in InGaAlAs as the InAlAs composition (x) is increased. b) The measured thermal conductivity of InGaAs with varying concentrations of ErAs as a function of thermal penetration depth (modulation frequency) for 2μm thick films.

A comparison of thermal conductivity for rare earth doped InGaAs in this work based on the 3ω technique and TDTR technique is shown in Figure 5.12. It can be seen that the thermal conductivity techniques agree within the ~20% error of these measurements. Overall, the thermal conductivity measurements from the 3ω technique result in slightly higher measured thermal conductivity values due to the larger thermal penetration depth used in this measurement technique.

Lastly, the 1% Gd doped InGaAs sample likely has a lower thermal conductivity than its Er and Sc counterparts due to the slower growth rate of InGaAs used in order to incorporate higher concentrations of Gd. Slower growth rates give rare earths more time to move on the InGaAs surface and incorporate into RE-As nanoparticles,

likely increasing the density and/or the size distribution of particles that can more effectively scatter phonons.

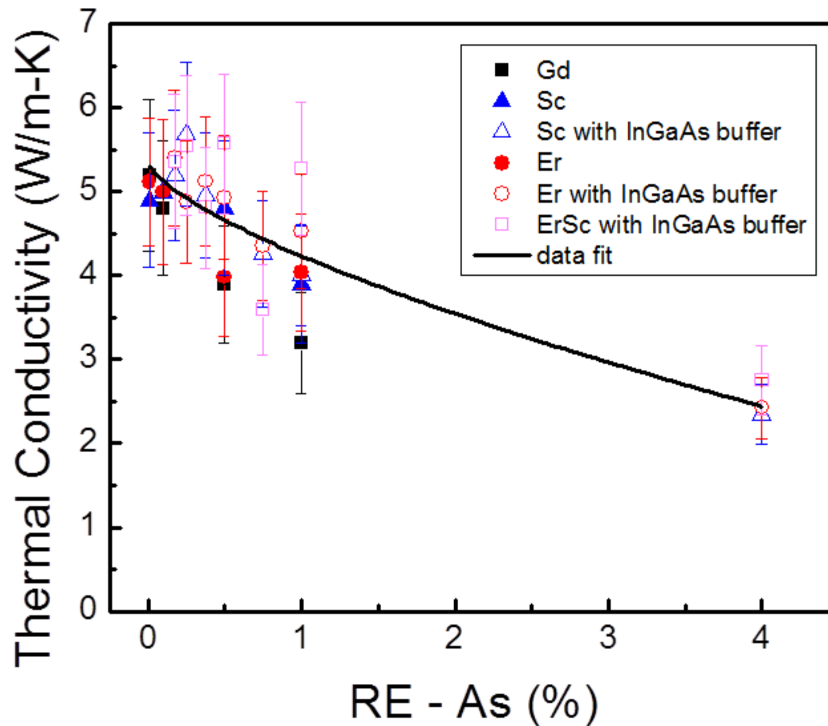

Figure 5.12 Comparison of thermal conductivity measurements
Thermal conductivity of all rare earth dopants follow the same trend within experimental error. Open circles are 1 µm thick InGaAs with an InGaAs buffer layer and a growth rate of 0.5µm/hr measured by the 3ω method and the closed circles are 4 µm thick InGaAs with an InAlAs buffer layer and a growth rate of 1µm/hr measured by TDTR with a modulation frequency of 1.1 MHz.

5.4.5 Thermoelectric Properties of RE Doped InGaAs

Figure 5.13b highlights the electrical contribution to ZT, the power factor ($S^2\sigma$). It is seen for all rare earth dopants and for Si doping that the power factor peaks around 10^{18} cm^{-3} carriers. This is consistent with the rare earth concentration (0.1% RE-As) where the expected onset of nanoparticles occur in Gd and Er doped

material. The low doping efficiency of Sc doped InGaAs requires higher Sc incorporation to maximize power factor. These trends are also consistent with achieving mobilities from rare earth doping as close to Si doped InGaAs as possible. Overall, the higher the doping efficiency of the rare earth, the higher the power factor is. In general, Si doped InGaAs has the highest power factor over a range of carrier concentrations due to the higher mobilities and doping efficiencies. However, 0.1% GdAs doped InGaAs has the highest power factor over both rare earth and Si doped InGaAs.

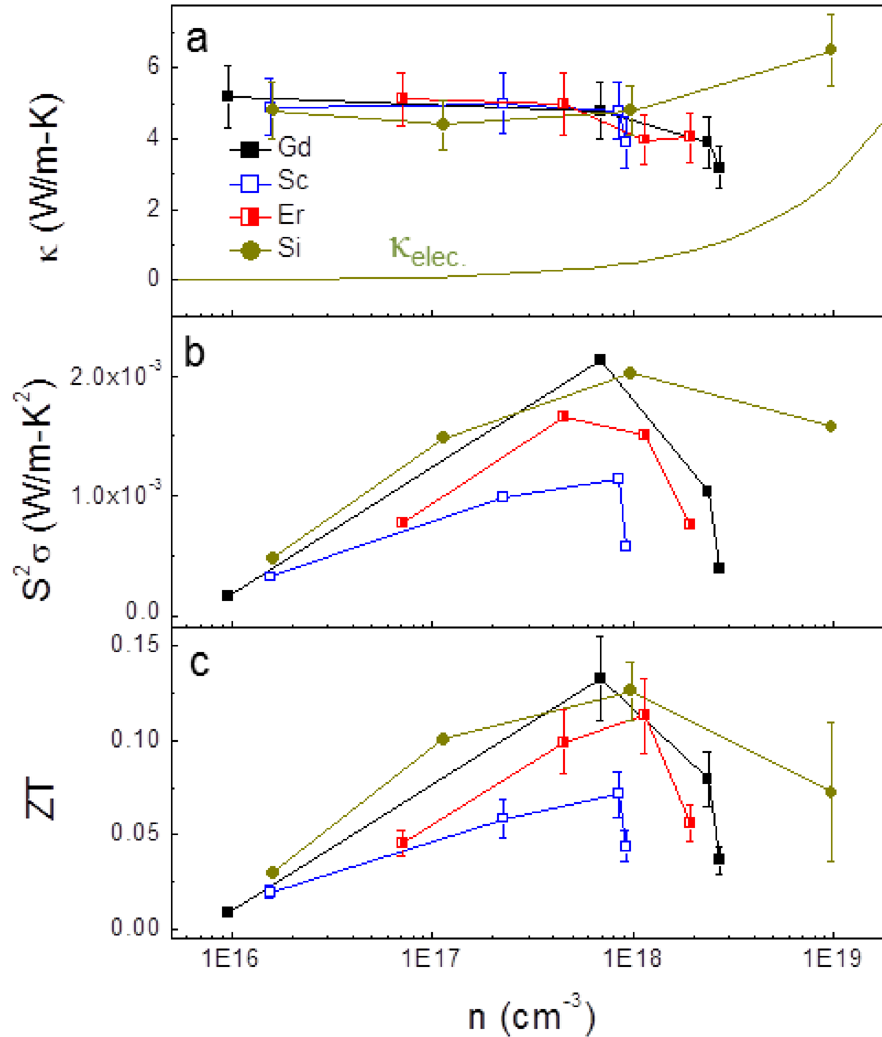

Figure 5.13 Thermoelectric Properties of RE and Si doped InGaAs
a) Total measured and calculated electronic thermal conductivity , b) power factor and c) ZT at room temperature for InGaAs doped with Si, Gd, Er, and Sc as a function of electrically active carrier concentration determined from Hall measurements.

Calculating the ZT from power factor and thermal conductivity leads to a peak ZT around 10^{18} cm^{-3} carrier concentration, similar to the peak power factor. The error bars in ZT are from error in thermal conductivity measurements. The highest room

temperature ZT is seen for 0.1% GdAs doped InGaAs with a value of 0.13. The power factor decreases too sharply after 10^{18} cm^{-3} carriers for the decrease in thermal conductivity at higher rare earth concentrations to compensate, so no improvement in thermal properties from nanoparticle incorporation is seen in the optimal ZT regime. Further studies exploring the doping range 0.1-0.5% RE-As concentration could more precisely define the optimal doping concentration at room temperature.

5.5 Conclusions and Future Work for Gd doped InGaAs

This chapter reports the successful growth of single crystal GdAs films both strained on GaAs and lattice matched to InGaAs. It is seen that unlike its other rare earth counterparts studied, the crystal quality depends strongly on growth temperature and the surface quality depends on As overpressure. The single crystal growth condition allows for single phase nanoparticles to precipitate out during InGaAs growth. Nanoparticle precipitation was confirmed with HRTEM images.

The thermoelectric properties of Gd doped InGaAs were examined and compared with Er, Sc, and Si doped InGaAs. It is seen that doping with rare earths effectively overcomes the Wiedemann-Franz law to decouple the electrical and thermal conductivities, while doping with Si cannot. All three rare earths studied have very similar thermoelectric trends, except for doping efficiency. It is seen that Gd is the most efficient electrical dopant with the least lattice mismatch and Sc is the least efficient electrical dopant with the most lattice mismatch.

Overall, Gd, as a more efficient dopant, has the highest power factor and ZT (ZT_{max}=0.13) over a range of carrier concentration. The higher electrical

conductivity of Gd doping at low concentrations is more effective in improving ZT than the reduced thermal conductivity from GdAs particles at high concentrations. Exploring the doping range between 0.1-0.5% GdAs more carefully could result in higher power factors and ZT. Investigating the effect of growth rate on rare earth solubility and thermoelectric properties could illuminate how rare earths can further improve thermoelectric properties of InGaAs. Overall, Si doped InGaAs has a higher thermoelectric efficiency over a wide range of carrier concentration for this set of growths and measurements, leading to Si having the potential to be a better thermoelectric dopant.

Chapter 6

6 Codoping as a Tool to Improve Thermoelectric Efficiency

This chapter aims to combine traditional and rare earth dopants in InGaAs to effectively map out how to reach the maximum thermoelectric efficiency in the embedded rare earth material system. By codoping InGaAs with rare earths and Si or Be, a maximum power factor can be achieved (in theory) independently of minimizing thermal conductivity. An analysis to describe electrical transport behavior with both n and p-type material will be discussed and tested with ScAs nanoparticles embedded in InGaAs. It is seen that in practice, this theory can be applied with a fixed Sc concentration. However, the low mobility of the ScAs nanoparticles leads InGaAs with varying compositions of Sc to deviate from this analysis, making Si the best thermoelectric dopant at room temperature.

6.1 The Concept of Codoping

Rare earth doping in InGaAs can improve the thermoelectric efficiency in two ways; by adding electrically active carriers to InGaAs, improving the electrical conductivity and by decreasing the lattice thermal conductivity from RE-As nanoparticles. Optimization of room temperature thermoelectric properties in Chapters 4 and 5 shows that doping with rare earths has a maximum thermoelectric

efficiency before a high enough nanoparticle density is reached for significant reduction in thermal conductivity. Therefore, doping with only rare earths takes advantage of only one mechanism of improving thermoelectric efficiency; an increase in power factor.

Since rare earths can be used to dope below and above the maximum power factor regime, it should be possible to 'counterdope' the rare earths. For example, it should be possible to incorporate Sc above the maximum power factor point so that there is a high concentration of nanoparticles to scatter phonons, but too high of a carrier concentration for optimum power factor. The maximum power factor can then be reached by codoping with Be as an electron trap for the excess electrons beyond the maximum power factor point. Since we have seen that incorporating rare earths maintains electrical transport through InGaAs consistent with single parabolic band models as discussed in section 5.4, we know that we can use multiple different types of dopants and maintain conduction through InGaAs. In this way, we can use the more precise ability to control carrier concentration with traditional dopants while increasing phonon scattering from RE-As particles.

6.2 Electrical Transport of Be and Si Codoping with Sc in InGaAs

In this study, Sc was chosen as the rare earth dopant to see if codoping could improve the thermoelectric properties above that of InGaAs. Be was used as a p-type dopant as it sits on a group III site and Si was used as an n-type dopant when it sits

on a group III site. Both Be and Si have a doping efficiency close to 100% over the concentrations used at room temperature[71, 72].

InGaAs films were grown by MBE lattice matched to InP as described in section 3.1. A 200nm InAlAs buffer layer was grown at 490°C on InP to smooth the surface and electrically isolate the active region. Then a 1 μm thick InGaAs film was grown at 1 μm/hr growth rate and codeposited with a fixed Sc flux. The Sc flux was held at ~0.09%, a concentration with dilute nanoparticle incorporation. The carrier concentration of these samples was tuned by codepositing the Sc doped InGaAs films with varying concentrations of Be and Si.

To explore how doping with rare earths affects the underlying transport mechanisms in InGaAs as well as to see how p-type InGaAs behaves, InGaAs was codoped with a single Sc concentration and either Si or Be. Room temperature Hall and Seebeck measurements of codoped InGaAs are compared in Figure 6.1 with Si doped InGaAs as discussed in Chapter 3.2.

It can be seen that the mobility of InGaAs codoped with Sc and Si is significantly lower than InGaAs doped only with Si. This is likely due to increased scattering from nanoparticles and atomic impurities. Although the nanoparticles provide coherent interfaces for electron conduction, there is still significant scattering.

Although the codoped InGaAs has much lower mobility at lower carrier concentrations, the mobility does not drop off as quickly as Si doped InGaAs with increasing carrier concentration. The mobility decreases sharply for Si doped InGaAs because there is an increase in ionized impurity scattering directly proportional to

how many free carriers (ionized Si impurities) are in the matrix. Because Sc can contribute carriers in a number of ways, including from semimetallic particles, the mobility is limited by other processes, such as scattering from the high concentration of atomic Sc impurities as well as ScAs nanoparticles. As more Si is added to Sc doped InGaAs, the increase in ionized impurities makes the curve follow more closely to Si doped InGaAs.

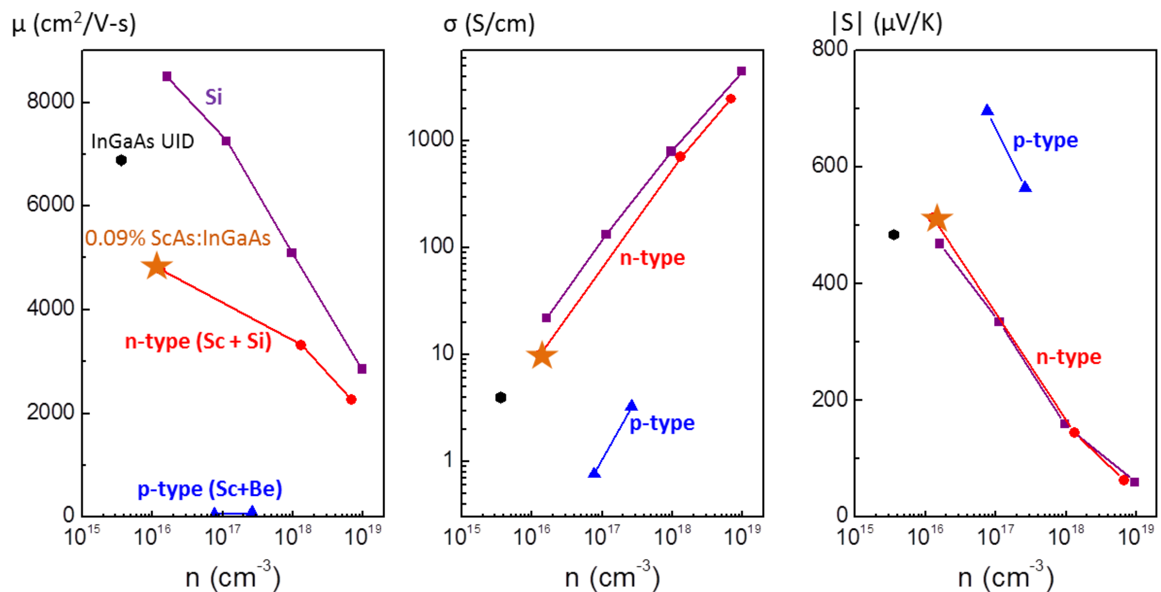

Figure 6.1 Electrical Properties of Codoping with Sc
Room temperature a) mobility, b) electrical conductivity, and c) Seebeck coefficient of InGaAs with n and p-type dopants.

It is important to note that when codoped InGaAs is made p-type by adding Be, the mobility drops by orders of magnitude, from thousands to tens of cm^2/V-s. This sharp decrease in mobility is due to the different dispersion relations for electrons and holes. Holes have an effective mass of $0.4m_e$ while electrons have an effective mass an order of magnitude lower, $0.04m_e$. This difference in effective mass is why

the conductivity for p-type InGaAs is orders of magnitude lower than n-type InGaAs at the same carrier concentration. Both codoped and Si doped n-type InGaAs have similar conductivity trends, with Sc doped samples having a lower conductivity due to its lower mobility.

Seebeck measurements are very telling of transport and scattering mechanisms in InGaAs. In Figure 6.1c, there are two different Seebeck vs. carrier concentration trends for n and p-type InGaAs. P-type InGaAs has a much higher Seebeck coefficient for a given carrier concentration than n-type InGaAs. This is to be expected from single parabolic band transport[103] since holes in InGaAs have a much higher effective mass and the Seebeck coefficient is proportional to the effective mass of the carrier. Both Si doped and Sc codoped InGaAs show very similar Seebeck trends. The Seebeck coefficient of pure Sc doped InGaAs shows the most deviation from Si doped InGaAs, and as more Si is added to Sc doped InGaAs, it appears to track closer to InGaAs doped with only Si. This shows that the changes to electron transport from rare earth doping can be overcome by adding orders of magnitude more carriers from Si.

It is important to note that it is not the number of impurity atoms, but the number of electrically active carriers that matters. Since approximately 0.1% Sc is incorporated in InGaAs, this corresponds to about 10^{19} cm^{-3} carriers, the same concentration as the highest Si doping added. The very low doping efficiency of Sc leads it to track closer to 10^{16} cm^{-3} Si.

Figure 6.1 shows two distinct trends for n and p-type InGaAs. All of the interdependent properties make it difficult to assess from Seebeck versus carrier concentration alone how these materials compare as thermoelectrics. But when we look at properties versus electrical conductivity instead of carrier concentration, we can more clearly identify how these materials behave, independent of carrier type.

Plotting Seebeck coefficient versus electrical conductivity in Figure 6.2 shows one trend for both n and p-type InGaAs. Not only that, but fitting a line to the data has a slope of 86.2 μV/K, which is equivalent to the Boltzmann constant. Using Sommerfeld's free electron model, the Cutler-Mott formula can be derived as shown in the equation below[4].

$$S = -\frac{\pi^2 k_b T}{3e} * \frac{d \ln \sigma(\varepsilon)}{d\ \varepsilon}|_{\varepsilon_F} \qquad (6.1)$$

This equation shows that the Seebeck is proportional to the natural log of the electrical conductivity by a proportionality constant equal to the Boltzmann constant, consistent with our graph. Figure 6.2 shows that codoped InGaAs with Sc has a relationship S=699-86.2*ln(σ). The relationship effectively takes into account the different effective masses of carriers from different bands.

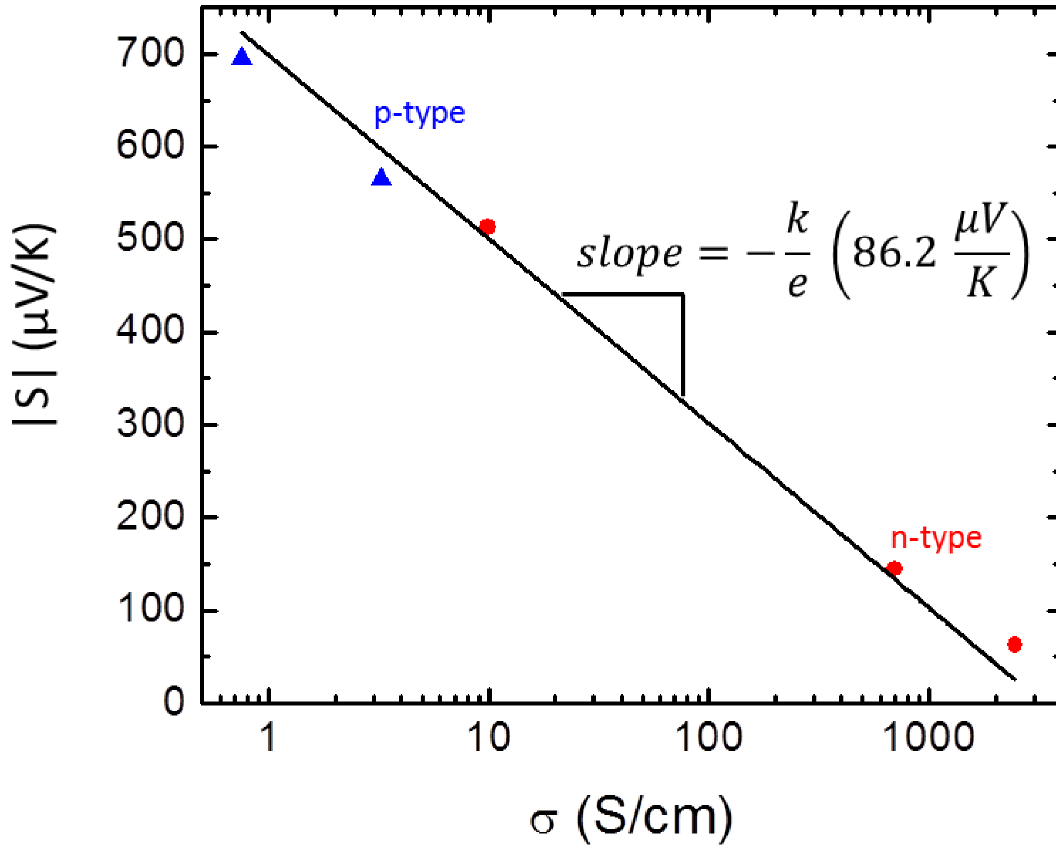

Figure 6.2 Intrinsic Material Relationship of Seebeck vs Conductivity
Seebeck coefficient versus electrical conductivity of Sc doped InGaAs codoped with Si or Be at room temperature follows a single trend independent of carrier type.

Using the fit of the Seebeck versus conductivity, the Seebeck coefficient can be predicted for any value of electrical conductivity. Since the power factor is a function of both Seebeck and conductivity, $PF=S^2\sigma$, the power factor can be predicted for any conductivity value by fitting the Seebeck versus conductivity trends. This allows the power factor to be modeled, showing how tuning carrier concentration to increase or decrease electrical conductivity can effectively reach the maximum power factor point. Figure 6.3 shows the fit to power factor from the Seebeck plot, which indicates

good agreement with Sc codoped experimental data points. Comparing with Si doping, it is seen that Si doping by itself has higher power factor than codoping with Sc. It is important to note that quite high power factors can still be reached with Sc codoping, so it is theoretically possible that the decrease in thermal conductivity from incorporating higher concentrations of Sc can be coupled with counterdoping to reach a higher room temperature ZT than Si doping by itself.

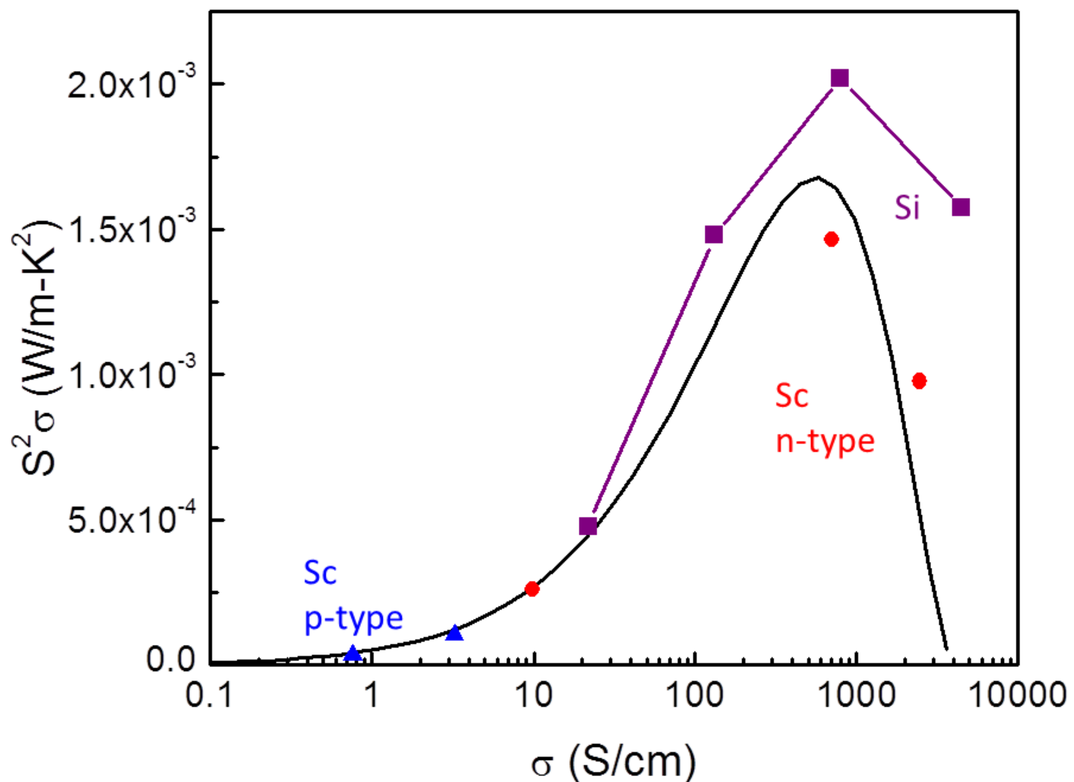

Figure 6.3 Power Factor of Codoped InGaAs
Power factor of Sc codoped and Si doped InGaAs compared to the expected power factor using the fit of the line in the Seebeck versus conductivity plot.

6.3 Price Analysis for ZT Optimization

Since the relationship between Seebeck and electrical conductivity indicates traditional band transport, in order to maximize power factor in a material, we need to know if we can increase the curve in Figure 6.2 to reach higher power factors than traditionally doped InGaAs. Seebeck coefficient is often compared with carrier concentration to understand transport and this relationship has been defined as the Pisarenko Relation[13, 19, 104]. Typical thermoelectric devices have both n and p type materials, which means that there are two different bands contributing to conduction depending on which material is used. Comparing the Seebeck coefficient to the electrical conductivity seems to take that into account, but there has been significantly less discussion in the literature comparing these relations beyond the basic Cutler-Mott formula discussed in the previous section.

In this section, a phenomenological model based on the work of P.J. Price[105] is used to analyze the Sc codoped material system. This model will be referred to as the Price analysis. This can then be applied to varying Sc concentrations to optimize ZT for the Sc doped InGaAs material system. Figure 6.4 illustrates how the Price analysis can be used to understand transport in InGaAs codoped with Sc and Si/Be. Both n and p-type InGaAs have a Seebeck versus conductivity slope equal to the Boltzmann constant.

From this analysis, a minimum conductivity can be estimated, where transport transitions from n to p-type behavior. The maximum Seebeck coefficient can also be evaluated from this analysis. It should be noted that there is a slight offset from zero

for n and p-type material as indicated by the blue dashed line. This offset is a result of differences in effective mass as well as differences in thermal energy transport from an applied electric field, $\delta_{n/p}$. This model fits the experimental data points to determine this phenomenological $\delta_{n/p}$ constant. As shown from the small offset, the thermal responsivity due to hole and electron transport is very similar.

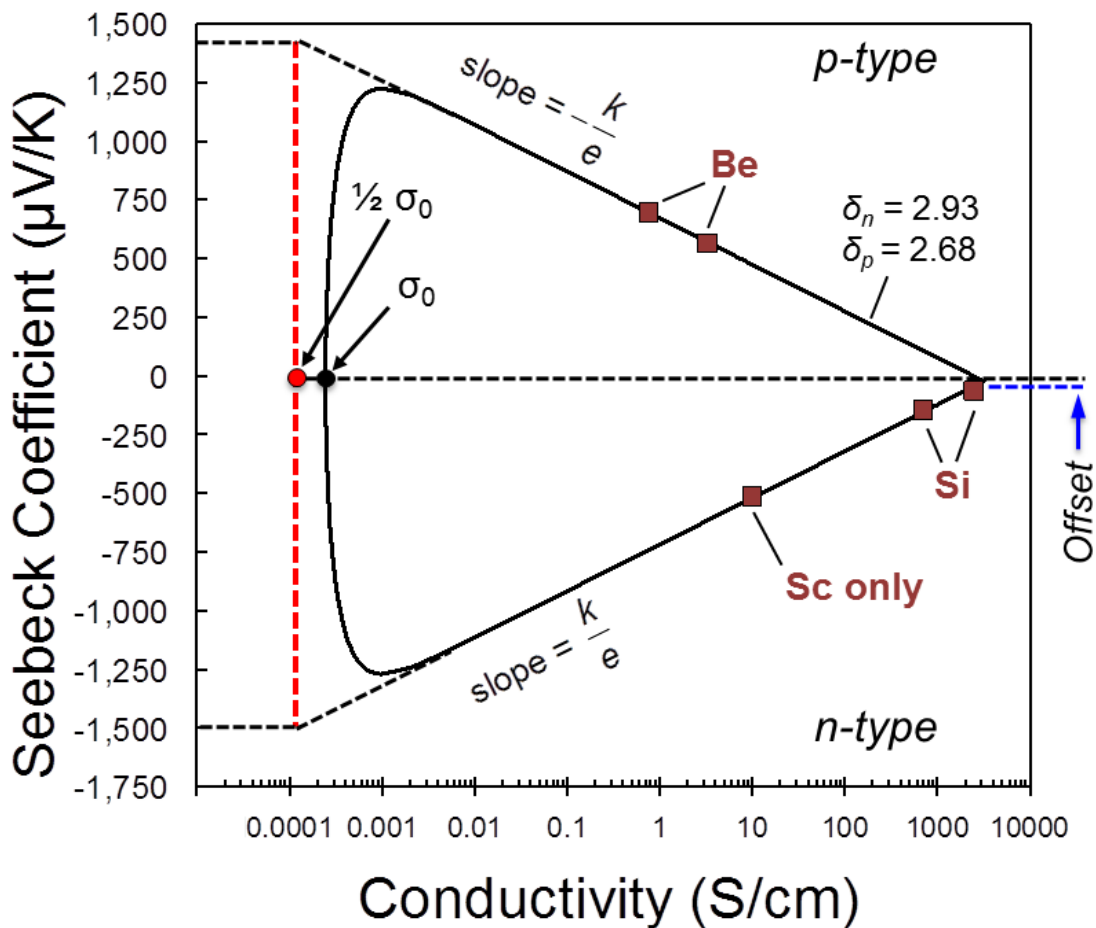

Figure 6.4 Price Analysis
The analysis by Price[105] gives a phenomenological explanation for tuning the Seebeck coefficient.

Now that the thermoelectric properties of InGaAs have been mapped out for a certain Sc concentration, it is important to see how transport changes as more Sc is incorporated. Figure 6.5 compares the Seebeck versus electrical conductivity for varying concentrations of Sc (from 0.01% to 2%) in InGaAs to Si doped InGaAs. The line that connects the points is a guide for the eye as more Sc is incorporated. It can be seen that Si doped InGaAs has the same slope as the lightly doped Sc:InGaAs. However, when varying the ScAs concentration the slope is only constant until 0.5% ScAs incorporation. Above this concentration, the Sc doped InGaAs curve has reached a maximum conductivity and moves away from Si doped InGaAs instead of with it. This is likely due to an increase in ScAs particle density so that band transport through InGaAs alone is no longer a good approximation. It is interesting to note that this deviation from single band transport is not seen in the Pisarenko relation shown in section 5.4.2, it is necessary to look at Seebeck as a function of electrical conductivity.

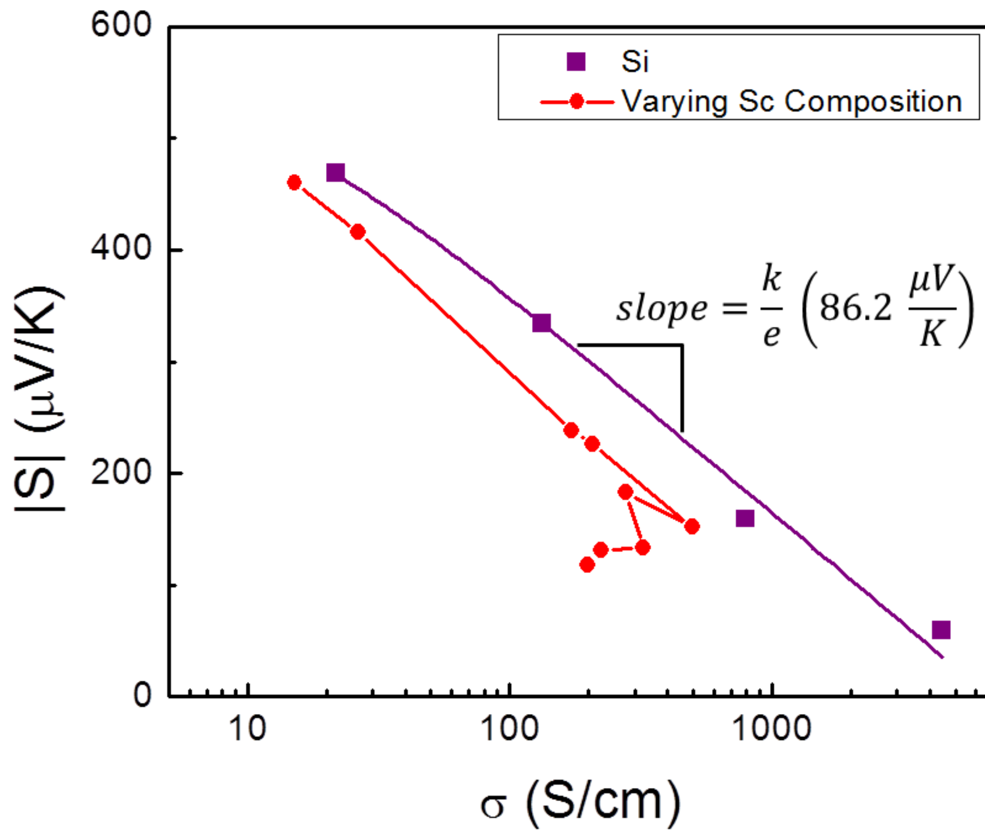

Figure 6.5 Sc Doping Deviates From Single Parabolic Band Transport
Room temperature Seebeck vs electrical conductivity comparing Si and Sc dopants in InGaAs. This relationship deviates from single parabolic band transport after a certain density of nanoparticles form.

This means that the Price analysis done for low Sc concentration will be different for higher Sc concentrations. New Price curves must be generated for each Sc composition in order to address the change in transport that ScAs particles induces. By fitting the known slope to each Sc composition, new Price curves can be generated for each Sc composition. Calculating ZT from the generated power factors and measured thermal conductivity trends from section 4.3, Figure 6.6 shows how ZT can be optimized over varying Sc concentrations.

At low Sc concentrations, ZT can be optimized by using Si to increase the electrical conductivity of InGaAs. However, due to the deviation from parabolic band transport with increased nanoparticle concentration, the maximum ZT decreases as more Sc is added. InGaAs with ScAs nanoparticles (above 0.1% ScAs) is already close to the maximum ZT point without any additional codoping. In these cases, it is unlikely that codoping with Si will benefit the thermoelectric properties, although a more thorough experimental study would be beneficial. For high Sc concentration, the decrease in thermal conductivity is not significant enough to overcome the lower power factors of InGaAs with ScAs nanoparticles. Furthermore, it is not possible to reach the ZT of Si doped InGaAs at room temperature using Sc and Si codoping. Rare earths with higher doping efficiencies, like Gd, should be able to reach the ZT of Si doped InGaAs, but it is unclear whether it can benefit from thermal conductivity reduction from nanoparticles. Certainly at high temperatures, minimal reduction in thermal conductivity will be seen from dilute nanoparticle scattering, due to Umklapp phonon scattering becoming more dominant over other scattering processes[98]. Therefore, improvements in high temperature electron transport should be studied to examine possible improvements from embedded nanoparticles.

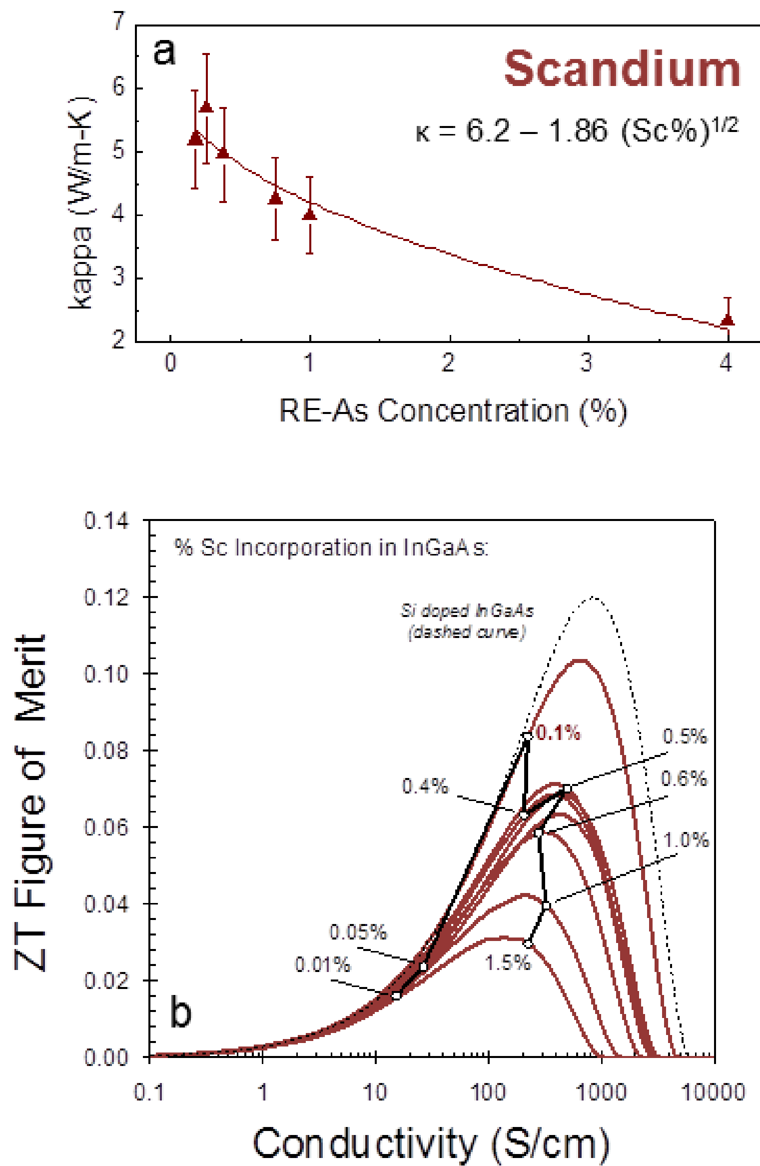

Figure 6.6 Optimization of Sc doped InGaAs

a) Thermal conductivity of Sc doped InGaAs as a function of Sc incorporation and b) ZT calculated from the Price analysis for each Sc composition compared to Si doped InGaAs (dashed line) at room temperature.

6.4 Conclusions

To conclude, we have developed a method to optimize the ZT of a given rare earth dopant using codoping with Si/Be. A trial with Sc codoping was conducted and differences in transport between n and p-type material were identified as well as differences in transport between traditional doping and rare earth doping. It was seen that although the traditional Pisarenko relations cannot effectively compare n and p-type material, using the phenomenological model put forth by Price[105] can effectively compare transport regimes. Plotting Seebeck versus conductivity should follow a straight line for a given material system where the slope is equal to the Boltzmann constant. Investigating varying Sc concentrations, however, does not follow this trend, indicating that ScAs nanoparticles affects transport in InGaAs in a way that the Pisarenko relations cannot illuminate. Applying this phenomenological model gives a sense of how rare earth doping affects transport over a range of electrical conductivities. Overall, this model does not predict improvements in ZT from codoping Sc with Si/Be. Using a more efficient rare earth dopant, such as Gd, could possibly lead to an enhancement and should be the focus of further studies. Overall, rare earth doping does not lead to significantly improved properties over Si doping for thermoelectric power generation.

Chapter 7

7 Literature Summary of Rare Earths in InGaAs

There has been a lot of work done in different groups on the thermoelectric properties of embedded RE-As nanoparticles in InGaAs at room temperature. This chapter compares data gathered in this work as well as previous work to understand how different rare earths impact the thermoelectric properties of InGaAs. It is seen that the most studied material system, Er doped InGaAs, has achieved the highest experimental power factor. However, a fit to Si doped InGaAs shows that Si doped InGaAs has the potential to have a higher power factor than any rare earth studied.

The solid Gd, Sc, Er, Si and UID points were taken from this work as well as the open Sc, Er and ErSc points grown on InGaAs buffers, as compared to InAlAs that almost all other works used. Tb doped InGaAs was grown on InGaAs or no buffer layer and the data was taken from Clinger, et. al.[45]. Ce and 'Burke Er' data points were taken from Peter Burke's thesis[14]. Other rare earths studied by Hong Lu and Peter Burke[14] showed poor thermoelectric performance, so they will not be included in the comparison here.

One thing to keep in mind when comparing different rare earths as dopants is that the samples in these studies were grown under different growth conditions. It has been shown in previous work as well as this work that the electrical properties of rare earth doped material are very sensitive to growth parameters such as growth

temperature[47] and layer structure. It is also likely that electrical properties are sensitive to other growth parameters such as growth rate or V/III ratio.

7.1 Electrical Comparison of Rare Earths

This dissertation has shown so far that the most efficient dopant in InGaAs leads to the highest ZT. Comparing this work to other studies of rare earth doped InGaAs can illuminate whether this is the dominant factor in achieving high power factor. Despite increased phonon scattering from RE-As nanoparticles compensating the Wiedemann-Franz law by decreasing the total thermal conductivity at high electrical conductivities, the highest ZT occurs at a low rare earth concentration, below the point where phonon scattering from RE-As nanoparticles leads to any significant decrease in thermal conductivity.

Figure 7.1 shows that most of the rare earths studied have the same trends. There is never as high of a doping efficiency as Si, but the electrically active carrier concentration increases at lower rare earth concentrations and starts to plateau between 10^{19}-10^{20} cm^{-3} rare earth concentration. Gd, Er and Tb can reach electrically active carrier concentrations of ~$2x10^{18}$ cm^{-3}, while Sc reaches about half of that. The doping efficiency of Er doped InGaAs grown on InAlAs buffer layers from this work is in good agreement with previous work on Er doped InGaAs[14]. Since Gd and Er have been seen to have the highest thermoelectric power factors, this suggests that the more efficient dopant a rare earth, the better a thermoelectric. It is important to note that Er and Sc doped InGaAs grown on an InGaAs buffer layer (open markers) shows a higher doping efficiency, which leads to a higher power factor.

This is likely an artifact of parallel conduction through the buffer layer and not representative of the film properties.

Tb does not reach its peak carrier concentration until much higher Tb incorporation than Er or Gd, leading to lower doping efficiency as well as lower thermoelectric power factor. In the case of high concentration of Tb ($>10^{21}$ cm^{-3}), the carrier concentration begins to decrease. TEM shows that there is a greater ratio of Tb atoms inside particles than at a TbAs/InGaAs interface[45], which is consistent with particles contributing carriers from thermal excitation of electrons across the interface as described in Section 4.3.1.

Ce sees a quite different trend in electrical activation. It reaches its peak carrier concentration at a much lower Ce incorporation and decreases in carrier concentration when more Ce is added. This is theorized to be a result of atomic Ce favoring a neutral substitutional site rather than an interstitial site[14].

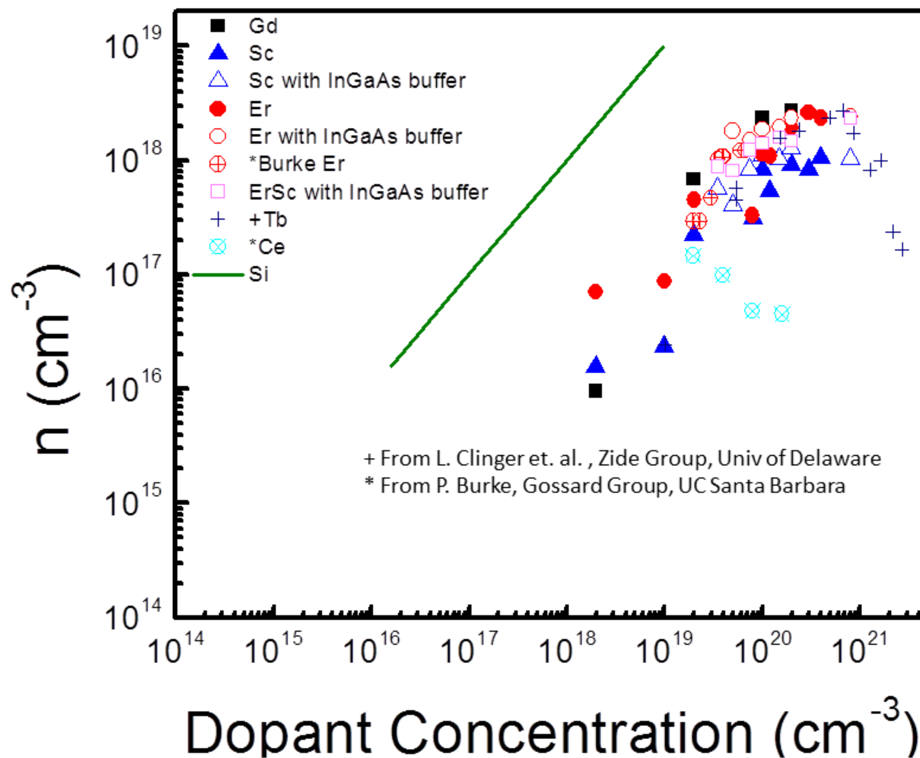

Figure 7.1 Doping Efficiency in InGaAs
The electrically active carrier concentration from Hall measurements is plotted for different rare earths from this work as well as literature values versus dopant concentration. Si doping has nearly 100% doping efficiency over the doping range explored.

The previous chapter showed that comparing the Seebeck as a function of electrical conductivity is a good way to explore how improvements to the thermoelectric properties of InGaAs can be realized. If a dopant lies above the trend of Si doped InGaAs, then it is a more efficient thermoelectric dopant than Si doped InGaAs.

Figure 7.2 shows that most of the rare earths studied have Seebeck coefficients that lie below the Si doped InGaAs trend found in the previous chapter. Some of the

low Er and Tb doped InGaAs lie above the trend for Si doped InGaAs developed in the previous chapter, but the conductivity is too low to improve power factor on a larger scale. This means that no power factor improvement is seen by incorporating rare earths in InGaAs and the rare earths can only achieve similar power factors to Si doped InGaAs at room temperature. As shown in the previous chapter, increasing rare earth concentration approaches the trend to Si doped InGaAs until a critical rare earth concentration is reached, where the decrease in mobility decreases the electrical conductivity as more rare earth is incorporated, deviating from the Si doped InGaAs trend.

The unintentionally doped (UID) InGaAs sample has a Seebeck coefficient below the trend of all doped material. This is due to impurities in InGaAs, likely C, compensating the background n-type carriers, reducing the Seebeck coefficient due to bipolar conduction. Consistent with the highest power factor samples seen in Figure 7.1, the best Er and Gd doped samples reach the theoretical limit for Si doped InGaAs, although do not surpass it.

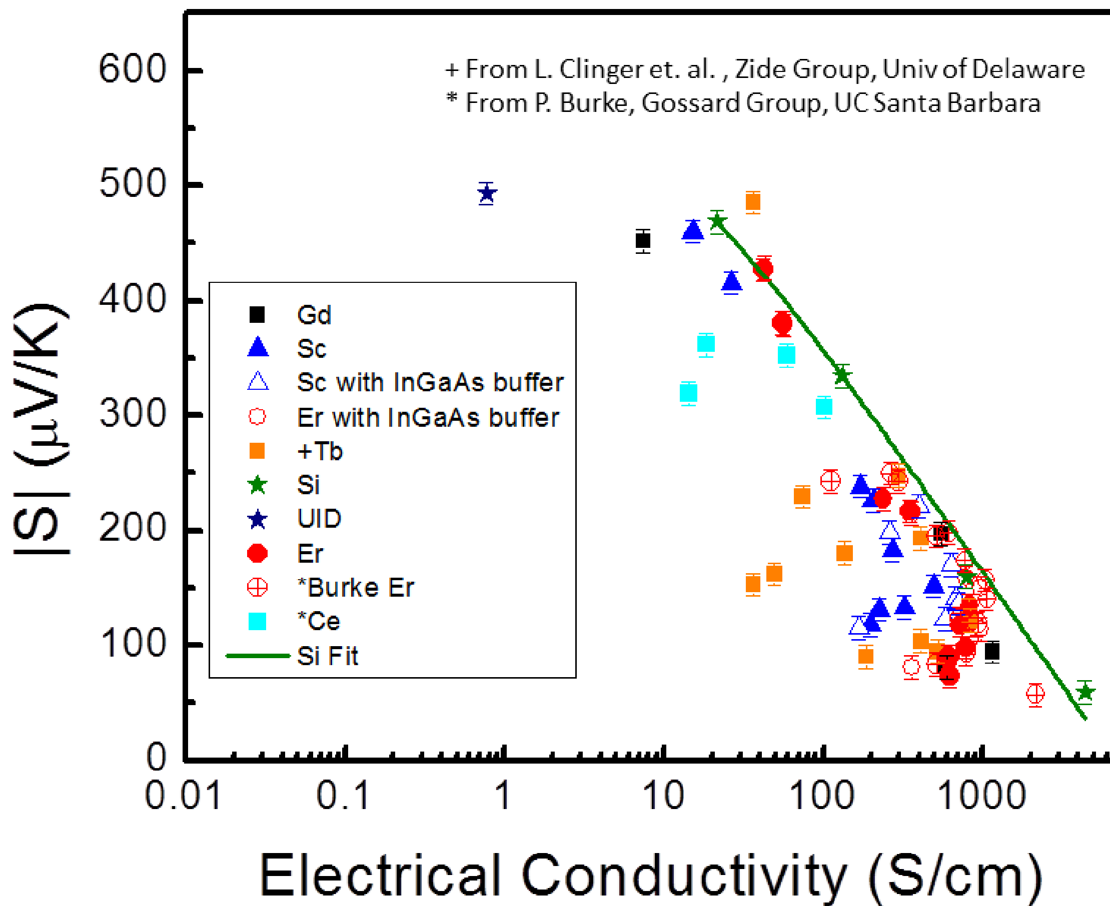

Figure 7.2 Comparison of Seebeck for Different Rare Earths
The electrical conductivity versus magnitude of Seebeck coefficient is plotted for all samples in this work, as well as relevant literature values. The error in the measurement setup is +/- 10 μV/K. All data points below the Si fit line developed in the previous chapter are less efficient thermoelectrics than Si doped InGaAs.

This is further shown in Figure 7.3, where the highest power factors achieved are the rare earth doped InGaAs that came closest to the Seebeck trends for Si doped InGaAs. Overall, using the analysis described in the previous chapter, the Si doped InGaAs trend has a higher predicted power factor than any of the rare earths studied, although some of the Er doped InGaAs from Peter Burke's thesis[14] comes close.

However, this Si doped trend is not corroborated by experimental data at the maximum power factor point, so more Si doped InGaAs in this doping regime would be prudent to make a more accurate comparison of rare earths to Si doped InGaAs in the high power factor regime. However, there is experimental evidence for higher power factors from Si doped InGaAs in the high and low carrier concentration regime, leading one to expect higher power factors in the 10^{18} cm^{-3} regime as well.

Since the peak power factor occurs at low rare earth concentrations, once too much rare earth has been incorporated, the power factor decreases due to a decrease in mobility from the RE-As particles, causing spread in the data shown in Figure 7.3.

It is important to note that Si, with almost 100% doping efficiency over the doping range explored, has the potential to reach higher power factors than any of the rare earth dopants. Experimentally, Si doped InGaAs has reached power factors commensurate with Er and Gd dopants at $2x10^{-3}$ $W/m\text{-}K^2$.

In this work, it is seen that Er doped InGaAs with an InGaAs buffer layer has a higher doping efficiency and therefore a higher power factor than Er doped InGaAs on an InAlAs buffer layer. This is likely due to parallel conduction in the buffer layer that is difficult to isolate in the electrical transport measurements. Therefore, samples with InGaAs buffer layers do not provide a good comparison. In order to isolate transport to the rare earth doped region, samples grown with InAlAs buffer layers provide a more accurate measurement of doping efficiency, as shown by the solid Er and Sc points.

Lastly, it can be seen that the highest power factors from rare earth dopants are from Peter Burke's work with 2 μm thick Er doped InGaAs on an InAlAs buffer layer grown at 2μm/hr. The peak power factor achieved by Burke[14] was significantly higher than the measured peak power factors of the Er doped InGaAs from this work. It is possible that because the peak power factor occurs over a narrow doping range, we have not fully captured the peak in power factor for Er, Gd, or Sc dopants.

Furthermore, it has been seen that the electrical properties of rare earth doped InGaAs are very sensitive to growth conditions. Exploring how growth conditions, such as growth rate and As overpressure, affect the thermoelectric properties of these rare earth doped materials could shed light on how to optimize this material system further.

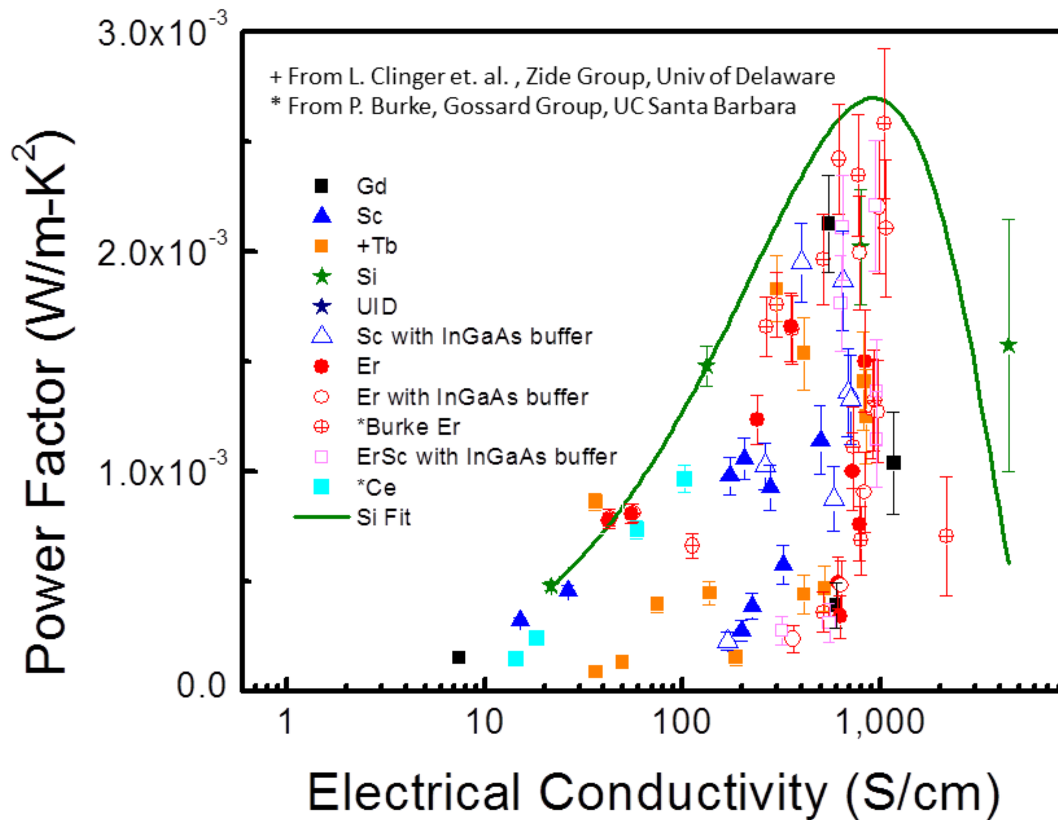

Figure 7.3 Comparison of Power Factor for Different Rare Earth Dopants
The power factor is plotted as a function of electrical conductivity for all samples in this work as well as relevant data from literature. Error bars are taken from the error in Seebeck measurements. It can be seen that there is a peak power factor for all dopants around 1,000 S/cm. Er doped InGaAs from Burke's thesis[14] are the highest power factors reported, but our model for Si doped InGaAs predicts that Si can reach higher power factors than the best experimental data.

7.2 Conclusions

To conclude this section, a comparison of different rare earths in InGaAs shows that different growth conditions for Er doped InGaAs have been able to achieve higher power factors than both the Er and Gd doped InGaAs studied in this work. Given the sensitivity of rare earth dopants to growth conditions, it is expected that by

tuning the growth parameters, higher power factors for Gd doped InGaAs will be seen to support the higher doping efficiency over Er seen in this work.

Furthermore, comparing all of the rare earths to Si doped InGaAs, it is seen that even the highest power factor samples doped with Er can only approach the theoretical limit for Si doped InGaAs at room temperature. Since these high power factor samples occur for low rare earth concentrations (<0.5%) in all studies, no benefit is expected to be seen from thermal conductivity reduction.

Chapter 8

8 Temperature Dependent Comparison of Rare Earth and Traditional Dopants

So far, this dissertation has discussed the room temperature thermoelectric properties in order to compare different rare earths to traditionally doped InGaAs. Since thermoelectric efficiency is directly proportional to carnot efficiency, high temperature operation is desired. This section describes high temperature electrical conductivity and Seebeck measurements to compare the electronic power factor of each material system. It is seen that Si doping reaches a higher power factor than Gd over the temperature range explored. The Si doped InGaAs in this study achieves the same power factor as the best previously reported Er doped InGaAs at high temperature[14].

The room temperature thermoelectric data discussed in previous sections revealed that embedding RE-As nanoparticles was only advantageous compared to experimental Si-doped material at one Gd doping level and a few Er doping levels, and even then, not by a significant amount. Trends extracted from Si doped InGaAs show that it has the potential to be a more efficient thermoelectric than any of the rare earths studied. At higher temperatures, the semimetallic RE-As nanoparticles should act as an additional source of free carriers in InGaAs not available to more conventional, Si-doped material.

This section uses temperature dependent electrical measurements, including Hall, Seebeck and electrical conductivity, as a tool to understand the different doping mechanisms at play using rare earths as dopants. There are differences in doping mechanisms depending on the concentration of rare earth used as seen by temperature dependent Hall and conductivity. Overall, no unexpected trends are seen between Seebeck and electrical conductivity to claim "resonant" doping properties or multiple band conduction as described in other noted material systems that have achieved high ZT[19, 23].

The metallic nature and band alignment of GdAs nanoparticles leads it to be a good high temperature dopant. However, at high temperature, Si doped InGaAs has a higher power factor than Gd doped InGaAs. Ultimately, Si is identified as the most efficient thermoelectric dopant at room and high temperature.

8.1 High Temperature Hall Effect

To examine thermal excitation of RE-doped material, high temperature Hall measurements were done in an Ar environment. In this chapter, all of the samples studied were 4 μm thick InGaAs doped with either Si, Gd, Er, or Sc as described in previous chapters. Figure 8.1 compares the high temperature electrical properties of Si- and Gd-doped InGaAs, and provides evidence to suggest different transport mechanisms are at play in the different materials. In Figure 8.1a, it can be seen that the carrier concentration of Si-doped InGaAs is independent of temperature, indicating that the Si donors have been fully ionized at room temperature. Since the intrinsic carrier concentration of InGaAs at 600K is 2×10^{15} cm^{-3}, InGaAs is still in an

extrinsic regime at this temperature. However, thermal activation of carriers can be seen in both of the Gd-doped samples. This thermal activation can come from levels contributed from both atomic impurities contributing states close to the conduction band edge as well as nanoparticles acting as a large source of thermally activated carriers.

The trends in carrier mobility (Figure 8.1b) are most evident between the high doping concentration and low doping concentration samples, independent of dopant type. Both 0.1% Gd doped InGaAs and $1x10^{18}$ cm^{-3} Si doped InGaAs show steep decreases in mobility as temperature is increased. This is due to increased phonon scattering with temperature. In the highly doped samples, the mobility decrease is much slower with temperature, indicating that ionized impurities have surpassed phonons as the primary scattering mechanism. Together, these trends create a crossover point near 600 K where the conductivity of 1% Gd doped InGaAs becomes higher than $1x10^{18}$ cm^{-3} Si doped InGaAs. It is theorized that thermal excitation from GdAs nanoparticles is the source of this increase in electrical conductivity with temperature at high Gd incorporation. Furthermore, it is expected that at higher temperatures than measured here, a crossover point between the electrical conductivity of 0.1% Gd doped and $1x10^{18}$ cm^{-3} Si doped InGaAs will occur, leading to larger power factor enhancement in the Gd doped InGaAs. $1x10^{19}$ cm^{-3} Si doped InGaAs is not shown in the conductivity plot because the large carrier concentration leads to a much larger electrical conductivity than the other samples measured. Since this sample is limited by ionized impurity scattering, the shallow decrease in

mobility leads to a shallow decrease in electrical conductivity compared to $1x10^{18}$ cm^{-3} Si doped InGaAs. Above 500K, the semi insulating InP substrate starts to become conducting, overwhelming the electrical measurement of the film.

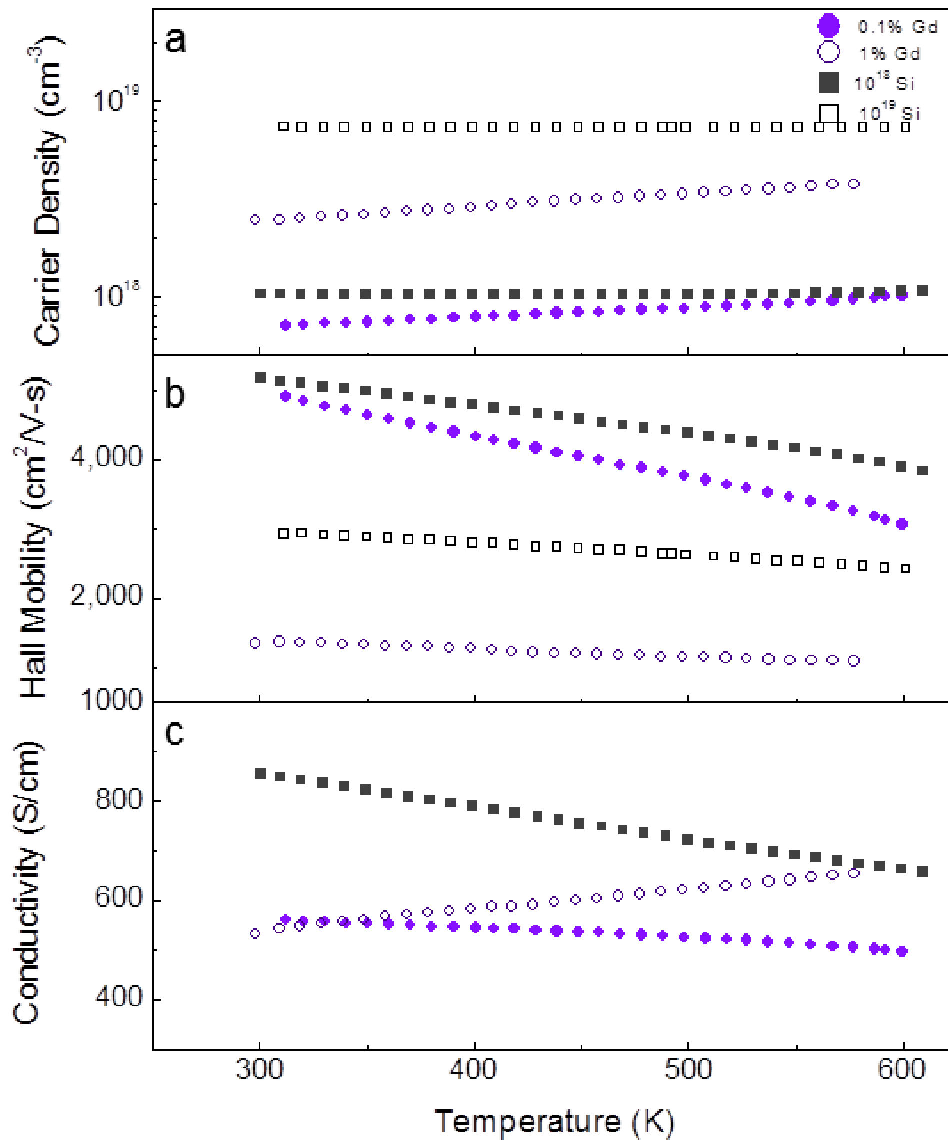

Figure 8.1 High Temperature Hall

a) Carrier concentration, b) Hall mobility, and c) electrical conductivity of Gd doped and Si doped InGaAs as a function of temperature. The electrical conductivity of 10^{19} Si is too large to be shown in this plot, but remains relatively flat with temperature.

8.2 Low Temperature Hall

Although low temperature measurements will not lead to improved thermoelectric efficiency, they show differences in transport properties in a temperature regime where conduction of the InP substrate is not an issue. This section describes low temperature Hall measurements of Gd and Sc doped InGaAs and subsequent activation energies extracted.

Figure 8.2 shows the low temperature Hall results for Gd and Sc doped InGaAs. The mobility data shows very different trends than what is seen for Si doped InGaAs as described in section 3.2.3. Instead of an increase in impurity concentration showing higher temperature mobility peak as scattering transitions from impurity limited to phonon limited as with Si doping, the Gd and Sc doping sees a decrease in the temperature of this transition as more rare earth is incorporated. This is likely due to the nanostructures formed at high rare earth incorporation. In theory, there should not be increasing concentrations of atomic impurities, but more nanoparticles forming as more rare earth is added. It is possible that the higher concentration of nanoparticles leads to less atomic impurities because there is less distance an atomic impurity has to move on the surface in order to incorporate as an energetically favorable nanoparticle. In this way, adding more rare earth would actually decrease the atomic impurities in the sample, therefore decreasing the temperature of the mobility peak.

Similarly, the mobility decreases much more slowly with temperature at lower Gd incorporation, where the mobility peak is shifted to higher temperatures. This is

indicative of higher atomic ionized impurity incorporation. However, the Sc doped InGaAs has the opposite mobility trend. The mobility decreases more steeply with temperature as the mobility peak is shifted to higher temperatures. These two trends are inconsistent and suggest that multiple scattering mechanisms contribute to transport with incorporation of Sc.

One open question is how the electrodynamics change between substitutional and interstitial impurities. It has been theorized that because rare earths tend to be in the +3 charge state, substitutional impurities are electrically neutral while interstitial impurities contribute electrons into conduction and are a major contributor of carriers to InGaAs[43]. However, rare earths have one electron in the d-orbital and completely full p- shells, so sp^3 bonding that typically occurs in III-V semiconductors cannot occur with substitutional rare earth impurities. Furthermore, atom probe results on Sc doped InGaAs suggests that Sc incorporates in a +2 charge state, indicating that a different bonding mechanism is at play and Sc could potentially be an acceptor if incorporating substitutionally. These different charge states and impurity sites could be a reason why the doping efficiency of rare earths is so much lower than that of Si.

For the lowest concentration of rare earth (0.01%), below the expected solubility limit, the Gd doped InGaAs increases carrier concentration by an order of magnitude, where the Sc doped InGaAs only doubles its carrier concentration. The slower increase in carrier concentration for Sc doped InGaAs is a sign of either ScAs particles, deeper donor levels, or compensating acceptor levels contributed from

substitutional impurities. It is believed that interstitial rare earths contribute shallow donors to InGaAs, consistent with the 0.01% Gd doped InGaAs and its steep increase in carrier concentration [42, 43]. At higher rare earth concentrations, the carrier concentration increases at about the same rate with temperature. This indicates that thermally excited carriers are being excited from RE-As particles with similar Fermi levels.

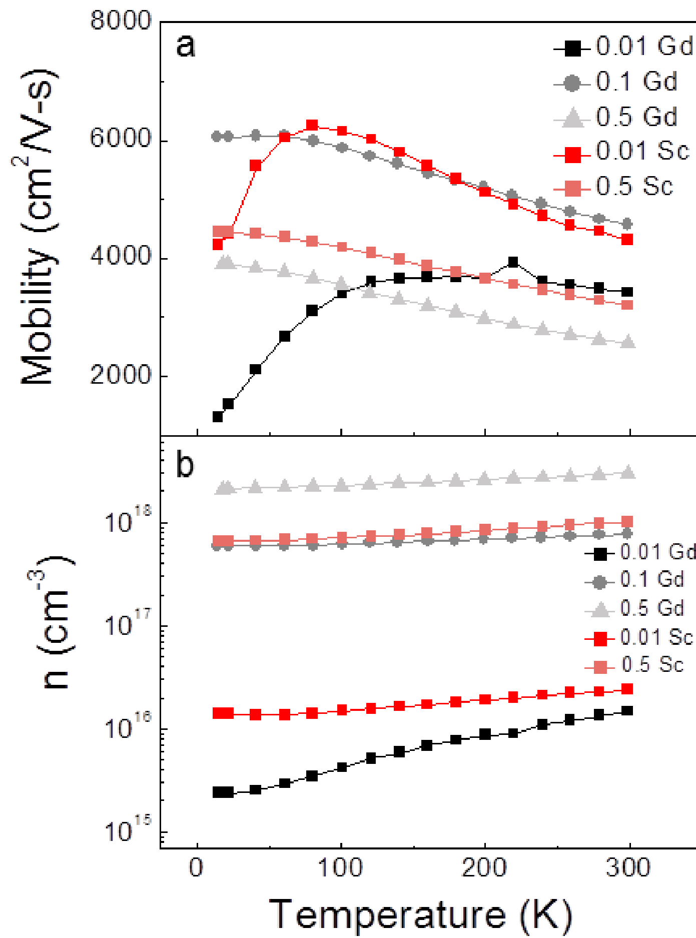

Figure 8.2 Low Temperature Hall of Sc and Gd Doped InGaAs
a) Mobility, b) 3D carrier concentration for Gd and Sc doped InGaAs from 10-300K.

Overall, the electrical conductivity trends vary with rare earth type and incorporation as shown in Figure 8.3. The electrical conductivity increases with temperature for 0.01% rare earth doped InGaAs as shown in Figure 8.3c due to its sharp increase in carrier concentration with temperature. This sample is the only one, including the unintentionally doped InGaAs from Figure 3.9, where thermal activation of carriers was seen at low temperatures. This corresponds to an activation

energy of ~34 meV as shown in Figure 8.4. The activation energy of this Gd doped sample is about twice as large as the activation energy seen in unintentionally doped InGaAs, which has impurity states from both donors and acceptors. A much slower increase in electrical conductivity with temperature is seen for the same 0.01% concentration of Sc, possibly due to the formation of ScAs particles at this concentration. 0.01% Sc doped InGaAs has a thermal activation similar to the higher rare earth doped InGaAs concentrations. This indicates that 0.01% Sc concentration has ScAs particles. All of the rare earth doped samples where particles are expected to form have a calculated activation energy of ~3-9 meV at low temperature. These are not very strong trends and indicate that the energy level of RE-As particles lies closer to the conduction band edge than atomic impurities. Although the measured barrier height of ErAs on InGaAs is ~100meV[33], it is possible that quantum confinement raises the ground state energy level of the particle, decreasing this barrier height.

Using a simple 1D particle in a box model for calculating the rising energy level due to quantum confinement assuming a free electron mass, the ground state energy level will increase from 1.6eV to 14.8 eV as the lengthscale decreases from 3 nm to 1 nm. Although the magnitude of the energy change is greatly exaggerated from this simple model, the trend is consistent with the strain nucleated particle argument described in Section 4.3.1. If GdAs, as a lattice matched RE-As, forms smaller strain nucleated particles, the Fermi level will rise more due to quantum confinement, decreasing the barrier height for thermal excitation of carriers and allowing more free

carriers to be thermally excited from particles at a given temperature. ScAs, with larger lattice mismatch, and therefore larger strain nucleated particles, will have a shallower rise in the ground state energy level from confinement, giving ScAs particles a larger barrier into conduction in InGaAs.

0.1% Gd doped InGaAs has a more similar electrical conductivity to 0.5% Sc doped InGaAs due to the higher doping efficiency of Gd. It is interesting to note that the electrical conductivity of 0.5% Sc doped InGaAs increases with temperature, whereas both 0.1% and 0.5% Gd doped InGaAs decrease with temperature. However, it is seen in Figure 8.5a that the electrical conductivity of 1% Gd doped InGaAs also increases with temperature. This is likely due to the increased density of nanoparticles acting as a source of thermally excited carriers. If this is indeed the cause of the increase in electrical conductivity with temperature at higher rare earth concentrations, it is possible that the Sc doped InGaAs has a higher volume concentration of nanoparticles at a given rare earth incorporation.

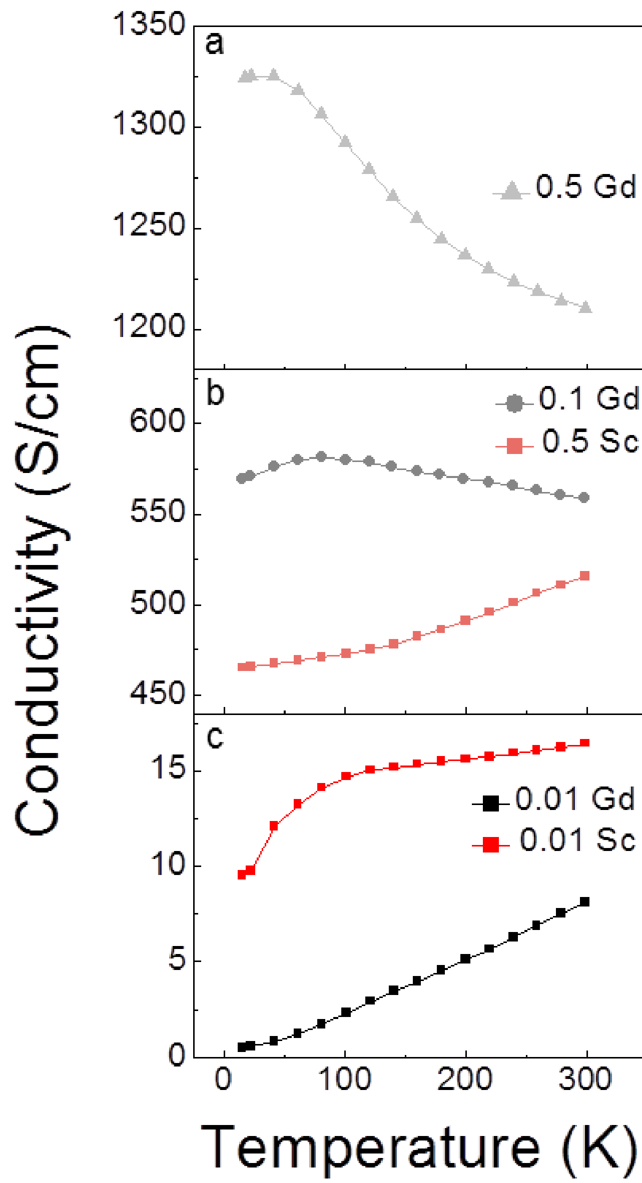

Figure 8.3 Low Temperature Electrical Conductivity

Low temperature electrical conductivity for a) 0.5% Gd doped InGaAs, b) 0.1% Gd and 0.5% Sc doped InGaAs and c) 0.01% Gd and 0.01% Sc doped InGaAs.

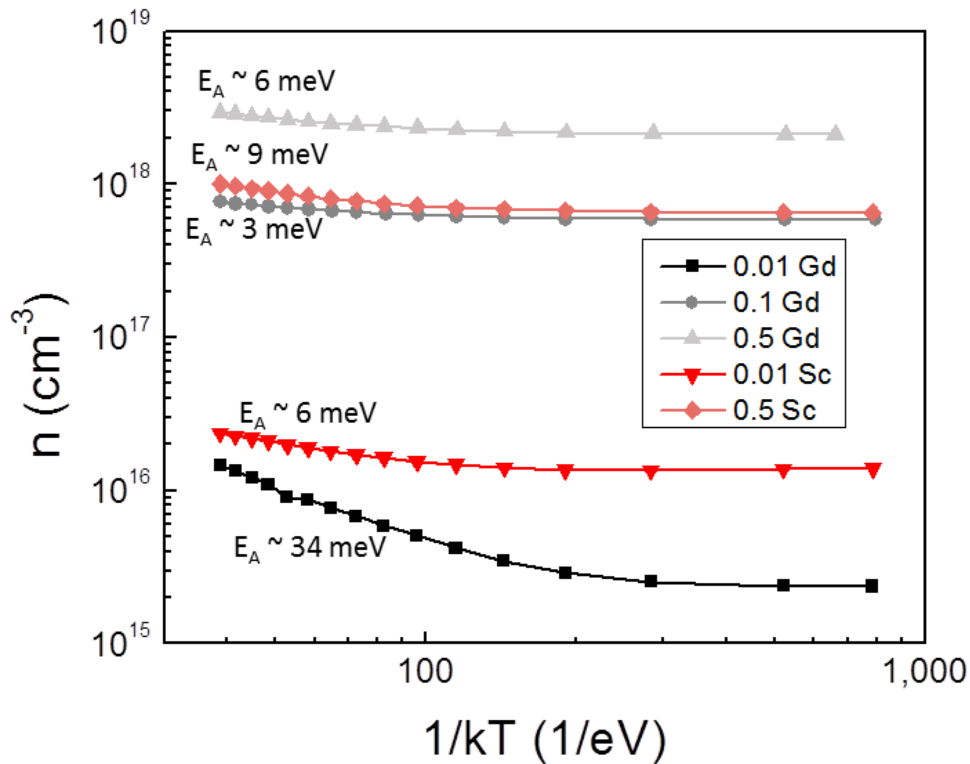

Figure 8.4 Activation Energy of Gd and Sc doped InGaAs
Carrier concentration versus 1/kT is plotted to extract activation energies for InGaAs doped with 0.01% Gd, which is below the estimated solubility limit, and for 0.01% Sc, 0.5% Gd, 0.1% Gd, and 0.5% Sc where transport shows nanoparticles are present.

To conclude the low temperature section of this chapter, it is shown how low temperature transport can give information on transport properties of InGaAs that act as clues to how the rare earths incorporate in InGaAs. However, more studies are needed to accurately define how particles or atomic impurities contribute states to InGaAs.

8.3 High Temperature Thermoelectric Properties

This section first compares the high temperature properties of high efficiency Si and Gd samples to explore how electrical conductivity relates to Seebeck with temperature. Then a wider range of doping concentration is explored to optimize power factor at both room and high temperature.

Figure 8.5a summarizes that the electrical conductivity of Si doped InGaAs decreases with temperature while the electrical conductivity of Gd doped InGaAs decreases much more slowly, or even increases with temperature when there is a high enough nanoparticle concentration. Temperature dependent Seebeck measurements in Figure 8.5b show that the slope corresponds with mobility trends of Figure 8.1b. The lower doped InGaAs has a steeper decrease in mobility with temperature as well as a steeper increase in Seebeck with temperature due to stronger phonon scattering at high temperature. The error bars represent the scatter over multiple measurement runs as well as error in Seebeck due to the tungsten probes. When impurity scattering dominates transport in highly doped InGaAs, the slope in the Seebeck vs temperature plot is about half of what it is when phonon scattering is the dominant scattering mechanism in the lower doped samples. It is important to note that the Seebeck coefficient sees a roll off at high temperature. This is due to substrate conduction and will be discussed in the next section.

The highest power factors are observed for the lower doped samples, as was the case at room temperature. Figure 8.5c shows that 0.1% Gd-doped InGaAs has a

slightly higher power factor at room temperature, but the roll off of the Seebeck coefficient leads the 1e18 Si to have a higher power factor above 400K.

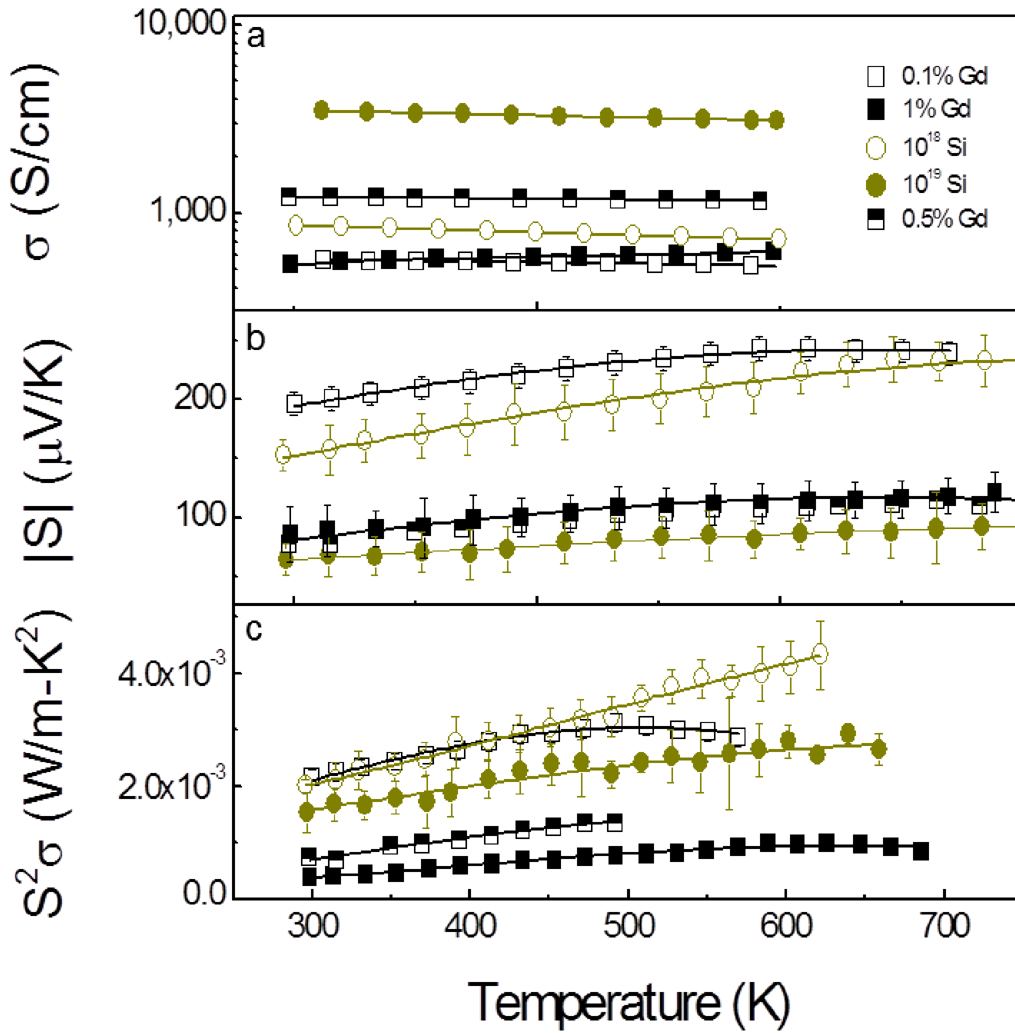

Figure 8.5 Power Factor of Si and Gd doped InGaAs
High temperature results for (a) electrical conductivity, (b) Seebeck coefficient, and (c) power factor for Si and Gd doped InGaAs. Low electrical conductivity InGaAs sees substrate conduction effects at lower temperatures.

8.3.1 InP Substrate Conduction and Bipolar Conductivity

As discussed in the previous section, signs of InP substrate conduction are seen at about 500K as the Seebeck coefficient and power factor of 0.1% Gd doped InGaAs starts to roll off.

InP is doped with Fe to be semi insulating at room temperature. Fe acts as a midgap trap for carriers. At high temperatures, thermal energy excites electrons from the Fe trap states into conduction as well as valence electrons into trap states. Since InGaAs has a relatively narrow bandgap, there are also minority carriers in InGaAs excited into conduction at high temperature. Bipolar conduction reduces the overall Seebeck coefficient since both electrons and holes will move with the thermal gradient, essentially cancelling the thermal voltage. Using heterostructures to block minority carrier conduction has been shown to effectively increase the Seebeck coefficient at high temperatures and reduce the thermal conductivity by reducing bipolar conduction[13, 14, 106].

Roll off of the Seebeck coefficient is particularly noticeable in low conductivity samples, since the proportional increase in thermally excited charge carriers is larger. To avoid thermal excitations from substrate conduction, films should be transferred to more insulating substrates, such as sapphire as shown in Figure 8.6[107]. It can be seen in the high temperature electrical conductivity measurement that there is a significant increase at high temperature which can be removed by transferring the film onto a more insulating substrate.

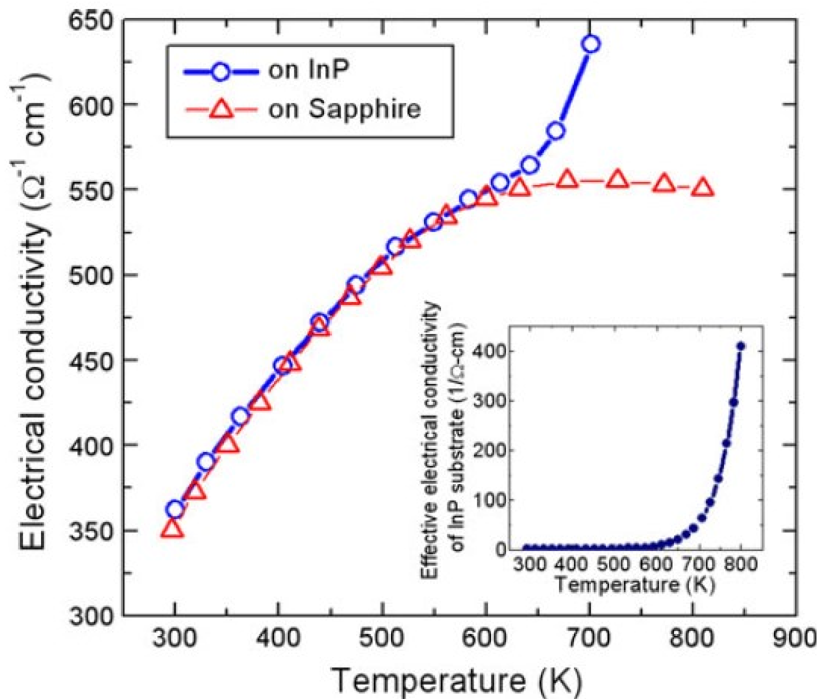

Figure 8.6 Effect of InP Substrate Conduction on Electrical Conductivty[107]**.**
Comparison of electrical conductivity measurements of 0.6% Er doped InGaAlAs on an InP substrate and transferred to an insulating sapphire substrate. Thermal activation of carriers in the InP substrate leads to a sharp increase in the measured electrical conductivity with temperature that is not seen on a sapphire substrate.

The cross over in power factor for Si doped InGaAs above 0.1% Gd doped InGaAs seen in Figure 8.5 is possibly an artifact of substrate conduction and can be overcome by transferring InGaAs films to a more insulating substrate. Measuring these films on insulating substrates will also help quantify bipolar conduction effects in InGaAs. Substrate conduction limits the temperature to which these films can be reliably measured[107]. Attempts have been made to transfer the RE-doped InGaAs films to a more insulating substrate to allow characterization of these materials to much higher temperatures. Previous techniques relied on making holes in InGaAs

films to reduce surface roughness, which voids the basic assumption for electrical conductivity measurements. InGaAs film transfer to sapphire substrates via flip chip bonding loosens the requirements on film roughness and will be described in Appendix A.

8.3.2 Summary of High Temperature Properties

Figure 8.7 shows the electrical conductivity, Seebeck and measured power factors for all of the Si and Gd doped InGaAs samples grown as well as the highest power factor samples (0.1% Er/Sc) for Er and Sc doped InGaAs. All of these films are 4 μm thick and were grown at a growth rate of 1μm/hr, keeping all growth conditions constant except for the dopant. Since the electrical properties of rare earth doped InGaAs have been shown to be very sensitive to growth conditions such as growth rate and buffer layer, the same set of growth conditions were compared in order to avoid changes from growth conditions. The conducting substrate effect can be clearly seen in Figure 8.7a where 0.01% Gd doped InGaAs sees a change of slope in the electrical conductivity as it starts to more rapidly increase with temperature.

The most important difference between rare earth doping and Si doping is that Si doped InGaAs has a much steeper decrease in electrical conductivity with temperature than InGaAs doped with rare earths over a range of conductivities. In fact, with a low (0.01%) or high (1%) concentration of Gd, an increase in electrical conductivity with temperature is seen. This is likely due to a combination of the defect levels atomic Gd impurities contribute as well as a high density of nanoparticles thermally exciting carriers. No thermal excitation of carriers is seen in

Si doped InGaAs in this temperature regime. This leads to crossover points where the electrical conductivity of Gd doped InGaAs is lower than Si doped InGaAs at room temperature, but might be greater than Si doped InGaAs above 200-300˚C.

An inverse relationship between electrical conductivity and Seebeck coefficient is seen. However, the Seebeck coefficient increases with temperature whether the electrical conductivity increases or decreases with temperature. As discussed earlier in this chapter, Seebeck trends versus temperature track more closely with mobility versus temperature.

It is clear that the InP substrate becomes conducting at high temperature from Seebeck measurements as it plateaus and starts downward trending between 200-300˚C. The lower the electrical conductivity of the film, the more sensitive the measurement becomes to thermally excited carriers from the conducting substrate. Therefore, the apparent downward trends of the Seebeck coefficient at high temperature is not representative of the film itself, but shows that the contribution from the substrate is significant.

Looking at power factor data, the best rare earth dopant at room temperature is also the best high temperature rare earth for the samples grown in this study. Gd is seen as the most efficient rare earth, where Sc is the least efficient rare earth examined in this study.

Comparing with traditional dopants in Figure 8.7, it is seen that the highest room temperature power factors are not always the highest power factors at 200˚C. Since the electrical conductivity of Si doped InGaAs decreases faster with temperature than

Gd doped InGaAs, 1% and 0.5% Gd doped InGaAs crosses over to have improved power factors over $1x10^{16}$ and $1x10^{17}$ cm^{-3} Si doped InGaAs at high temperature, respectively. However, Gd has a larger power factor than $1x10^{18}$ cm^{-3} Si doped InGaAs at room temperature, but Si doping has a faster increasing Seebeck, which leads to a higher power factor above 100˚C. It is unclear whether this crossover is due to substrate conduction effects having more of an impact on Gd doped InGaAs or if this is an inherent property of the dopant type. This data can be compared to previous work incorporating Er in InGaAs[14] and InGaAlAs[26], where ZT>1 have been experimentally realized above 500˚C on sapphire substrates.

8.3.2.1 High Temperature Power Factor in the Literature

As seen in Figure 8.7, Er doped InGaAlAs[26] is shown to have a lower power factor than both the best Gd and Si concentration. This is likely due to the lower mobility and higher conduction band edge of InGaAlAs, showing that filtering of low energy electrons is not the most effective way to improve thermoelectric power factor in this material system.

Work on Er doped InGaAs on sapphire substrates has been shown to reach a ZT of 1.7 at 500˚C[14]. Comparing the highest performing sample from reference [14], Figure 8.7 shows that Er doped InGaAs has a lower power factor than Gd doped InGaAs at room temperature, but without the InP substrate corrupting the measurement at high temperature, a much steeper increase in power factor is realized since no roll off in Seebeck occurs. This leads one to expect that Gd doped InGaAs can achieve ZT>1.7 at comparable temperatures to Er doped InGaAs[14].

It is important to note that even with the InP substrate, Si doped InGaAs achieves similar power factors to the best performing Er doped InGaAs sample at high temperature. Since there is also substrate conduction affecting the measurement of Si doped InGaAs, it is likely that Si doping can achieve comparable or higher ZT than any of the rare earths studied.

It is clear that high power factors can be realized from doping with rare earths at high temperature in certain doping regimes. However, it is likely that Si doping can reach a higher peak power factor at high temperature. Furthermore, measurements on insulating substrates show that the Seebeck and power factor are steadily increasing, suggesting that these materials can be taken up to higher temperatures to reach $ZT>1.7$.

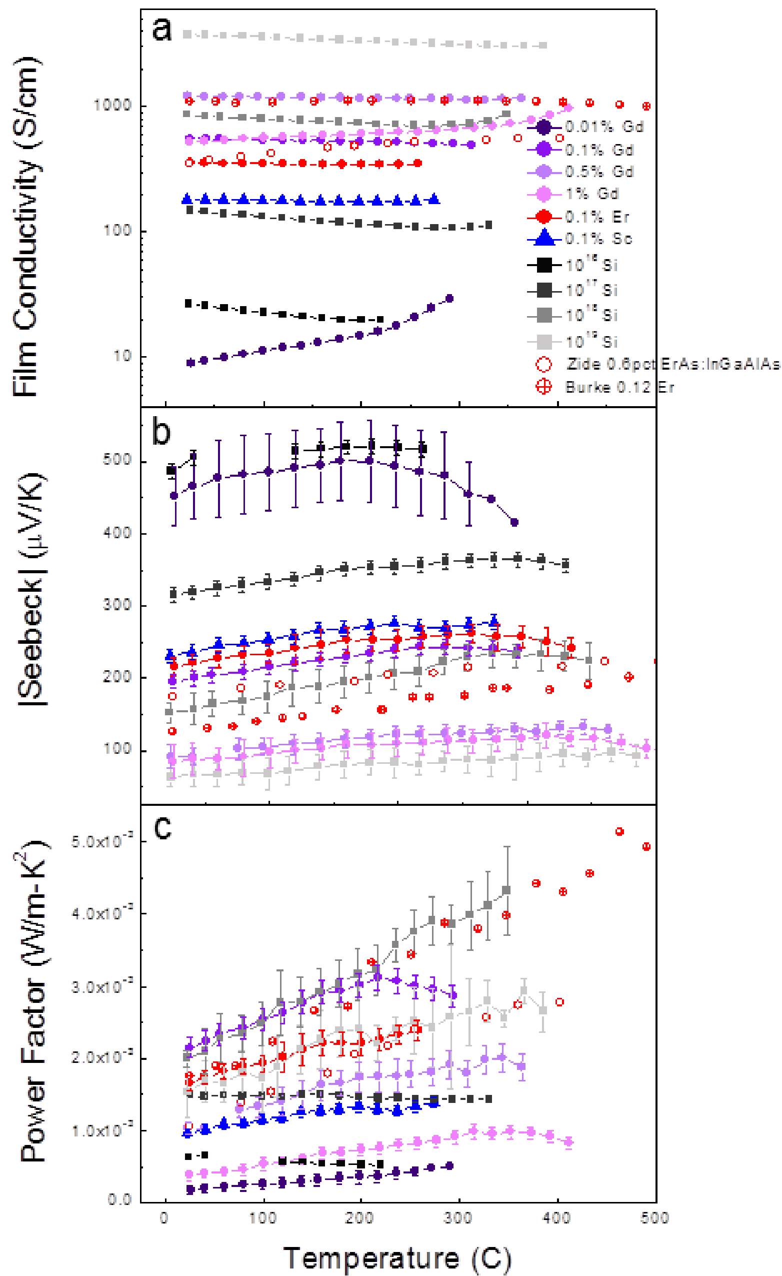

Figure 8.7 Temperature Dependent Power Factor

a) Electrical conductivity, b) Seebeck coefficient, and c) adjusted power factor for Gd, Si, Er and Sc doped InGaAs at high temperature to match the room temperature values on the room temperature measurement setup. The red open circles are taken from literature for Er doped InGaAlAs which reached a high power factor and ZT of 1.3 at 500˚C[26] and the red crossed circles are taken from Peter Burke's thesis for Er doped InGaAs which reached a ZT of 1.7 at 575˚C[14].

8.3.3 Optimizing ZT at High Temperature

Using the Seebeck versus conductivity trends as discussed in Chapter 6, we can create a theoretical landscape for the power factor, and therefore ZT, of Si doped InGaAs over a range of temperatures. Using the model described in Chapter 6, Figure 8.8 shows the Seebeck trends over a range of electrical conductivity. This data can be fit to a line so that the Seebeck can be predicted for any electrical conductivity. This allows the theoretical power factor to be calculated for any electrical conductivity as shown in Figure 8.9 over a range of temperatures. The solid line represents the calculated power factor assuming trends shown in the Seebeck versus conductivity plots, where the slope is proportional to the Boltzmann constant.

Over all temperatures explored, the peak power factor lies between 1,000-2,000 S/cm. It is seen that 0.1% Gd doped InGaAs approaches the peak power factor for Si doped InGaAs, but cannot surpass it. The highest ZT in this material system measured to date contained 0.12% Er doped InGaAs, suggesting that the 0.1% Gd doped InGaAs is already close to the optimal doping level. Comparing with the highest performing Er doped InGaAs transferred to a sapphire substrate, the power factor increases much faster with temperature, reaching the peak power factor for Si doped InGaAs at 200˚C. This is likely due to InP substrate conduction corrupting measurements of Si doped InGaAs at high temperature. On a more insulating substrate, both Gd and Si doped InGaAs are likely to have improved power factors at 200˚C. Now that we have established trends from the Si doped InGaAs baseline, we

can more carefully target higher power factors and ZT. It is important to note that even the highest performing Er sample has a low Er concentration, where no significant reduction in thermal conductivity is expected to be seen.

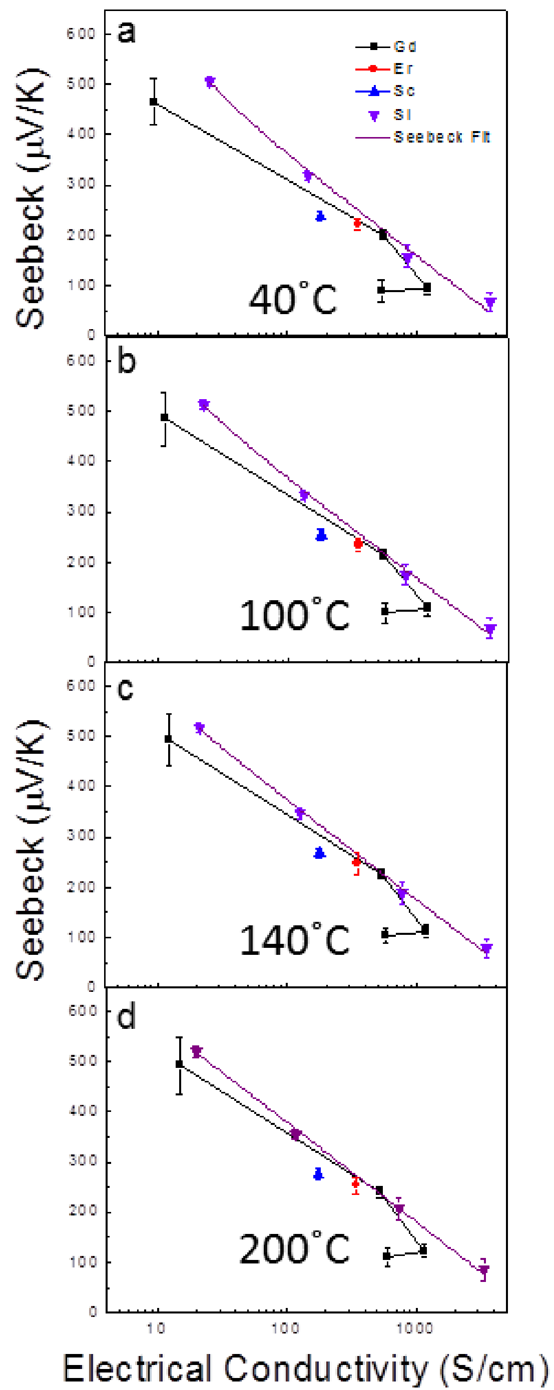

Figure 8.8 Seebeck Trends at Varying Temperature

Seebeck versus electrical conductivity for Gd, Si, Er and Sc doped InGaAs at a) 40˚C, b) 100˚C, c) 140˚C and d) 200˚C. The slope of Si doped InGaAs is k_b/e.

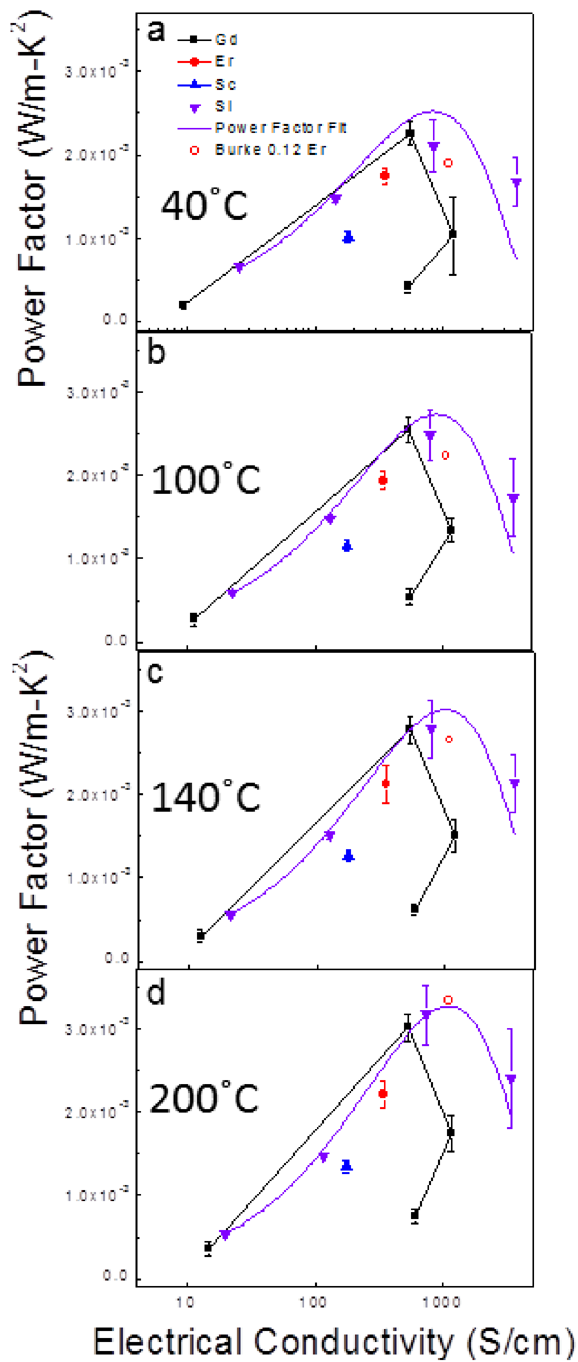

Figure 8.9 Power Factor Optimization Over Temperature

a) Power factor at 40˚C, b) 200˚C, c) 140˚C and d) 200˚C for Gd, Si, Er, and Sc doped InGaAs. The open red circles are previously studied Er doped InGaAs samples from Peter Burke's thesis[14]. The purple line is calculated from the fit of the Seebeck versus electrical conductivity plots.

Since ZT is optimized and it is seen that the rare earth doped material with the maximum power factor did not see significant decrease in thermal conductivity from nanoparticles, we can use the power factor model coupled with literature values of high temperature thermal conductivity of undoped InGaAs to predict the maximum ZT achievable with Si doped InGaAs and Gd doped InGaAs. Gd can reach a theoretical ZT of ~0.34 at 200˚C, while the power factor fit model can reach a ZT of ~0.36 at the same temperature. Therefore, no improvement in ZT from Gd is expected to be seen at the temperatures measured in this experiment.

However, a much greater ZT of 0.46 is achieved at that temperature in previously measured 0.12% Er doped InGaAs[14]. This is mostly due to a lower measured thermal conductivity with a difference of 0.8 W/m-K, consistent with ~20% error that can be expected in thermal conductivity measurements. This is an example of how error in thermal conductivity measurements can lead to large discrepancies in reported ZT.

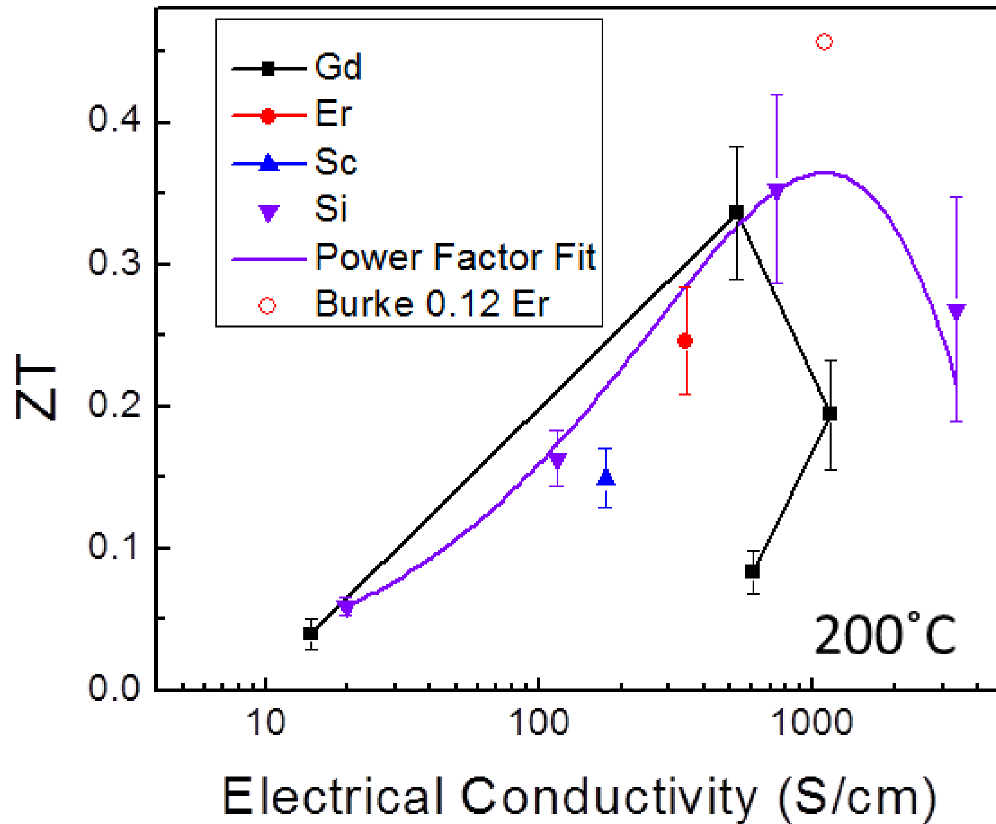

Figure 8.10 Optimized ZT at 200˚C
Using literature values for thermal conductivity of undoped InGaAs, ZT is calculated for rare earth and Si doped InGaAs at 200˚C. This is compared to Burke's thesis[14], which has a higher ZT due to a higher power factor and lower reported thermal conductivity.

When we use the optimum ZT trends for both Gd and Si fits, we can see how ZT changes with temperature and use an empirical fit to predict the ZT of InGaAs doped with either Si or Gd at high temperature. Using a power law fit to power factor coupled with an exponential decay to fit thermal conductivity data from literature[98], a trend with good agreement to experimental data is realized.

It is important to note the error associated with thermal conductivity measurements when reporting ZT values. Figure 8.11b shows that when the thermal conductivity is offset for the lowest[102] and highest[61] reported room temperature thermal conductivity measurements of undoped InGaAs, there is a very large spread in ZT. Therefore, it is important to note the error in reporting absolute values of ZT. Qualitative comparisons of controlled experiments are necessary for thermal conductivity measurements.

Projecting these ZT values to high temperature, we see that at 500˚C, a ZT of 1.5 can be reached for Gd doped InGaAs and a ZT of 1.8 can be reached for Si doped InGaAs. This is comparable to a ZT of 1.7 that was experimentally realized with Er doped InGaAs[14], but Si doping is predicted to have a larger ZT at this temperature. Furthermore, these estimates for Si and Gd doped InGaAs should be a lower bound on ZT, since they are based off of measurements that have been affected by substrate conduction. Increasing in temperature, we see that ZT in excess of 3 are predicted at 700˚C for both Gd and Si doped InGaAs. If InGaAs can be passivated so that it is stable at that temperature, great improvements in thermoelectric efficiency should be theoretically possible, paving the way for thermoelectrics to have new commercial applications.

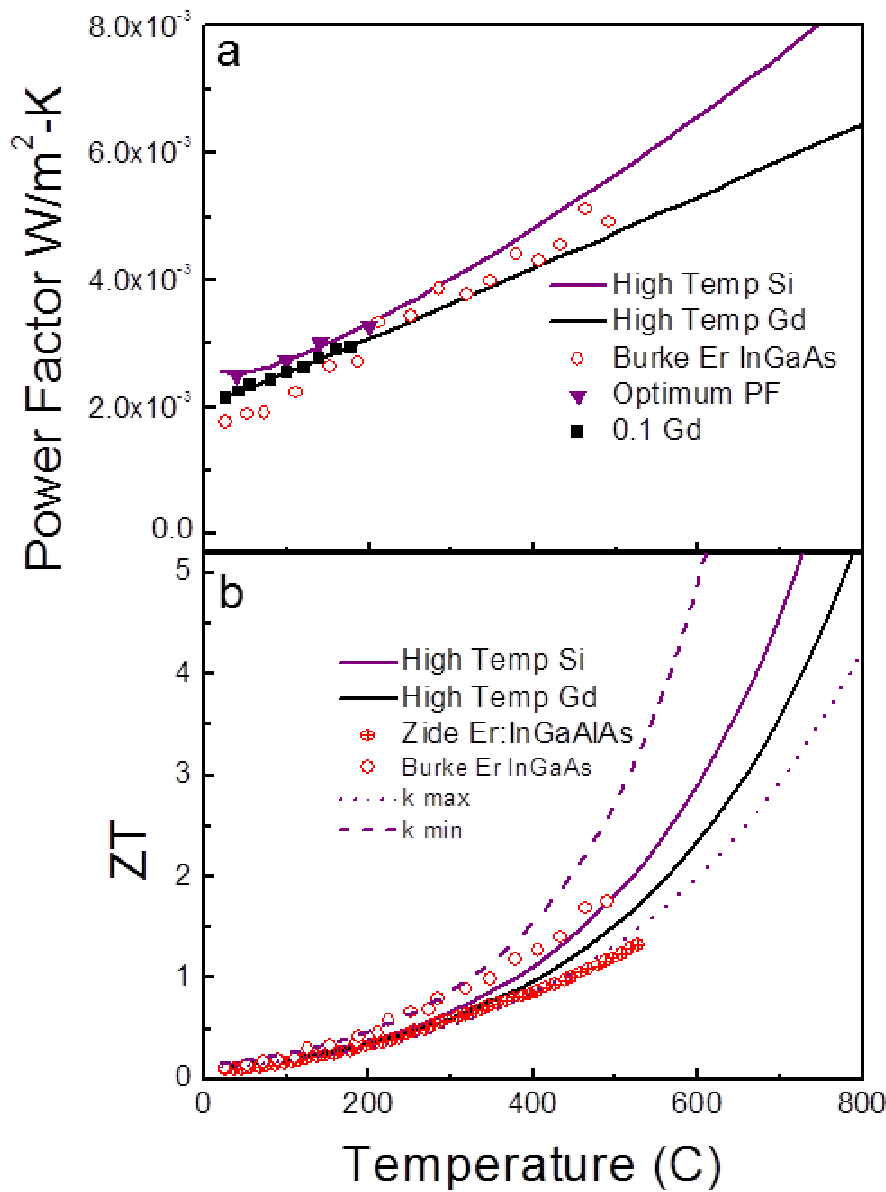

Figure 8.11 ZT Trends Extrapolated to High Temperature

a) Power factor trends and b) ZT trends extrapolated for Si doped InGaAs and 0.1% Gd doped InGaAs. The purple dashed line is the offset ZT for the lowest measured thermal conductivity[102] for undoped InGaAs at room temperature and the dotted line uses the highest reported thermal conductivity[61]. The red circles are comparisons to literature for Er doped InGaAs[14] and Er doped InGaAlAs[26].

8.4 Conclusions

To conclude this section, both high temperature and low temperature transport of rare earth and Si doped InGaAs was explored. It is seen that rare earth doping has different scattering mechanisms than traditionally doped InGaAs. Thermally excited carriers contribute to a more slow decrease, or even increase in electrical conductivity with temperature. Seebeck versus temperature trends track with mobility.

It is seen that Si doped InGaAs has the highest power factor at 200˚C compared to the other rare earths in this study. However, literature values for Er doped InGaAs on an insulating substrate show that higher power factors can be realized from substrate transfer. Using a model to optimize the power factor of Si doped InGaAs, the maximum power factor and ZT of Si doped InGaAs is seen to increase above maximum power factor of Gd doping at high temperature. It is possible that the peak power factor point of Gd doped InGaAs is not captured experimentally by the samples grown in this study, but comparison with a similar doping level of Er suggests that 0.1% Gd is close to the optimal doping level. Given that there is not as clear of a trend in rare earth doping, it is difficult to predict the true optimal doping without growing many samples. Extrapolating ZT trends to higher temperatures, a ZT in excess of 3 is predicted to occur above 700˚C. If this can be experimentally realized, it could open the door to new commercially viable thermoelectric applications.

Chapter 9

9 Conclusions and Future Work

9.1 Conclusions

In this work, different rare earths were explored as exotic dopants in InGaAs for thermoelectric applications and compared to traditionally, Si, doped InGaAs. Ultimately, it was seen that under these controlled growth conditions, the higher doping efficiency of Si in InGaAs led it to be a comparable thermoelectric to the best rare earth dopants for this set of growths and measurements. Si has the potential to achieve higher power factors than the rare earth doping explored as predicted from the Price analysis developed. Since the best rare earth doped InGaAs occurs at concentrations below a reduction in thermal conductivity is seen, no benefit over Si doped InGaAs is seen by including rare earths. Furthermore, the error associated with difficulty in the non-standard Seebeck and thermal conductivity measurements warrant qualitative comparisons of controlled experiments rather than quantitatively comparing to literature.

In Chapter 3, a baseline of the thermoelectric properties of Si doped InGaAs is developed as a traditional InGaAs system with no added nanostructures. The MBE growth of InGaAs is detailed and the room temperature thermoelectric properties are discussed to map out the optimal doping regime for this material system. A

maximum ZT~0.13 is achieved at room temperature for 10^{18} cm^{-3} Si concentration. Low temperature electrical transport illuminates different transport regimes at different temperatures and shows how adding Si impurities changes that transport.

In Chapter 4, doping with rare earths is introduced and Er and Sc are compared. A growth structure for minimizing parallel conduction and effects from depletion of less conductive films is optimized. Sc, a new dopant, shows similar thermoelectric properties as Er doping, with the difference being that Sc has a lower doping efficiency than Er. When alloying Er and Sc in InGaAs, a doping efficiency between the two individual rare earths is realized. This can be used to develop a model of carrier generation from particles based on strain nucleated particles leading to larger particles with less interfaces for thermally excited carriers to escape into the InGaAs matrix.

In Chapter 5, Gd is explored as another new rare earth dopant. GdAs is lattice matched to the InGaAs matrix and has the highest doping efficiency of all the rare earths explored, supporting the strain argument developed in the previous chapter. Overall, the higher doping efficiency of Gd leads it to have the highest power factor of all the rare earths studied. Since no significant decrease in thermal conductivity is seen in the optimal power factor range for rare earth doped InGaAs, Gd also has the highest room temperature ZT of all the rare earth dopants. Compared with Si doped InGaAs, the rare earths generally have lower ZT due to increased electron scattering from nanoparticles. Only the optimal power factor sample of Gd doped InGaAs had a comparable ZT to its Si doped counterpart.

Chapter 6 uses codoping of rare earth and traditional dopants to survey a wider range of the thermoelectrics space while using the minimal number of samples. Codoping with Si and Be allows independent control of nanoparticle concentration and electrical conductivity. However, it is seen that by introducing more RE-As nanoparticles at higher concentrations, the mobility of InGaAs is decreased so that the power factor cannot reach the same values as lower rare earth concentrations. The decrease in thermal conductivity from having more nanoparticles cannot overcome the decrease in power factor at high rare earth concentration, so Si doping on its own is seen as a more efficient thermoelectric dopant at room temperature.

Comparing to previous work in Chapter 7 on rare earths in InGaAs, Er doped InGaAs still has the highest reported power factor at room temperature, while Si is predicted to be able to achieve even higher power factors. Exploring thermoelectric properties around the peak Gd concentration could lead to further improvements in power factor.

The high temperature thermoelectric properties are discussed in Chapter 8. Thermal excitation of carriers is seen in Gd doped InGaAs, while no increase in carrier concentration is seen in Si doped InGaAs. The more Gd incorporated, the more the thermally excited carriers can overcome decreases in carrier mobility at high temperature. However, no significant enhancement in power factor is seen from doping with rare earths in the temperature regime studied. In fact, the power factor of Si doped InGaAs increases faster than Gd doped InGaAs, leading to the highest

measured power factor of Si doped InGaAs. This has a comparable high temperature power factor to the best reported Er doped InGaAs sample.

Using our model to determine power factor over a broader range of electrical conductivity, it is seen that Si doped InGaAs has the potential to have a higher power factor than Gd doped InGaAs at room temperature and high temperature. Si is identified as a better thermoelectric dopant for this set of growths and measurements. Overall, no improvement is seen from adding rare earths at either room temperature or high temperature. Extrapolating ZT out to higher temperatures shows that significant improvements in ZT can be gained with ZT>3 theoretically possible at 700˚C.

Overall, this thesis systematically explores different dopants in InGaAs for thermoelectrics. Much research has been done in the past showing that doping InGaAs with rare earths improves ZT, but this work includes a control experiment that proves Si doped InGaAs is indeed a better thermoelectric for this set of growths and measurements. Thermal conductivity suppression from rare earth doping was not able to compensate for the low power factors for the high doping concentration, giving no advantage to rare earth doping over Si. Furthermore, the higher doping efficiency and higher crystal quality of Si doping achieves higher electrical conductivities at a given dopant concentration compared to rare earth doping, leading to higher power factor trends for this set of growths and measurements. Using these thin film studies by MBE is a controlled way to illuminate how nanostructuring can or cannot improve thermoelectric properties.

9.2 Future Work

Although much work has already been done on this material system, there are several more steps to be taken to optimize the ZT of InGaAs.

9.2.1 High Temperature Measurements

First and foremost, getting reliable high temperature measurements to experimentally verify ZT predictions at high temperatures would be prudent. Previous work at high temperature has not seen a decrease in thermoelectric properties up to 850K, so finding the maximum operating temperature would allow one to properly tailor the electrical conductivity to the maximum power factor point. In order to quantitatively compare ZT, a more accurate thin film thermal conductivity measurement must be developed. Developing a working AC Seebeck measurement at high temperature will lead to much more accurate measurements, particularly at high temperature, where it becomes more difficult to stabilize two individual copper heaters.

In order to accomplish this, a reliable method to transfer InGaAs films onto an insulating substrate much be developed that is stable at high temperatures. Some work has been done to use flip chip bonding to suspend films, but a more repeatable process needs to be developed.

Furthermore, exploring more finely spaced Si doping levels at high temperature will help verify the model developed in Chapter 6, to explore what power factors can be achieved at high temperature in InGaAs.

9.2.2 Growth Rate Effect

Much work has been done on doping InGaAs with rare earths and there is a lot of spread in the data gathered. It has been shown that the thermoelectric properties of rare earth doped InGaAs are very sensitive to growth structure and growth parameters. Previous work has shown how growth temperature can change the solubility limit of Er in InGaAs, affecting the thermoelectric properties of otherwise identical structures[47]. A study to understand how changing growth rate affects rare earth solubility and thermoelectric properties would be prudent. It is typically seen that the peak ZT occurs near the onset of nanoparticle formation. If the growth rate can be increased to suppress the formation of RE-As nanoparticles, it might be possible to reach a higher doping efficiency, which has been shown to directly correlate to ZT.

9.2.3 Si as a Dopant in InGaAs

Si is seen as a more efficient dopant over most of the carrier concentration regime, except for the peak power factor seen in 0.1% Gd doped InGaAs. Si doping is a good control dopant because in the carrier concentration range explored, it incorporates substitutionally and does not form new phases, such as the rocksalt RE-As phase formed from incorporating rare earths. However, Si is known to be an amphoteric dopant at high carrier concentrations as it will also sit on As sites acting as an electron acceptor as well as sitting on group III sites acting as an electron donor[71]. It is possible that with high enough Si incorporation ($>10^{20}$ cm^{-3}), the Si diamond phase precipitates out similar to the way that the RE-As rocksalt phase

precipitates in InGaAs. It would be interesting to compare these multiphase systems. The incorporation of Si clusters in InGaAs would be different than RE-As clusters in a couple of ways. The Si clusters would be semiconducting instead of semimetallic and the single element Si clusters could lead to stacking faults when the ternary InGaAs covers the Si clusters. This could potentially lead to grain-like features to further reduce the thermal conductivity by introducing micron sized features in addition to nanoscale features, using an all-scale hierarchy to achieve very low thermal conductivity as done in high ZT PbTe[5].

10 Appendix

A.1 Substrate Removal for High Temperature Measurements

Due to the conducting InP substrate corrupting high temperature electrical measurements as discussed in Chapter 7, it is necessary to develop a way to transfer InGaAs films to more insulating substrates for more accurate high temperature measurements. Oxide bonding of InGaAs films has shown that measurements up to 850K can be made on InGaAs films[26, 107]. However, this requires films to be atomically flat with features less than 5nm. This is not feasible for MBE grown films since oval defects add roughness on a much larger scale to the film. In order to use this technique, oval defects must be etched away, which violates the rule for conductivity measurements of having a continuous film with no holes.

Flip chip bonding using Au/Au thermocompression shows promise as a way to successfully transfer MBE grown films to sapphire substrates, which are insulating up to very high temperatures[108]. Since Au is a very soft, ductile material, particularly at high temperature, surface roughness constraints as well as thermal mismatch constraints are significantly reduced. Preliminary work has shown that InGaAs films can be successfully bonded to sapphire with thick, electroplated Au contacts as shown in Figure 10.1. Au not only serves as the bonding medium, but also as the electrical contact.

The key to a successful bond is porous, easily compressible Au with a clean surface for strong bonding. Using an O_2 plasma cleaning process, the Au surfaces can be successfully bonded in a graphite chuck at 300˚C after the film is aligned to the new substrate in the flip chip bonder.

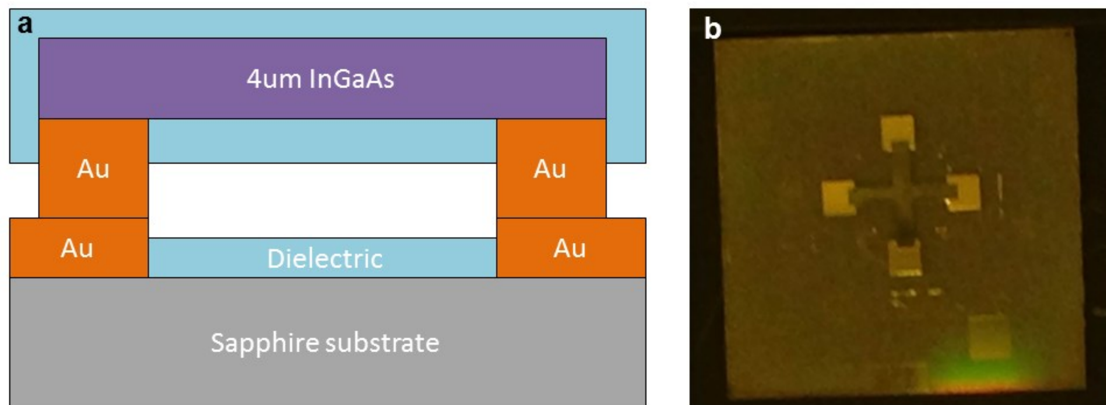

Figure 10.1 Au Bonding of InGaAs Films to Insulating Substrate
a) Schematic of a flip chip bonded thin film for high temperature electrical measurements on sapphire and b) a picture of a suspended thin film from this process.

The main problem with this technique so far is its high propensity to crack. Large InGaAs structures are not strong enough to be suspended without cracking, so moving to smaller device structures shows promise as a way to make repeatable suspended InGaAs films with stability up to high temperature. Details of the process are shown below.

Process Flow for InGaAs Film Transfer to Sapphire Substrate
Cleave and dice samples
Define mesas in InGaAs with H_3PO_4:H_2O_2:H_2O 8:1:1
Passivate InGaAs with SiN_x/SiO_2 200/100nm
Litho Au Contact openings on InGaAs and deposit TiWN/Au
Deposit Au seed layer on entire InGaAs sample
Deposit Ti/Au on sapphire
Electroplate Au on InGaAs and sapphire
Lithographically etch Au contacts on InGaAs and sapphire with KI solution.
Deposit SiO_2 support on sapphire
Etch through SiO_2 above Au contacts(BHF wet or CHF_4 dry etch)
Etch bonding valleys in SiO_2 on sapphire(CHF_4 dry etch)
Clean samples(solvent clean and O_2 plasma clean)
Flip Chip bond
Graphite Chuck Bonding Anneal at 300˚C for 1 hour
Substrate removal with HCl
Passivate InGaAs with SiN_x/SiO_2
Etch through passivation to Au contacts(BHF wet or CHF_4 dry etch)

B.1 Defect Levels From Temperature Dependent Hall

GdAs, along with other rare earths, are predicted to contribute thermally excited carriers from atomic donor impurities as well as from particles lying close to the conduction band edge of InGaAs. Temperature dependent Hall measurements are a good way to extract activation energies from impurities. This is more complicated in the rare earth doped InGaAs system due to the different types of impurities that rare earths form in InGaAs.

As can be seen in Figure 10.2, there are three temperature regimes which correspond to different activation energies. However, none of these regimes follows a perfect trend, probably due to the formation of a number of closely spaced impurity levels. Further characterization, such as deep level transient spectroscopy (DLTS)[109], can be used to more precisely detect different impurity levels in InGaAs.

It can be seen that at low temperatures, a thermal activation energy of ~3meV is seen with a very poor fit, consistent with low activation energies seen at low temperature in Section 8.2. Above room temperature, an activation energy of ~15meV is seen that can be estimated from levels from GdAs particles as well as atomic impurities from Gd. Above 500K, a thermal activation energy of ~39meV is seen, likely due to thermal activation of carriers from the InP substrate. Measuring InGaAs on an insulating substrate at high temperature will give more information about the film itself, without contamination from a conductive substrate.

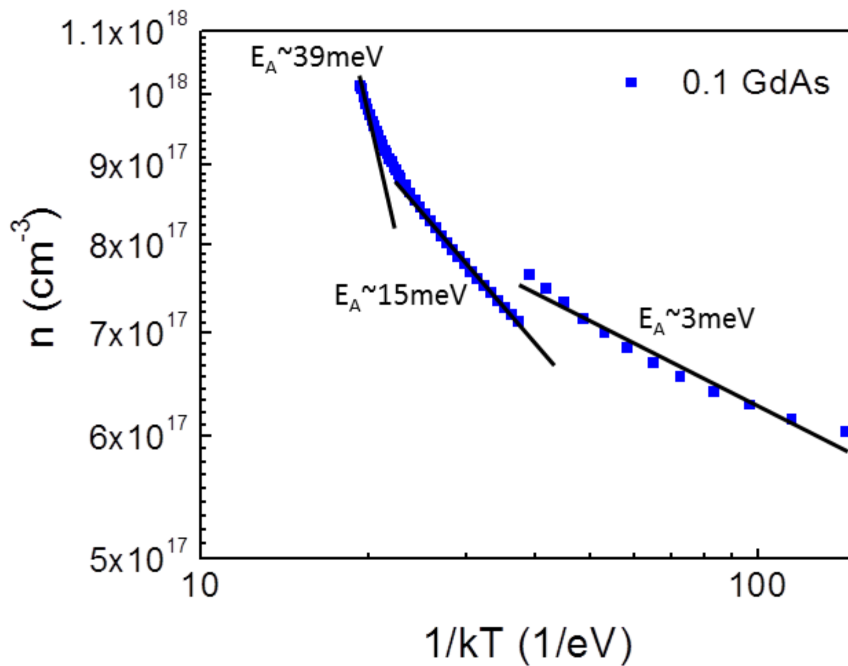

Figure 10.2 Many Levels from Gd doped InGaAs

Temperature dependent Hall for 0.1% Gd doped InGaAs. An "activation energy" can be extracted from the slopes of the exponential fits in different temperature regimes: low temperature (100-300K), medium temperature (310-500K) and high temperature (510-600K). This corresponds to different defects being thermally activated in the InGaAs on InP system.

In order to separate the contribution from atomic impurities and particles, more controlled structures, such as schottky barriers[33] with GdAs and diodes with only atomic Gd can be used to correlate electronic levels to different types of impurities in InGaAs.

C.1 Particle Detection From Low Temperature Photoluminesence

TEM is typically the characterization method of choice to detect RE-As nanoparticles in III-V semiconductors due to its high resolution to differentiate the high Z in rare earth based particles[29, 79]. However, TEM falls short in that only small volumes of material can be surveyed. Furthermore, the difficulty in producing high quality TEM samples that can resolve ErAs nanoparticles makes particle detection in individual samples impractical. Furthermore, elements that do not provide enough Z contrast are not practical for TEM characterization.

Photoluminesence could serve as a quick tool to detect RE-As nanoparticles. The short carrier lifetimes of ErAs particles has been shown to quench photoluminescence in GaAs[110]. Assuming that atomic Er impurities simply act as donors in InGaAs and do not exhibit the same quenching properties, low temperature photoluminescence can be used as a tool to detect the presence of RE-As (ErAs) in InGaAs.

Figure 10.3 shows a high photoluminescence of unintentionally doped InGaAs that is continually decreased as more Er is incorporated. At 0.1% ErAs incorporation, the previously reported solubility limit in InGaAs from TEM experiments[42], the photoluminescence signal is quenched, signaling a critical density of ErAs nanoparticles as recombination centers in InGaAs.

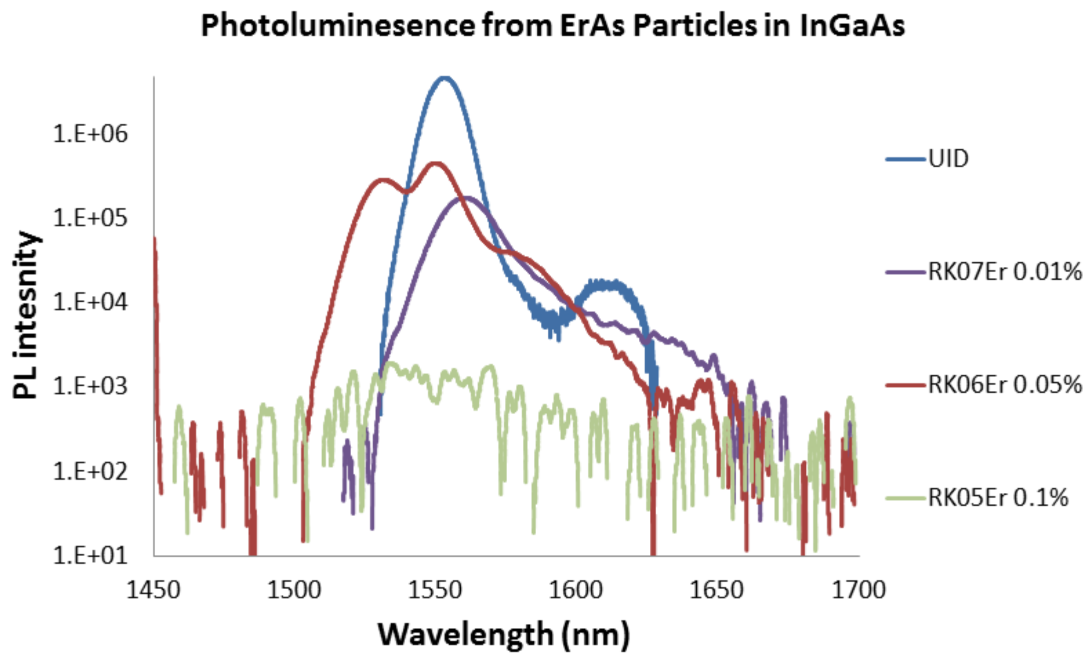

Figure 10.3 Photoluminesence to Detect ErAs Nanoparticles
Quenching of pholotuminesence at 10K due to the presence of ErAs nanoparticles in InGaAs.

References

1. **Energy Flow** [https://flowcharts.llnl.gov/]

2. **Voyager: The Interstellar Mission** [voyager.jpl.nasa.gov/mission/index.html]

3. Vining CB: **An inconvenient truth about thermoelectrics.** *Nat Mater* 2009, **8**:83–5.

4. Solyom J: *Fundamentals of the Physics of Solids, Vol 2 Electronic Properties*. Berlin Heidelberg: Springer-Verlag; 2009.

5. Biswas K, He J, Blum ID, Wu C-I, Hogan TP, Seidman DN, Dravid VP, Kanatzidis MG: **High-performance bulk thermoelectrics with all-scale hierarchical architectures**. *Nature* 2012, **489**:414–418.

6. Dresselhaus MS, Chen G, Tang MY, Yang R, Lee H, Wang D, Ren Z, Fleurial J-P, Gogna P: **New Directions for Low-Dimensional Thermoelectric Materials**. *Adv Mater* 2007, **19**:1043–1053.

7. Minnich AJ, Dresselhaus MS, Ren ZF, Chen G: **Bulk nanostructured thermoelectric materials: current research and future prospects**. *Energy Environ Sci* 2009, **2**:466–479.

8. Snyder GJ, Toberer ES: **Complex thermoelectric materials.** *Nat Mater* 2008, **7**:105–14.

9. Heremans JP, Dresselhaus MS, Bell LE, Morelli DT: **When thermoelectrics reached the nanoscale**. *Nat Nanotechnol* 2013, **8**:471–3.

10. **Overview of the Advanced Combustion Engine R & D** [http://www1.eere.energy.gov/vehiclesandfuels/pdfs/merit_review_2012/plenary/vtpn05_ace_singh_2012_o.pdf]

11. Yang J: **Develop Thermoelectric Technology for Automotive Waste Heat Recovery**. In *Dir Engine-Efficiency Emiss Res Conf*; 2009.

12. Liang X, Wang X, Shu G, Wei H, Tian H, Wang X: **A review and selection of engine waste heat recovery technologies using analytic hierarchy process and grey relational analysis**. *Int J Energy Res* 2014.

13. Zhao LD, Wu HJ, Hao SQ, Wu CI, Zhou XY, Biswas K, He JQ, Hogan TP, Uher C, Wolverton C, Dravid VP, Kanatzidis MG: **All-scale hierarchical**

thermoelectrics: MgTe in PbTe facilitates valence band convergence and suppresses bipolar thermal transport for high performance. *Energy Environ Sci* 2013, **6**:3346.

14. Burke PG: **Molecular Beam Epitaxy Growth of Rare Earth Elements in III-V Semiconductors for Thermoelectrics**. University of California Santa Barbara; 2013(December).

15. Hicks LD, Dresselhaus MS: **Effect of quantum-well structures on the thermoelectric figure of merit**. *Phys Rev B* 1993, **47**:727–731.

16. Hicks LD, Dresselhaus MS: **Thermoelectric figure of merit of a one-dimensional conductor**. *Phys Rev B* 1993, **47**:631–634.

17. Dresselhaus MS, Dresselhaus G, Sun X, Zhang Z, Cronin SB, Koga T, Ying JY, Chen G: **The Promise of Low-Dimensional Thermoelectric Materials**. *Microscale Thermophys Eng* 1999:89–100.

18. Cutler M, Mott NF: **Observation of Anderson Localization in an Electron Gas**. *Phys Rev Lett* 1969, **181**:1336–1340.

19. Heremans JP, Jovovic V, Toberer ES, Saramat A, Kurosaki K, Charoenphakdee A, Yamanaka S, Snyder GJ: **Enhancement of thermoelectric efficiency in PbTe by distortion of the electronic density of states.** *Science* 2008, **321**:554–557.

20. Zhang Z, Ying JY, Dresselhaus MS: **Bismuth quantum-wire arrays fabricated by a vacuum melting and pressure injection process**. *J Mater Res* 1998, **13**:1745–1748.

21. Tian Y, Sakr MR, Kinder JM, Liang D, MacDonald MJ, Qiu RLJ, Gao H-J, Gao XPA: **One-Dimensional Quantum Confinement Effect Modulated Thermoelectric Properties in InAs Nanowires**. *Nano Lett* 2012, **12**:6492–6497.

22. Wu PM, Gooth J, Zianni X, Svensson SF, Gluschke JG, Dick KA, Thelander C, Nielsch K, Linke H: **Large thermoelectric power factor enhancement observed in InAs nanowires.** *Nano Lett* 2013, **13**:4080–6.

23. Biswas K, He J, Zhang Q, Wang G, Uher C, Dravid VP, Kanatzidis MG: **Strained endotaxial nanostructures with high thermoelectric figure of merit.** *Nat Chem* 2011, **3**:160–6.

24. Zide JMO, Vashaee D, Bian ZX, Zeng G, Bowers JE, Shakouri A, Gossard AC: **Demonstration of electron filtering to increase the Seebeck coefficient in $In_{0.53}Ga_{0.47}As/In_{0.53}Ga_{0.28}Al_{0.19}As$ superlattices**. *Phys Rev B* 2006, **74**:205335.

25. Kim W, Zide J, Gossard A, Klenov D, Stemmer S, Shakouri A, Majumdar A: **Thermal Conductivity Reduction and Thermoelectric Figure of Merit Increase**

by Embedding Nanoparticles in Crystalline Semiconductors. *Phys Rev Lett* 2006, **96**:045901–1.

26. Zide JMO, Bahk J-H, Singh R, Zebarjadi M, Zeng G, Lu H, Feser JP, Xu D, Singer SL, Bian ZX, Majumdar A, Bowers JE, Shakouri A, Gossard AC: **High efficiency semimetal/semiconductor nanocomposite thermoelectric materials**. *J Appl Phys* 2010, **108**:123702.

27. Palmstrøm CJ, Sands T, Harbison JP, Keramidas VG, Tabatabaie N, Cheeks TL, Ramesh R, Silberberg Y: **Stable and epitaxial metal/III-V semiconductor heterostructures**. *Mater Sci Reports* 1990, **5**:99–170.

28. Hanson MP, Bank SR, Zide JMO, Zimmerman JD, Gossard AC: **Controlling electronic properties of epitaxial nanocomposites of dissimilar materials**. *J Cryst Growth* 2007, **301-302**:4–9.

29. Klenov DO, Driscoll DC, Gossard AC, Stemmer S: **Scanning transmission electron microscopy of ErAs nanoparticles embedded in epitaxial In[0.53]Ga[0.47]As layers**. *Appl Phys Lett* 2005, **86**:111912.

30. Klenov DO, Zide JM, Zimmerman JD, Gossard AC, Stemmer S: **Interface atomic structure of epitaxial ErAs layers on (001) $In_{0.53}Ga_{0.47}As$ and GaAs**. *Appl Phys Lett* 2005, **86**:241901.

31. Palmstrøm CJ, Cheeks TL, Gilchrist HL, Zhu JG, Carter CB, Wilkens BJ, Martin R: **Effect of orientation on the Schottky barrier height of thermodynamically stable epitaxial metal/GaAs structures**. *J Vac Sci Technol A Vacuum, Surfaces, Film* 1992, **10**:1946–1953.

32. Van de Walle CG: **Bandgap Heaven in Color**.

33. Zimmerman JD, Brown ER, Gossard AC: **Tunable all epitaxial semimetal-semiconductor Schottky diode system: ErAs on InAlGaAs**. *J Vac Sci Technol B Microelectron Nanom Struct* 2005, **23**:1929–1935.

34. Brillson LJ, Slade ML, Viturro RE, Kelly MK, Tache N, Margaritondo G, Woodall JM, Kirchner PD, Pettit GD, Wright SL: **Absence of Fermi level pinning at metal-$In_xGa_{1-x}As(100)$ interfaces**. *Appl Phys Lett* 1986, **48**:1458.

35. Allen SJ, Tabatabaie N, Palmstrøm CJ, Mounier S, Hull GW, Sands T, DeRosa F, Gilchrist HL, Garrison KC: **Magneto-Transport in Ultrathin ErAs Epitaxial Layers Buried in GaAs**. *Surf Sci* 1990, **228**:13–15.

36. Kawasaki JK, Timm R, Delaney KT, Lundgren E, Mikkelsen A, Palmstrøm CJ: **Local Density of States and Interface Effects in Semimetallic ErAs Nanoparticles Embedded in GaAs**. *Phys Rev Lett* 2011, **107**:036806.

37. Schultz BD, Palmstrøm CJ: **Embedded assembly mechanism of stable metal nanocrystals on semiconductor surfaces**. *Phys Rev B* 2006, **73**:241407.

38. Zide JM, Klenov DO, Stemmer S, Gossard AC, Zeng G, Bowers JE, Vashaee D, Shakouri A: **Thermoelectric power factor in semiconductors with buried epitaxial semimetallic nanoparticles**. *Appl Phys Lett* 2005, **87**:112102.

39. Zide JMO, Zeng G, Bahk JH, Kim W, Singer SL, Vashaee D, Bian ZX, Singh R, Bowers JE, Majumdar A, Shakouri A, Gossard AC: **Nanocomposites of Semimetallic ErAs Nanoparticles Epitaxially Embedded within InGaAlAs-based Semiconductors for Thermoelectric Materials**. In *2006 Int Conf Thermoelectr*. *Volume 00*; 2006:280.

40. Lu H, Burke PG, Gossard AC, Zeng G, Ramu AT, Bahk J-H, Bowers JE: **Semimetal/Semiconductor Nanocomposites for Thermoelectrics**. *Adv Mater* 2011, **23**(XX):1–7.

41. Deputier S, Guerin R, Ballini Y, A. G: **Solid state phase equilibria in the Er-Ga-As system**. *J Alloys Compd* 1993, **202**:95–100.

42. Burke PG, Lu H, Rudawski NG, Stemmer S, Gossard AC, Bahk J-H, Bowers JE: **Electrical properties of Er-doped $In_{0.53}Ga_{0.47}As$**. *J Vac Sci Technol B Microelectron Nanom Struct* 2011, **29**:03C117.

43. Burke PG, Ismer L, Lu H, Frantz E, Janotti A, Van de Walle CG, Bowers JE, Gossard AC: **Electrically active Er doping in InAs, $In_{0.53}Ga_{0.47}As$, and GaAs**. *Appl Phys Lett* 2012, **101**:232103.

44. Cassels LE, Buehl TE, Burke PG, Palmstrøm CJ, Gossard AC, Pernot G, Shakouri A, Haughn CR, Doty MF, Zide JMO: **Growth and characterization of TbAs:GaAs nanocomposites**. *J Vac Sci Technol B Microelectron Nanom Struct* 2011, **29**:03C114.

45. Clinger LE, Pernot G, Buehl TE, Burke PG, Gossard AC, Palmstrøm CJ, Shakouri A, Zide JMO: **Thermoelectric properties of epitaxial TbAs : InGaAs nanocomposites**. *J Appl Phys* 2012, **111**.

46. Selezneva E, Clinger LE, Ramu AT, Pernot G, Buehl TE, Favaloro T, Bahk J-H, Bian Z, Bowers JE, Zide JMO, Shakouri A: **Thermoelectric Transport in InGaAs with High Concentration of Rare-Earth TbAs Embedded Nanoparticles**. *J Electron Mater* 2012, **41**:1820–1825.

47. Burke PG, Buehl TE, Gilles P, Lu H, Shakouri A, Palmstrøm CJ, Bowers JE, Gossard AC: **Controlling n-Type Carrier Density from Er Doping of InGaAs with MBE Growth Temperature**. *J Electron Mater* 2012, **41**:948–953.

48. Martin J, Tritt T, Uher C: **High temperature Seebeck coefficient metrology**. *J Appl Phys* 2010, **108**:121101.

49. Sztein A: **Advancements in III-Nitride Materials for Thermoelectric Applications**. University of California Santa Barbara; 2013(December).

50. Shi L, Li D, Yu C, Jang W, Kim D, Yao Z, Kim P, Majumdar A: **Measuring Thermal and Thermoelectric Properties of One-Dimensional Nanostructures Using a Microfabricated Device**. *J Heat Transfer* 2003, **125**:881.

51. Curtin BM: **Improvement and Integration of Silicon Nanowires for Thermoelectric Applications**. University of California Santa Barbara; 2014(March).

52. Cahill DG: **Thermal conductivity measurement from 30 to 750K: the 3ω method**. *Rev Sci Instrum* 1990, **61**:802–808.

53. Cahill DG, Katiyar M, Abelson JR: **Thermal conductivity of a-Si:H thin films**. *Phys Rev B* 1994, **50**:6077–6081.

54. Cahill DG: **Analysis of heat flow in layered structures for time-domain thermoreflectance**. *Rev Sci Instrum* 2004, **75**:5119–5122.

55. Koh YK, Singer SL, Kim W, Zide JMO, Lu H, Cahill DG, Majumdar A, Gossard AC: **Comparison of the 3ω method and time-domain thermoreflectance for measurements of the cross-plane thermal conductivity of epitaxial semiconductors**. *J Appl Phys* 2009, **105**:054303.

56. Borca-Tasciuc T, Kumar AR, Chen G: **Data reduction in 3ω method for thin-film thermal conductivity determination**. *Rev Sci Instrum* 2001, **72**:2139–2147.

57. Kim WC: **Thermal Transport in Nanostructured Materials**. University of California, Berkeley; 2005.

58. Feser JP: **Scalable Routes to Efficient Thermoelectric Materials**. University of California, Berkeley; 2010.

59. Koh YK: **Heat Transport by Phonons in Crystalline Materials and Nanostructures**. University of Illinois at Urbana-Champaign; 2010.

60. Wang Y, Park JY, Koh YK, Cahill DG: **Thermoreflectance of metal transducers for time-domain thermoreflectance**. *J Appl Phys* 2010, **108**:043507.

61. Hockings EF, Kudman I, Seidel TE, Schmelz CM, Steigmeier EF: **Thermal and Electrical Transport in InAsGaAs Alloys**. *J Appl Phys* 1966, **37**:2879.

62. Foxon CT, Joyce BA: **Surface Processes Controlling the Growth of $Ga_xIn_{1-x}As$ and $Ga_xIn_{1-x}P$ Alloy Films by MBE**. *J Cryst Growth* 1978, **44**:75–83.

63. Averbeck R, Riechert H, Schlotterer H: **Oxide desorption from InP under stabilizing pressures of P2 or As4**. *Appl Phys Lett* 1991, **59**:1732–1734.

64. Klenov DO, Zide JMO: **Structure of the InAlAs/InP interface by atomically resolved energy dispersive spectroscopy**. *Appl Phys Lett* 2011, **99**:141904.

65. Tersoff J: **Schottky barriers and semiconductor band structures**. *Phys Rev B* 1985, **32**:6968–6971.

66. Mead CA, Spitzer WG: **Fermi Level Position at Metal-Semiconductor Interfaces**. *Phys Rev* 1964, **134**:A713–A716.

67. Bhargava S, Blank H-R, Narayanamurti V, Kroemer H: **Fermi-level pinning position at the Au–InAs interface determined using ballistic electron emission microscopy**. *Appl Phys Lett* 1997, **70**:759–761.

68. Millunchick JM, Riposan A, Dall BJ, Pearson C, Orr BG: **Surface reconstructions of InGaAs alloys**. *Surf Sci* 2004, **550**:1–7.

69. Skromme BJ, Bose SS, Lee B, Low TS, Lepkowski TR, DeJule RY, Stillman GE, Hwang JCM: **Characterization of high purity Si doped molecular beam epitaxial GaAs**. *J Appl Phys* 1985, **58**:4685–4702.

70. Briones F, Collins DM: **Low Temperature Photoluminescence of Lightly Si-doped and Undoped MBE GaAs**. *J Electron Mater* 1982, **11**:847–866.

71. Neave JH, Dobson PJ, Harris JJ, Dawson P, Joyce BA: **Silicon doping of MBE-grown GaAs films**. *Appl Phys A Solids Surfaces* 1983, **32**:195–200.

72. Schubert EF: *Doping in III-V Semiconductors*. New York: Cambridge University Press; 1993.

73. Sze SM: *Semiconductor Devices: Physics and Technology*. 2nd edition. John Wiley & sons, Inc.; 1985.

74. Goldsmid HJ: **Review of Thermoelectric Materials**. In *Introd to Thermoelectr*; 2010.

75. Chen G: **Nanoscale Heat Transfer and Nanostructured Thermoelectrics**. *IEEE Trans Components Packag Technol* 2006, **29**:238–246.

76. Palmstrøm CJ, Mounier S, Finstad TG, Miceli PF: **Lattice-matched $Sc_{1-x}Er_xAs$/GaAs heterostructures: A demonstration of new systems for fabricating lattice-matched metallic compounds to semiconductors**. *Appl Phys Lett* 1990, **56**:382–384.

77. Palmstrøm CJ, Tabatabaie N, Allen SJ: **Epitaxial growth of ErAs on (100)GaAs**. *Appl Phys Lett* 1988, **53**:2608–2610.

78. Gschneidner KA, Calderwood FW: **The As-Sc (Arsenic-Scandium)**. *Bull Alloy Phase Diagrams* 1986, **7**:348–349.

79. Klenov DO, Zide JMO, LeBeau JM, Gossard AC, Stemmer S: **Ordering of ErAs nanoparticles embedded in epitaxial InGaAs layers**. *Appl Phys Lett* 2007, **90**:121917.

80. Kawasaki JK, Timm R, Buehl TE, Lundgren E, Mikkelsen A, Gossard AC, Palmstrøm CJ: **Cross-sectional scanning tunneling microscopy and spectroscopy of semimetallic ErAs nanostructures embedded in GaAs**. *J Vac Sci Technol B Microelectron Nanom Struct* 2011, **29**:03C104.

81. Kawasaki JK, Schultz BD, Palmstrøm CJ: **Size effects on the electronic structure of ErSb nanoparticles embedded in the GaSb(001) surface**. *Phys Rev B* 2013, **87**:035419.

82. Kawasaki JK, Schultz BD, Lu H, Gossard AC, Palmstrøm CJ: **Surface-Mediated Tunable Self-Assembly of Single Crystal Semimetallic ErSb/GaSb Nanocomposite Structures**. *Nano Lett* 2013, **13**:2895–901.

83. Kadow C, Johnson JA, Kolstad K, Ibbetson JP, Gossard AC: **Growth and microstructure of self-assembled ErAs islands in GaAs**. *J Vac Sci Technol B Microelectron Nanom Struct* 2000, **18**:2197.

84. Perea DE, Allen JE, May SJ, Wessels BW, Seidman DN, Lauhon LJ: **Three-dimensional nanoscale composition mapping of semiconductor nanowires**. *Nano Lett* 2006, **6**:181–5.

85. Blavette D, Bostel A, Sarrau JM, Deconihout B, Menand A: **An atom probe for three-dimensional tomography**. *Nature* 1993, **363**:432–435.

86. Thompson K, Lawrence D, Larson DJ, Olson JD, Kelly TF, Gorman B: **In situ site-specific specimen preparation for atom probe tomography**. *Ultramicroscopy* 2007, **107**:131–139.

87. Bas P, Bostel A, Deconihout B, Blavette D: **A general protocol for the reconstruction of 3D atom probe data**. *Appl Surf Sci* 1995, **87/88**:298–304.

88. Miller MK, Kenik EA: **Atom probe tomography: a technique for nanoscale characterization**. *Microsc Microanal* 2004, **10**:336–41.

89. Stephenson LT, Moody MP, Liddicoat P V, Ringer SP: **New techniques for the analysis of fine-scaled clustering phenomena within atom probe tomography (APT) data.** *Microsc Microanal* 2007, **13**:448–63.

90. Koltun R, Hall JL, Mates TE, Bowers JE, Schultz BD, Palmstrøm CJ: **Thermoelectric properties of single crystal $Sc_{1-x}Er_xAs$: InGaAs nanocomposites**. *J Vac Sci Technol B Microelectron Nanom Struct* 2013, **31**:041401.

91. Schultz BD: **In-Situ Surface, Chemical, and Electrical Characterization of the Interfaces Between Ferromagnetic Metals and Compound Semiconductors Grown by Molecular Beam Epitaxy**. University of Minnesota; 2005.

92. Koh YK, Cahill DG: **Frequency dependence of the thermal conductivity of semiconductor alloys**. *Phys Rev B* 2007, **76**:075207.

93. Buehl TE, Palmstrøm CJ, Gossard AC: **Embedded ErAs nanorods on GaAs (n11) substrates by molecular beam epitaxy**. *J Vac Sci Technol B Microelectron Nanom Struct* 2011, **29**:03C108.

94. Burke PG, Lu H, Kawasaki JK, Koh Y, Shakouri A, Palmstrøm CJ, Bowers JE, Gossard AC: **Influence of CeAs particles and Ce atoms on electronic properties of MBE grown InGaAs**. In *29th North Am Mol Beam Ep Conf*; 2012.

95. Krivoy EM, Rahimi S, Nair HP, Salas R, Maddox SJ, Ironside DJ, Jiang Y, Dasika VD, Ferrer DA, Kelp G, Shvets G, Akinwande D, Bank SR: **Growth and characterization of single crystal rocksalt LaAs using LuAs barrier layers**. *Appl Phys Lett* 2012, **101**:221908.

96. Ramu AT, Cassels LE, Hackman NH, Lu H, Zide JMO, Bowers JE: **Rigorous calculation of the Seebeck coefficient and mobility of thermoelectric materials**. *J Appl Phys* 2010, **107**:083707.

97. Zhao L-D, Lo S-H, Zhang Y, Sun H, Tan G, Uher C, Wolverton C, Dravid VP, Kanatzidis MG: **Ultralow thermal conductivity and high thermoelectric figure of merit in SnSe crystals.** *Nature* 2014, **508**:373–7.

98. Kim W, Singer SL, Majumdar A, Zide JMO, Klenov D, Gossard AC, Stemmer S: **Reducing thermal conductivity of crystalline solids at high temperature using embedded nanostructures**. *Nano Lett* 2008, **8**:2097–2099.

99. Lee S, Esfarjani K, Luo T, Zhou J, Tian Z, Chen G: **Resonant bonding leads to low lattice thermal conductivity**. *Nat Commun* 2014, **5**:1–8.

100. Poudel B, Hao Q, Ma Y, Lan Y, Minnich A, Yu B, Yan X, Wang D, Muto A, Vashaee D, Chen X, Liu J, Dresselhaus MS, Chen G, Ren Z: **High-thermoelectric performance of nanostructured bismuth antimony telluride bulk alloys**. *Science (80-)* 2008, **320**:634–8.

101. Boukai AI, Bunimovich Y, Tahir-Kheli J, Yu J-K, Goddard WA, Heath JR: **Silicon nanowires as efficient thermoelectric materials**. *Nature* 2008, **451**:168–71.

102. Abrahams MS, Braunstein R, Rosi FD: **Thermal, Electrical and Optical Properties of (In,Ga)As Alloys**. *J Phys Chem Solids* 1959, **10**:204–210.

103. May AF, Fleurial J-P, Snyder GJ: **Thermoelectric performance of lanthanum telluride produced via mechanical alloying**. *Phys Rev B* 2008, **78**:125205.

104. Zevalkink A, Toberer ES, Zeier WG, Flage-Larsen E, Snyder GJ: **Ca_3AlSb_3: an inexpensive, non-toxic thermoelectric material for waste heat recovery**. *Energy Environ Sci* 2011, **4**:510–518.

105. Price PJ: **Theory of Transport Effects in Semiconductors: Thermoelectricity**. *Phys Rev Lett* 1956, **104**:1223–1239.

106. Bahk J, Shakouri A: **Enhancing the thermoelectric figure of merit through the reduction of bipolar thermal conductivity with heterostructure barriers**. *Appl Phys Express* 2014, **105**:052106.

107. Bahk J-H, Zeng G, Zide JMO, Lu H, Singh R, Liang D, Ramu AT, Burke P, Bian Z, Gossard AC, Shakouri A, Bowers JE: **High-Temperature Thermoelectric Characterization of III–V Semiconductor Thin Films by Oxide Bonding**. *J Electron Mater* 2010, **39**:1125–1132.

108. Lin C-T, McMahon WE, Ward JS, Geisz JF, Wanlass MW, Carapella JJ, Olavarria W, Young M, Steiner MA, Frances RM, Kibbler AE, Duda A, Olson JM, Perl EE, Friedman DJ, Bowers JE: **Fabrication of Two-Terminal Metal-Interconnected Multijunction III-V Solar Cells**. In *PVSC IEEE Proc*. Austin, TX; 2011:944–948.

109. Lang D V.: **Deep-level transient spectroscopy: A new method to characterize traps in semiconductors**. *J Appl Phys* 1974, **45**:3023–3032.

110. Sethi S, Bhattacharya PK: **Characteristics and Device Applications of Erbium Doped III-V Semiconductors Grown by Molecular Beam Epitaxy**. *J Electron Mater* 1996, **25**:467–477.